Hokkaido University

Graduate School of Chemical Sciences and Engineering

Doctoral dissertation

Study on Atomic Layer Deposition (ALD) of Dielectric Films Using Novel Liquid Homoleptic Precursors for Advanced CMOS Devices

(次世代の CMOS デバイス向けの新規な液体ホモレプティック前駆体を用いた原子層堆積法による高誘電膜に関する研究)

Akihiro Nishida （西田 章浩）

Graduate School of Chemical Sciences and Engineering,

Hokkaido University

February 2024

Table of Contents

Chapter 1

General Introduction

"Society 5.0" is the vision for the next stage in the evolution of human society (Fig. 1), following its previous stages as a hunter-gatherer society (Society 1.0), agrarian society (Society 2.0), industrial society (Society 3.0), and information society (Society 4.0). [1] Society 5.0 is focused on achieving both economic development and solving social issues by utilizing a system of highly integrated virtual space with real space toward achieving sustainable development goals (SDGs), which are the common goals of the international community. [2] To achieve Society 5.0, semiconductor technology will become even more critical as a fundamental technology.

Figure 1. Schematic of Society 5.0. [1]

Semiconductors are an important technology that supports various components of a digital society, such as the Internet of Things (IoT), artificial intelligence (AI), Beyond 5G/6G, supercomputers, big data, robotics technology, and autonomous driving technology. Thus, research toward a device that can process a huge amount of data with high speed and low power consumption is being actively conducted. Recently, because of the influence of the world situation, semiconductors have become an extremely important strategic technology of national security [3]. Accordingly, from the perspective of economic security, governments of various countries have provided industrial support to accelerate the development of semiconductors. Capital investment by device manufacturers has also been increasing. As a result, miniaturization of semiconductor devices is now required for further improvement of device performance, energy savings, and cost reduction. That is,

semiconductor manufacturing technology is an indispensable fundamental technology for the further evolution of semiconductor devices.

History of transistors

An understanding of transistors is indispensable for understanding semiconductor technology. A transistor can amplify or switch electrical signals and power in an electronic circuit. The first point-contact transistor has developed by John Bardeen and Walter Houser Brattain at AT&T Bell Laboratories in 1947. William Bradford Shockley developed the bipolar transistor in 1948. Bardeen, Brattain, and Shockley were awarded the Nobel Prize in Physics for their research on semiconductors and the discovery of the transistor effect. Integrated circuits (ICs) were subsequently invented, enabling large numbers of transistors, capacitors, and resistors to be combined on the same substrate. Moreover, the integration density was dramatically increased; large-scale integrated circuits (LSIs) including 1,000–100,000 components or more on a chip were developed alongside advances in manufacturing technology. ICs and LSIs have become important components in electrical appliances. In 1965, Gordon Moore predicted that the number of transistors in a dense IC would double approximately every 2 years on the basis of his analysis of historical trends in the computer manufacturing industry (Fig. 2) [4]. This proposition is known as Moore's law and is widely accepted in the semiconductor and computer industries.

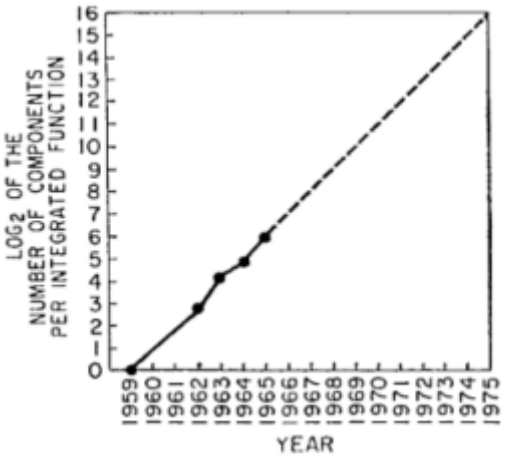

Figure 2. Original graph from "Cramming more components onto integrated circuits." [4]

In 1974, Robert H. Dennard advocated guiding principles to take advantage of these improvements in terms of metal oxide semiconductor field-effect transistor (MOSFET) device design, circuit design, and chip design [5]. These principles have served as the basic reference for the

semiconductor industry over several decades. In the 1980s, very-large-scale integration (VLSI) of 100,000–10,000,000 components on a chip was developed. In the 1990s, ultra-large-scale integration (ULSI) of more than 10,000,000 components on a chip appeared. These developments led to a dramatic increase in computing power. In the 2000s, systems-on-chips (SoCs) integrating various components such as a central processing unit (CPU), graphics, memory, storage, interfaces, and sensors were fabricated. SoCs enabled the manufacture of substantially smaller computers that consumed less power. Because of the development of SoCs, mobile computing devices were widely adopted worldwide. In 2022, the number of transistors reached 20 billion in the second-generation 5 nm technology for the Apple M2 chip. Researchers have continually innovated to realize numerous technical advances. The number of transistors is expected to further increase with future technological innovations (Fig. 3).

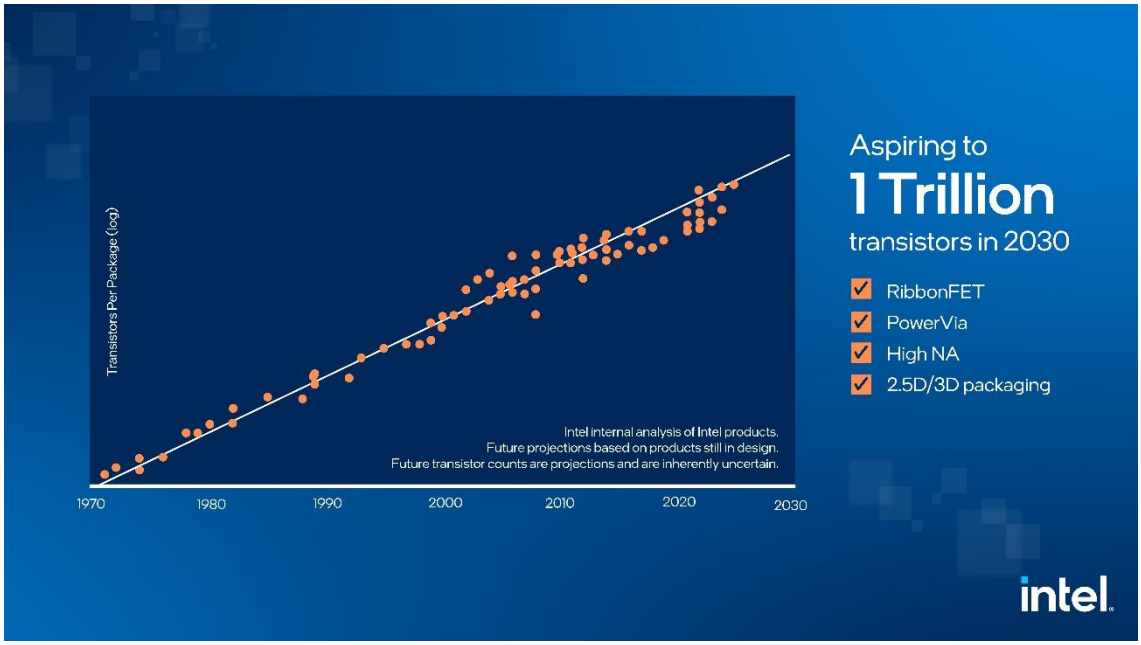

Figure 3. The number of transistors per device according to Moore's law: past, present, future. [6]

CMOS technology and high-*K* materials

The complementary metal oxide semiconductor (CMOS) field-effect transistor is the most important electronic device. CMOSs use complementary and symmetrical pairs of a *p*-channel MOS (PMOS) and an *n*-channel MOS (NMOS). Device scaling is achieved through reductions of the gate length, gate dielectric, source–drain junction depth, and other components of a MOSFET and through reduction the device area by shortening the switching time to increase performance and lower manufacturing costs. The scaling of CMOS transistors has led to the silicon dioxide (SiO_2) layer used as a gate dielectric becoming so thin that its leakage current is increased. However, as the SiO_2 film

used as the gate insulator gets thinner, the gate leakage current due to direct electron tunneling through the SiO_2 film becomes very high, exceeding 1 A/cm^2 at 1 V, making device operation difficult (Fig. 4). Therefore, it is necessary to search for materials that can replace SiO_2.

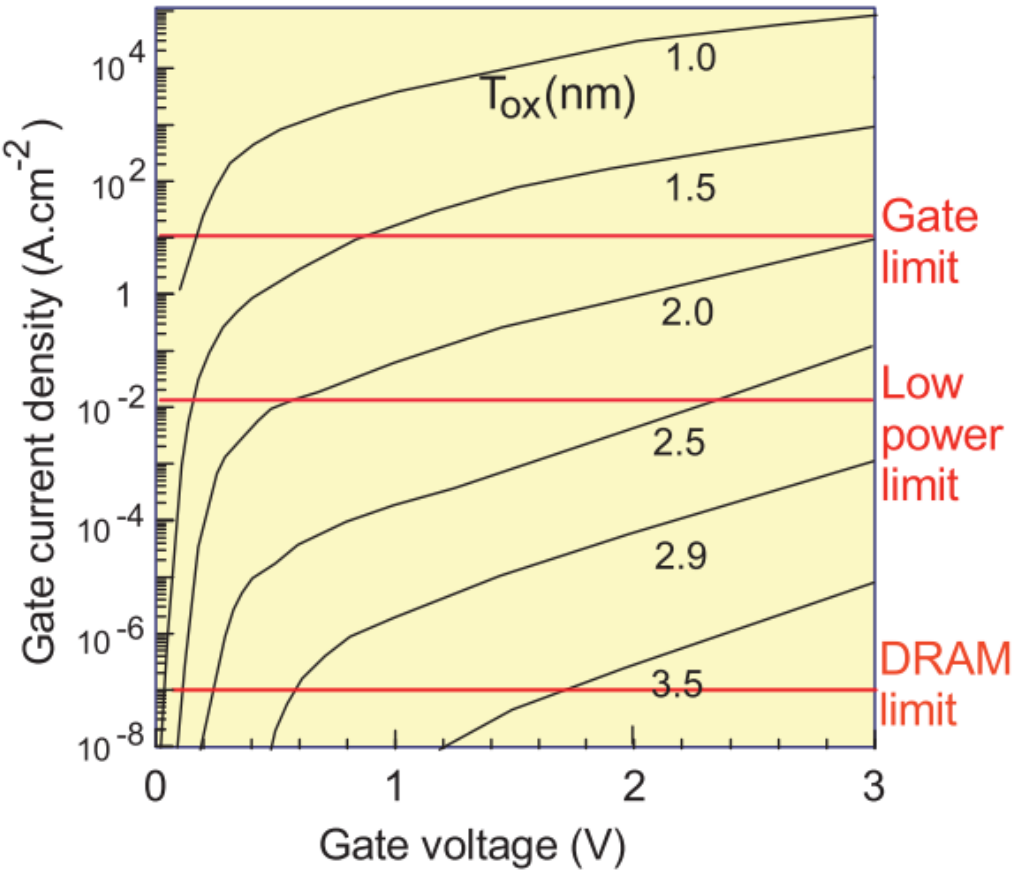

Figure 4. Leakage current vs voltage for SiO_2 layers of various thickness. [7]

FETs are capacitance-operated devices, and the source–drain current of a FET depends on its gate capacitance. The gate capacitance *C* is expressed as follows when considering a parallel plate capacitor that neglects quantum mechanical and depletion effects from the Si substrate and gate:

$$C = \frac{\varepsilon_0 K A}{t} \tag{1}$$

where ε_0 is the free-space electric permittivity ($= 8.85 \times 10^{-12}$ F/m), *K* is the relative permittivity, *A* is the area, and *t* is the thickness of the oxide. The tunneling current decreases exponentially with increasing distance. Thus, the solution to the tunneling problem is to replace SiO_2 with a physically

thicker layer of a new material with a higher *K*. This approach maintains the same capacitance but reduces the tunneling currents. These new gate oxides are called "high-*K* oxides" [8]. The relationship between the electric permittivity and bandgap of typical high-*K* oxides is shown in Fig. 5.

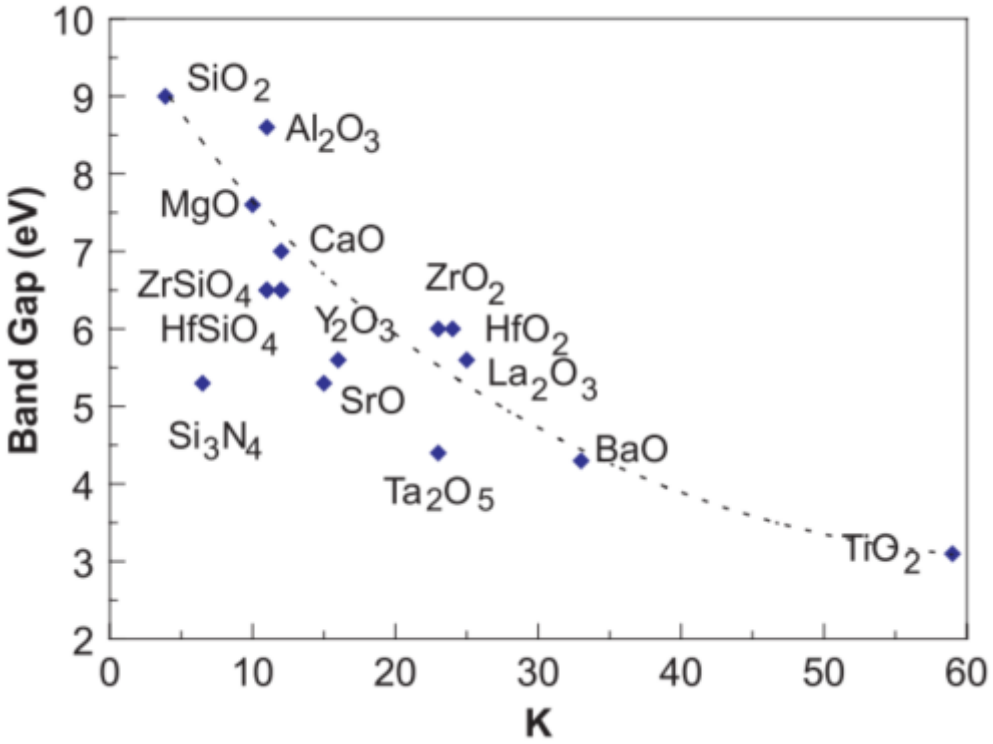

Figure 5. Static dielectric constant vs bandgap for candidate gate oxides. [9]

Although the magnitude of the relative permittivity is important in terms of capacitance, the magnitude of the bandgap is also important in terms of suppressing gate leakage current in FETs. Unfortunately, high-*K* materials have a smaller bandgap than SiO_2, resulting in a lower barrier height of tunneling. Therefore, ZrO_2, HfO_2, La_2O_3, Y_2O_3, and similar materials have been actively studied as stable compounds on Si substrates with both high electric permittivity and a large bandgap [10]. In 2007, Intel announced HK+MG technology that uses HfO_2 deposited by atomic layer deposition (ALD), and this high-dielectric material was adopted for CMOS devices (Fig. 6) [11].

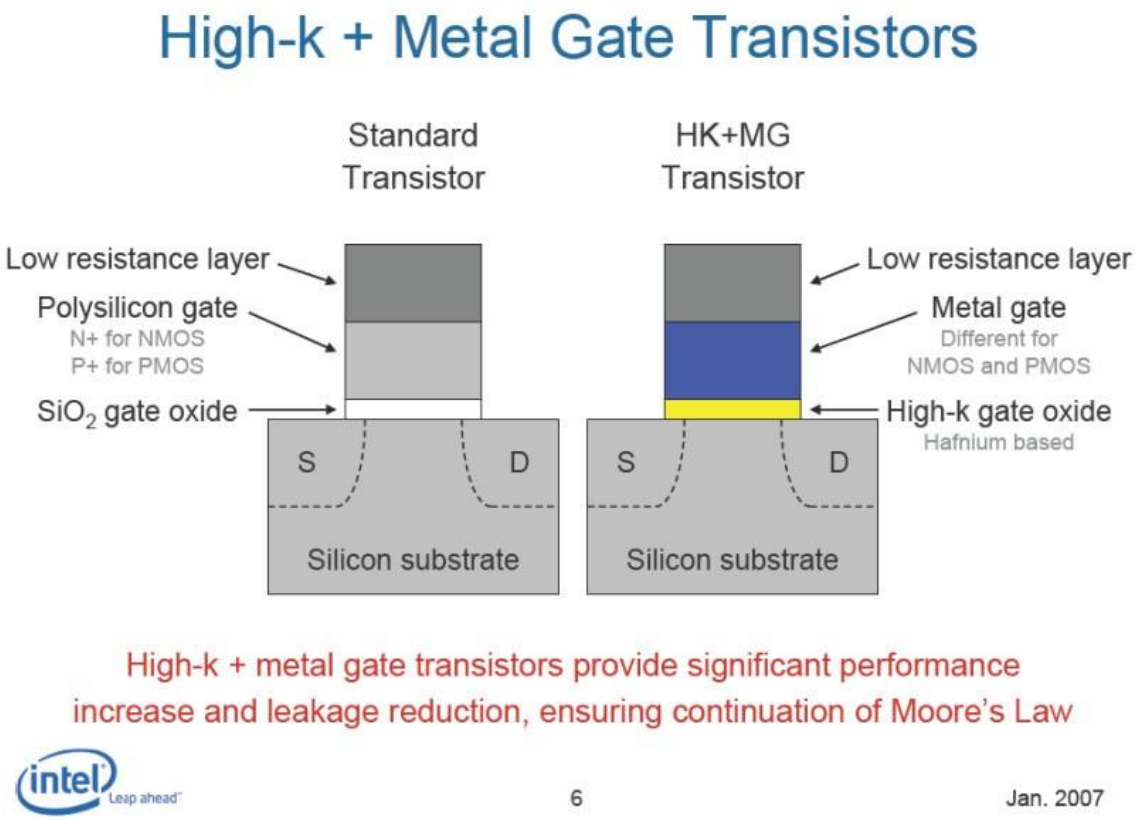

Figure 6. Structure of a standard transistor and a high-*k* + metal gate transistor. [11]

In the case of 32–45 nm technology nodes, only the planar structure shown above was practically used for MOSFETs in CMOS LSIs. However, for the 2*X* nm and smaller technology nodes, fin field effect transistor (FinFET) structures (Fig. 7) are the mainstream structures in LSIs that use bulk Si substrates [12]. In addition, gate-all-around (GAA) FETs, which are even more resistant to short channel effects than FinFETs, are emerging at technology nodes of 7 nm and smaller. In the future, 1 nm technology nodes are expected to move to the complementary FET structure, representing a further advancement. Therefore, deposition technologies that can correctly form high-*K* gate dielectrics in three-dimensional and denser structures are needed.

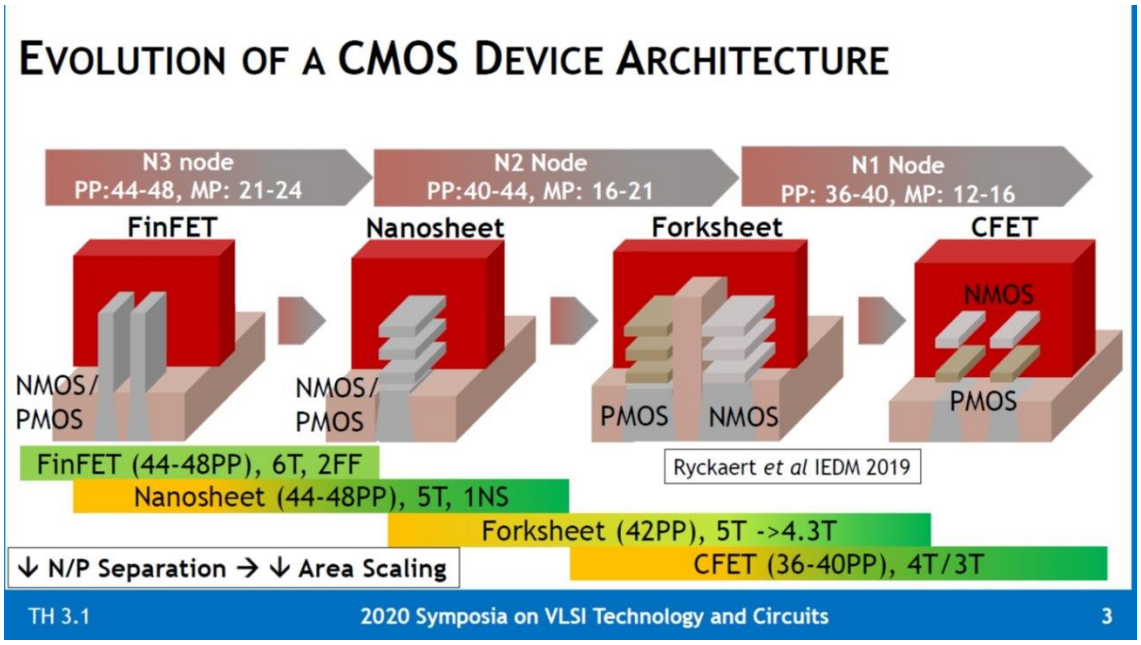

Figure 7. Evolution of the CMOS device architecture. [12] Where the PP is poly pitch (nm), MP is densest metal pitch (nm), T is track cell.

Memory technology and high-*K* materials

Memory is a device for storing information in a computer. Memory is categorized into volatile memory and nonvolatile memory depending on the operating principle of the semiconductor device. [13] Volatile memory can maintain stored data only while power is distributed, whereas nonvolatile memory retains data even when the power is turned off. The former includes dynamic random access memory (DRAM) and static random access memory (SRAM). The latter includes read only memory (ROM) such as mask ROM, programmable ROM (PROM), erasable programmable ROM (EPROM), and electrically erasable programmable ROM (EEPROM). Flash memory, magnetoresistive random access memory (MRAM), and ferroelectric random access memory (FeRAM) are also classified as nonvolatile memory. High-*K* dielectrics have become increasingly important because of the scaling of memory devices. Below, we share examples of high-*K* materials for memory devices.

DRAM

Substantial effort has been devoted over the past two decades to incorporating high-*K* dielectrics into DRAM storage capacitors. A DRAM memory cell consists of a single MOSFET and a cell capacitor, as shown in Figs. 8 and 9. [14]

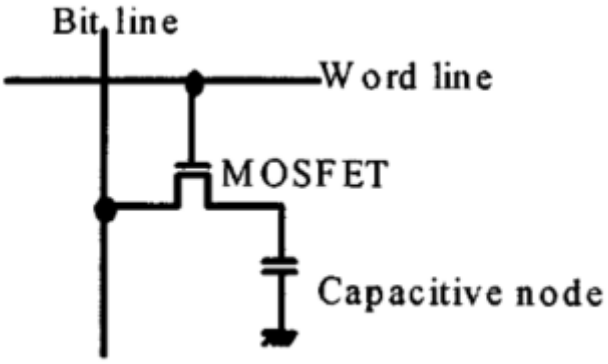

Figure 8. General DRAM cell structure. [14]

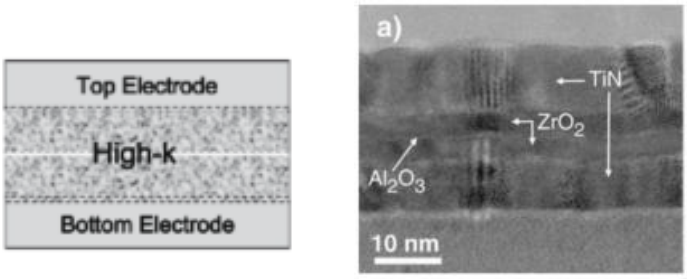

Figure 9. Schematic and high-resolution TEM image of a DRAM MIM capacitor. [15]

The amount of charge (Q_s) stored in a DRAM cell capacitor is expressed by the equation.

$$Q_s = C_s V \propto \frac{\varepsilon S}{t_{ox}} V \tag{2}$$

where ε is the relative permittivity of the capacitor dielectric film, S is the total area where a capacitor can be formed, t_{ox} is the thickness of the capacitor dielectric film, and V is the voltage applied to the capacitor. As clear from equation (2), Q_s can be increased four ways: 1) increasing the voltage (V) applied to the capacitor; 2) increasing the capacitor area (S); 3) reducing the thickness of the capacitor insulating film (t_{ox}); and 4) increasing the relative dielectric constant (ε) of the capacitor dielectric film.

As DRAMs increase in capacity, the voltage V applied to capacitors becomes difficult to increase because lower voltages are being used to reduce power consumption. Therefore, the capacitor structure was first changed from planar to three-dimensional to increase the capacitor area S. However, as memory cell miniaturization progresses, ensuring an adequate C_s by simply making the capacitor

structure three-dimensional becomes difficult. In addition, when a thermally oxidized silicon film (i.e., a SiO_2 film) is used as the capacitor insulator film, how thin the film can be made encounters a lower limit because an excessively thin film increases the leakage current due to direct tunneling. Accordingly, research was conducted on the use of high-*K* films as capacitor dielectric films. SiO_2/SiN/SiO_2 (ONO), Ta_2O_5, and Al_2O_3 have been used as capacitor insulating films [16]. A combination of a HfO_2 film and Al_2O_3 film with a large bandgap, which had been developed for gate insulating films, was also introduced as a capacitor dielectric film to improve the dielectric constant. Recently, ZrO_2–Al_2O_3–ZrO_2 (ZAZ) capacitor structures consisting of ZrO_2, which has a higher dielectric constant than HfO_2, and an ultra-thin (~0.5 nm) layer of Al_2O_3 have been used [15]. These capacitor dielectric films must be deposited uniformly in a three-dimensional cylinder or pillar structure to increase the capacitor area *S* (Fig. 10). To achieve the required structure, these capacitor dielectric films are deposited by the ALD method.

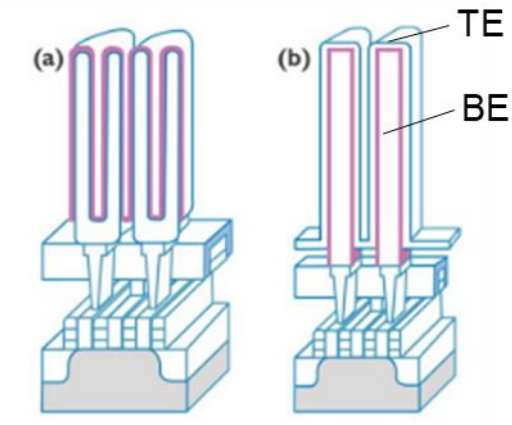

Figure 10. Schematics of double-sided cup-type (a) and pillar-type (b) DRAM capacitor designs. [17] Where the pink layer is high-*K* dielectric film. The TE is top electrode. The BE is bottom electrode.

FeRAM

FeRAM is a nonvolatile RAM that has unique characteristics such as data retention when power is turned off, like ROM and Flash memory, and a fast read–write access, similar to DRAM. The memory cell of FeRAM is composed of a capacitor and a transistor (Fig. 11). [18] The 1 transistor and 1 capacitor (1T-1C) FeRAM cell architecture is especially similar to the DRAM cell structure. Unlike DRAM, FeRAM employs the polarization characteristic of ferroelectrics as a memory element of the capacitor dielectric. Ferroelectrics are characterized by spontaneous polarization, the direction of which can be changed by an external electric field. The polarization shows a hysteresis loop in the dependence of polarization *P* on electric field *E* (Fig. 12). [19] FeRAM can store data in the cell using this characteristic. In a DRAM cell, the data periodically require refreshing because of discharging of the capacitor, whereas FeRAM maintains the data without any external power supply. Hence, FeRAM

is expected to lower the power consumption of computer devices.

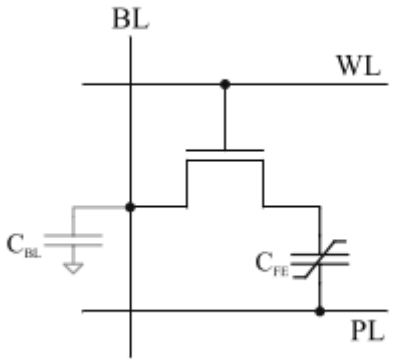

Figure 11. Schematic layout of a FeRAM 1T-1C cell. [18] Where the BL is bit-line. The WL is word-line. The PL is plate-line. The C is capacitor.

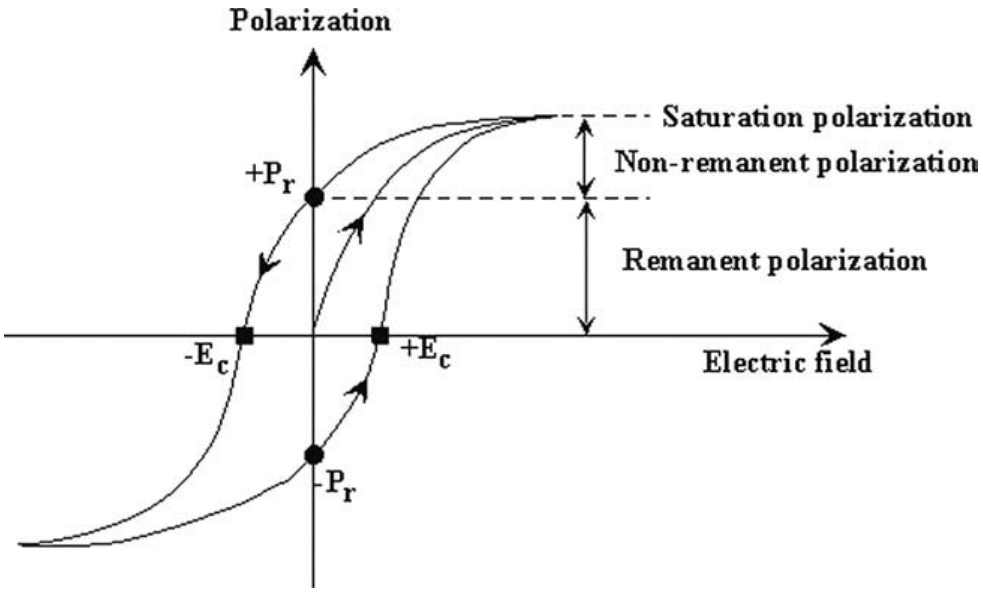

Figure 12. Typical polarization vs electric field (*P–E*) hysteresis loop of a ferroelectric. [19]

Perovskite-based materials such as $SrBi_2Ta_2O_9$ (SBT) and $Pb(Zr_xTi_{1-x})O_3$ (PZT) have been demonstrated as ferroelectric materials for FeRAM. [20, 21] However, FeRAM using perovskite-based materials has problems with low memory density and high manufacturing cost because of a low affinity with CMOS technology and the minimum thickness required for ferroelectricity. Since T. S. Boescke first reported ferroelectricity in Si-doped HfO_2 thin films in 2011, HfO_2-based materials have been attracting attention as ferroelectric materials for use in FeRAM [22]. HfO_2 has already been

established as a high-*K* dielectric material in the CMOS technology; thus, HfO_2-based materials deposited by ALD are one of the most important materials in FeRAM and have been extensively studied in recent years. [23-28]

Deposition technologies of high-*K* materials

The scaling of semiconductor devices has been achieved through advances in manufacturing technology, such as oxidation, deposition, photolithography, etching, resist stripping, cleaning, and many other processes. This thesis describes thin-film deposition technology. In general, high-*K* films are deposited by physical vapor deposition (PVD) and chemical vapor deposition (CVD). PVD and CVD show high film growth rates; thus, the film can be deposited with high productivity. However, the step coverage is insufficient in principle; thus, depositing a high-*K* film on a complex structure having a high aspect ratio is difficult. ALD based on self-limiting surface reactions is promising for depositing high-*K* films with good coverage and high purity and without pinholes. Typical deposition conditions and the film-forming characteristics of the PVD, CVD, and ALD methods are compared in Table 1. [29] The advantages of ALD over PVD and CVD are precise uniformity control and high conformality; thus, ALD is more suitable than PVD and CVD for advanced semiconductor manufacturing processes (Fig. 13). [30]

Table 1. Comparison of the deposition properties for PVD, CVD, and ALD. [29]

Deposition conditions	PVD	CVD	ALD
Vacuum requirement	$<10^{-2}$ Torr	10^{-3}–10^{2} Torr	10^{-4}–1 Torr
Deposition thickness range	5 nm–>10 μm	10 nm–>3 μm	0.1–40 nm
Uniformity control	nm	nm	0.1 nm
Deposition rate	10–1000 nm/min	10–1000 nm/min	<0.2 nm/cycle; <1.0 nm/min typical
Conformality	15% at 4:1 aspect ratio	0%–100% at 4:1 aspect ratio	100% at 15:1 aspect ratio
Contamination/ Particles	Indirect only (flaking)	Particles can exist due to gas phase reactions	Low: no gas phase chemistry

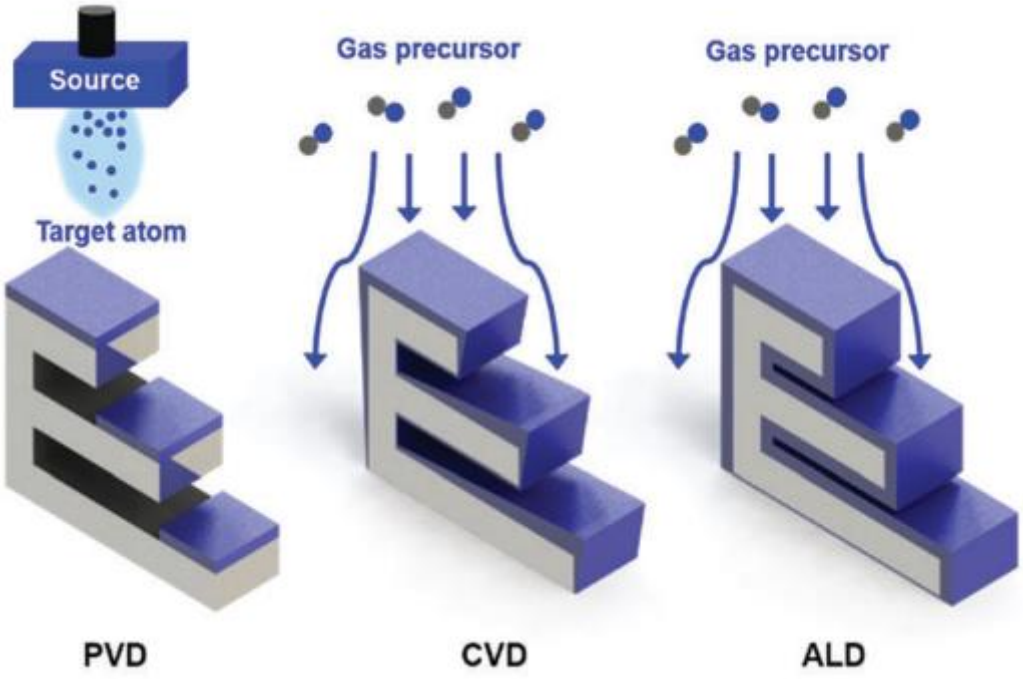

Figure 13. Schematic of film deposition techniques. [30]

Mechanism of ALD

ALD generally consists of four steps, as schematically illustrated in Figure 14. [31] In preparation for the ALD process, the substrate is placed into an ALD chamber under high vacuum and heated at 100–400 °C. An initial precursor vapor is introduced into the chamber after the substrate temperature has stabilized. The precursor molecules (Reactant A) adsorb onto and form a chemically bound monolayer on the substrate surface via chemisorption (Step 1). Excessive ALD precursor molecules also reach the surface and are bound only by physisorption. The physisorption is sufficiently weak to allow the remaining precursor to be pumped away under high vacuum. This self-limiting reaction is the reason for ALD saturation. The chamber is then purged with inert gas to remove any excess precursor (Step 2). Next, Reactant B is introduced into the process chamber to react with the adsorbed monolayer to generate the desired compound on the substrate surface (Step 3). Finally, the byproducts of this reaction are purged with inert gas and pumped away (Step 4). The four-step cycle is repeated until the desired thickness is achieved.

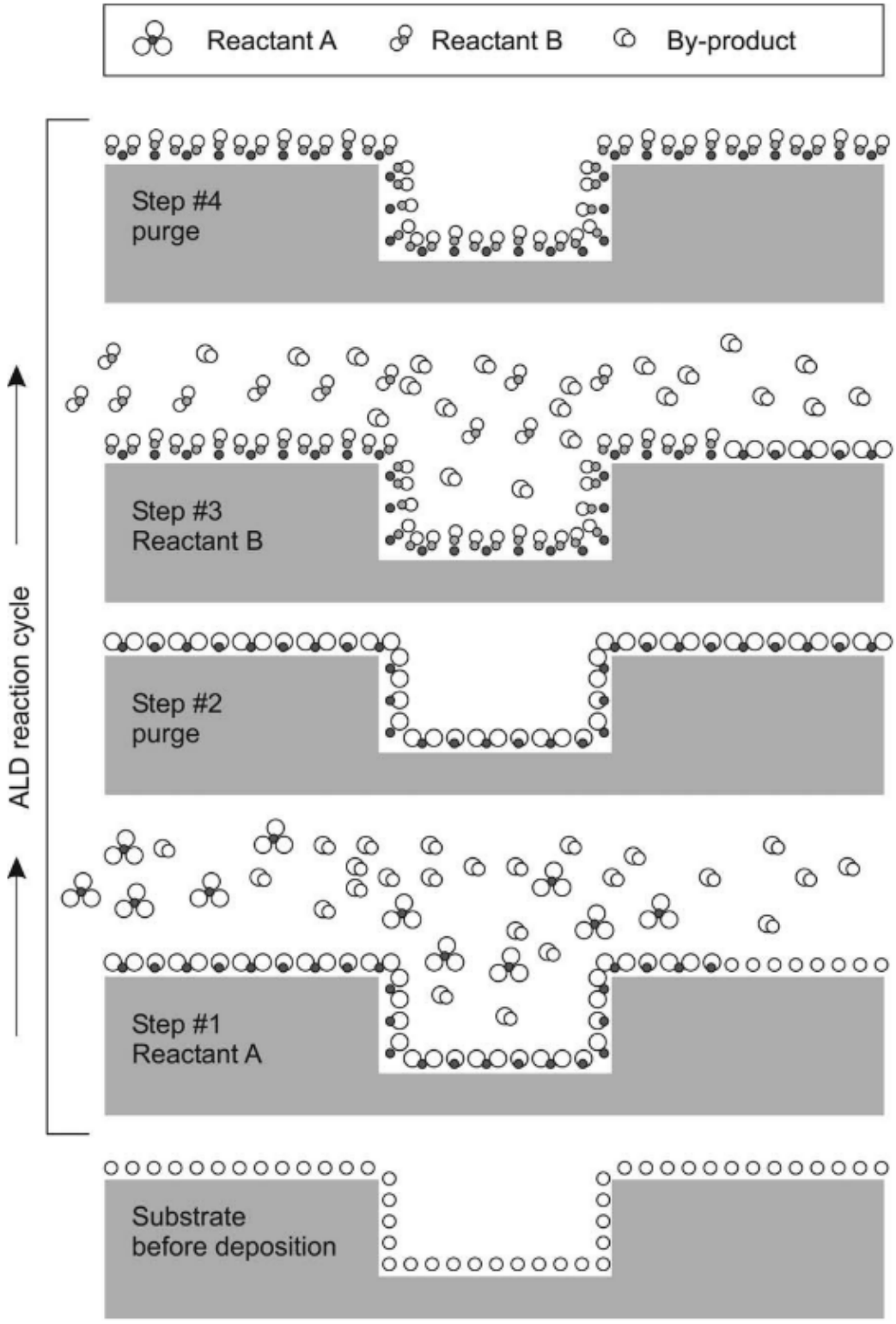

Figure 14. Schematic of one ALD reaction cycle. [31]

For ALD processing, the optimal temperature range for each ALD precursor needs to be determined. The optimum temperature range for ideal ALD behavior, which is known as the "ALD window," is known to exist between nonideal regions (Fig. 15). At lower temperatures, the growth per cycle (GPC) increases when the ALD precursors can condense on the surface. Alternatively, the GPC decreases if the surface reactions lack sufficient thermal energy to proceed to completion. At higher temperatures, the GPC increases when the surface species can decompose and allow the adsorption of additional reactants. This behavior is similar to CVD by unimolecular decomposition. If the surface species desorb from the substrate surface because of thermal energy, the GPC will decrease at higher temperatures. Therefore, the selection of a suitable ALD precursor having a desirable ALD window is critical to attaining the target film. However, because of complications in the manufacturing process due to device scaling, conventional ALD precursors are no longer suitable for future semiconductor device manufacturing. The development of new ALD precursors is urgently needed.

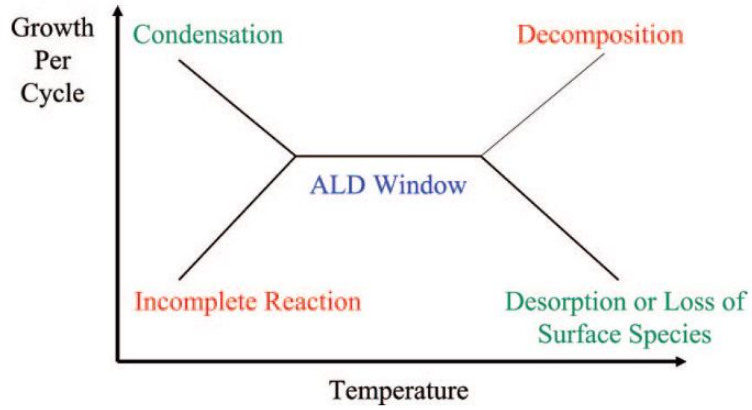

Figure 15. Schematic of possible behavior for the ALD growth per cycle versus temperature, showing the "ALD window." [32]

Global market of ALD precursors

ALD was originally called atomic layer epitaxy (ALE) and was developed by Tuomo Suntola and Jorma Antson in the 1970s for fabricating polycrystalline luminescent ZnS:Mn and amorphous Al_2O_3 insulator films for electroluminescent flat-panel displays. [31] Since the 2000s, interest in ALD for scaling down microelectronic devices has greatly increased, as reflected by the number of scientific publications related to ALD (Fig. 16). Accordingly, a huge number of ALD processes and precursors have been developed. Today, the world market for ALD precursors is worth approximately US$640M. The forecast compound annual growth rate (CAGR) of the ALD precursor market is expected to be approximately 10% from 2020 to 2024 [33]. Therefore, ALD precursors should not only enable the deposition of target films but should also have industrially preferred properties in anticipation of their use in mass production processes.

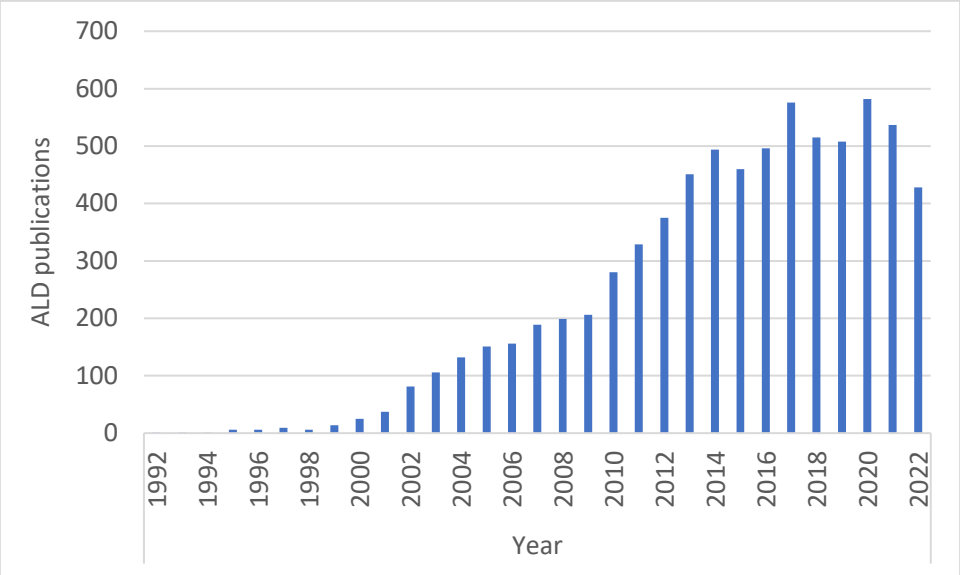

Figure 16. Number of publications related to ALD per year between 1992 and 2022. The search was performed with Web of Science. The search phrase was "atomic layer deposition" in the title.

ALD precursors

ALD precursors are volatile metal complexes having self-limiting adsorption and reaction steps. Numerous types of compounds are widely used as ALD precursors. Figure 17 summarizes the most common ALD precursors used for high-*K* films. Metal halides, especially chlorides, have been used to deposit Al_2O_3, TiO_2, ZrO_2, HfO_2, and other films. [34-37] These precursors have a wide ALD window because of their high thermal stability. However, most metal halide complexes are solids and cause halide contamination in the resultant film. In general, halide contaminants in films reduce the reliability of semiconductor devices. Metal alkyls such as trimethylaluminum ($AlMe_3$) exhibit high volatility and are small molecules; they therefore exhibit almost ideal ALD behavior. [38] However, safety is an important concern, especially for mass-production, because metal alkyls tend to be pyrophoric. Metal alkylamide precursors are commonly used as ALD precursors for TiO_2, ZrO_2, and HfO_2, among other metal oxides. [39, 40] These precursors exhibit high volatility as well as low melting points. However, the ALD window of metal alkylamide precursors is limited to the region below 300 °C because they have relatively weak metal (*M*)–N bonds. Alkoxide precursors require a relatively high temperature for the ALD reaction because of the relatively stable *M*–O bonding. [41] Alkoxide precursors also have a narrow ALD window because of their low reactivity at low temperatures and tendency to thermally decompose at high temperature. [42] β-Diketonates are common precursors for CVD but are not suitable for ALD. β-Diketonates require a strong oxidant such as O_3 for the reaction because they have two stable *M*–O bonds to the ligand. [43] In addition, β-diketonates are generally solid precursors at room temperature and exhibit low volatility. Amidinate precursors consist of amides

chelated to a metal center through two *M*–N bonds. Like alkylamide precursors, they exhibit high reactivity. The structure of amidinates makes them good ALD precursor candidates, especially for the deposition of La_2O_3 and Y_2O_3 films. [44-46] However, the GPC with amidinates is lower than that with alkylamide precursors because of amidinates' bulky structure. Metal cyclopentadienyls are candidates for advanced ALD precursor structures because cyclopentadienyl (Cp) ligands are good electron donors and metal cyclopentadienyls bound to good metal electron acceptors are relatively stable. [43, 47, 48] However, cyclopentadiene used as a ligand is a highly flammable compound and must be cooled to restrain its dimerization, which is an exothermic reaction. [49] Cyclopentadiene is prepared by cracking dicyclopentadiene and should be used without delay for safety. This point is a major concern for using cyclopentadiene in mass production.

Heteroleptic precursors that combine the aforementioned ligands, such as cyclopentadienyltris(dimethylamino)zirconium(IV) ($CpZr(NMe_2)_3$) have been developed as precursors with improved properties. [50-52] Heteroleptic precursors having the characteristics of both ligand types (i.e., cyclopentadienyl and dimethylamino ligands) are expected to be used in advanced semiconductor manufacturing processes. However, the synthetic route and isolation process of the target heteroleptic precursors make their production difficult. In addition, the disproportionation reaction must be suppressed. As a result, the cost of heteroleptic precursors is generally higher than that of homoleptic precursors. Therefore, we consider that heteroleptic precursors are not always the best precursors for industrial use.

As described above, numerous studies on ALD precursors have been reported. However, there has been little research on optimizing the molecular structure of ALD precursors for easy precursor manufacturing and long-term stability in the film production process. Therefore, many of the precursors used for mass production processes still suffer various problems. The constraints of manufacturing processes that use ALD precursors should be eliminated for future CMOS device production.

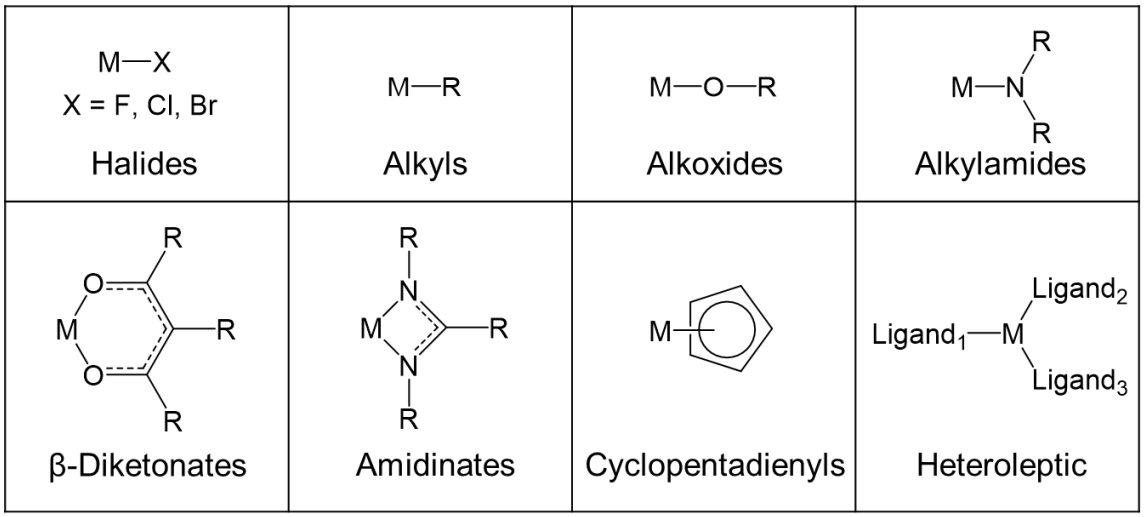

Figure 17. Summary of the most common ALD precursors for high-*K* films. M and R in the chemical structures represent a metal and an alkyl group, respectively.

Purpose of this study

The purpose of this study is to evaluate the ALD processes, film characteristics, and electric properties of deposited films prepared via novel liquid ALD precursors for industrial use. In particular, this paper deals with novel liquid ALD precursors that have a homoleptic structure for the ALD of high-*K* films such as Y_2O_3, HfO_2, ZrO_2, and $Hf_xZr_{1-x}O_2$ (HZO). We propose that the following characteristics are especially necessary for an industrially preferred precursor.

1. Liquid at room temperature

The melting point of precursors should be lowered to overcome several problems, such as a difficult purification process of precursor manufacturing, clogging of precursor delivery lines, and the generation of particles on the wafer. A complicated precursor canister is necessary to maintain a constant temperature for stable vapor generation of a solid precursor. [53] If the precursor is a liquid at room temperature, then a liquid delivery system can be used to generate a large amount of vapor, thereby improving productivity for a batch process by enabling faster saturation.

2. Halide free

To prevent halide contamination of the deposited films, the ALD precursor should not contain halide atoms. In addition, halides generate corrosive byproducts as a result of the ALD reaction. [54, 55] Thus, etching of the deposited films, corrosion of the ALD equipment, and the additional cost of processing waste-gas using scrubbers are major problems.

3. High volatility and high decomposition temperature

In principle, the vapor of the ALD precursor should be generated by heating for the ALD process. The available temperature range of the ALD precursor should be expanded by reducing the temperature at which volatilization occurs and increasing the thermal decomposition temperature. [32]

4. Reactivity with a co-reactant

If the reactivity decreases, film contamination increases as a result of an incomplete reaction. In addition, a higher deposition temperature will be needed for the ALD reaction. As a result, the ALD window between the reaction temperature and the thermal decomposition temperature becomes narrower. Therefore, high reactivity is important for an ALD precursor. [32]

5. Homoleptic molecular structure

A heteroleptic structure can improve several precursor properties. However, the synthetic route and purification process for heteroleptic precursors are complicated. In addition, the disproportionation reaction must be suppressed. As a result, the cost of heteroleptic precursors is higher than that of homoleptic precursors.

6. Film growth rate per ALD cycle

A higher film growth rate is critical for achieving high film productivity for industrial applications. However, the requirement of precise film thickness control to within 1 Å increases for cutting-edge semiconductor manufacturing methods with high film growth rates. Increasing the number of ALD precursor options depending on the application is critical.

7. Long-term thermal stability at the source temperature over a few months

ALD precursors are heated for an extended time to generate the vapor. Long-term thermal stability at the source temperature for more than few months is critical for industrial use. When a long-life precursor is used, the film can be continuously produced without stopping the production line.

Organization of present paper

This thesis is composed of six chapters. In chapter 1, we discuss general information about the study.

In chapter 2, we present the ALD of Y_2O_3 films using a novel liquid homoleptic yttrium precursor: tris(*sec*-butylcyclopentadienyl)yttrium(III) [$Y(^sBuCp)_3$] (Fig. 18).

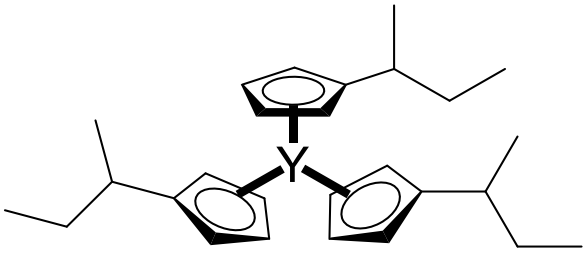

Figure 18. Chemical structure of ALD precursor Y(^{s}BuCp)$_3$.

In chapter 3, we present the ALD of HfO_2 films using the novel liquid homoleptic hafnium precursor tetrakis(1-(*N*,*N*-dimethylamino)-2-propoxy)hafnium [Hf(dmap)$_4$] (Fig. 19).

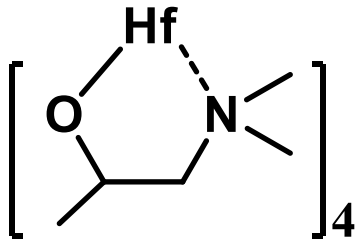

Figure 19. Chemical structure of ALD precursor Hf(dmap)$_4$.

In chapter 4, we present the ALD of a ZrO_2 film using the novel liquid homoleptic zirconium precursor tetrakis(1-(*N*,*N*-dimethylamino)-2-propoxy)zirconium [Zr(dmap)$_4$] (Fig. 20).

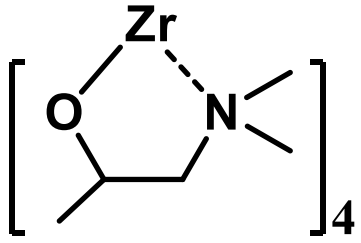

Figure 20. Chemical structure of ALD precursor Zr(dmap)$_4$.

In chapter 5, we present the ALD of a HZO film using a mixture of Hf(dmap)$_4$ and Zr(dmap)$_4$ named "FER-1" as an ALD precursor.

In chapter 6, we summarize our study.

References

(1) 経団連. *経団連 SDGs*. 2022. https://en.keidanrensdgs.com/society-5-0-jp (accessed.

(2) 文部科学省. 令和 3 年版科学技術・イノベーション白書. 文部科学省, Ed.; 2021.
(3) 経済産業省. 半導体・デジタル産業戦略検討会議. 経済産業省, Ed.; 2022.
(4) Moore, G. E. Cramming more components onto integrated circuits. *Electronics* **1965**, *38* (8), 114-117.
(5) Dennard, R. H.; Gaensslen, F. H.; Yu, H. N.; Rideout, V. L.; Bassous, E.; Leblanc, A. R. Design of ion-implanted MOSFET's with very small physical dimensions. *IEEE Journal of Solid-State Circuits* **1974**, *9*, 256-268.
(6) Kelleher, A. Moore's Law – Now and in the Future. Intel Newsroom: 2022.
(7) Robertson, J.; Wallace, R. M. High-K materials and metal gates for CMOS applications. *Materials Science and Engineering: R: Reports* **2015**, *88*, 1-41. DOI: 10.1016/j.mser.2014.11.001.
(8) Gusev, E. P.; Cartier, E.; Buchanan, D. A.; Gribelyuk, M.; Copel, M.; Okorn-Schmidt, H.; D'Emic, C. Ultrathin high-K metal oxides on silicon: processing, characterization and integration issues. *Microelectronic Engineering* **2001**, *59* (1-4), 341-349. DOI: 10.1016/s0167-9317(01)00667-0.
(9) Robertson, J. High dielectric constant oxides. *The European Physical Journal Applied Physics* **2004**, *28* (3), 265-291. DOI: 10.1051/epjap:2004206.
(10) Hubbard, K. J.; Schlom, D. G. Thermodynamic stability of binary oxides in contact with silicon. *Journal of Materials Research* **1996**, *11* (11), 2757-2776. DOI: 10.1557/jmr.1996.0350.
(11) Intel. A 45nm Logic Technology with High-k+Metal Gate Transistors, Strained Silicon, 9 Cu Interconnect Layers, 193nm Dry Patterning, and 100% Pb-free Packaging. In 2007.
(12) Subramanian, S. First Monolithic Integration of 3D Complementary FET (CFET) on 300mm Wafers. *imec* **2020**.
(13) Meena, J. S.; Sze, S. M.; Chand, U.; Tseng, T. Y. Overview of emerging nonvolatile memory technologies. *Nanoscale Res Lett* **2014**, *9* (1), 526. DOI: 10.1186/1556-276X-9-526 From NLM PubMed-not-MEDLINE.
(14) Makihara, A.; Shindou, H.; Nemoto, N.; Kuboyama, S.; Matsuda, S.; Oshima, T.; Hirao, T.; Itoh, H.; Buchner, S.; Campbell, A. B. Analysis of single-ion multiple-bit upset in high-density DRAMs. *IEEE Transactions on Nuclear Science* **2000**, *47* (6), 2400-2404. DOI: 10.1109/23.903783.
(15) Kittl, J. A.; Opsomer, K.; Popovici, M.; Menou, N.; Kaczer, B.; Wang, X. P.; Adelmann, C.; Pawlak, M. A.; Tomida, K.; Rothschild, A.; et al. High-k dielectrics for future generation memory devices (Invited Paper). *Microelectronic Engineering* **2009**, *86* (7-9), 1789-1795. DOI: 10.1016/j.mee.2009.03.045.
(16) Yeh, W. K.; Lin, Y. C.; Chen, T. P.; Huang, C. T.; Chang, S. J.; Lin, W. J.; Jung, L. T.; Chien, S. C.; Sun, S. W.; Liou, F. T. A low thermal budget high performance 0.25-0.18 mu m merged logic device and dynamic random access memory application. *Japanese Journal of Applied Physics*

Part 1-Regular Papers Short Notes & Review Papers **2000**, *39* (4B), 2162-2166. DOI: 10.1143/jjap.39.2162.

(17) Popovici, M. High-performance (EOT<0.4nm, Jg~10－7 A/cm2) ALD-deposited Ru¥SrTiO3 stack for next generations DRAM pillar capacitor. **2018**. DOI: 10.1109/IEDM.2018.8614673.

(18) Kohlstedt, H.; Mustafa, Y.; Gerber, A.; Petraru, A.; Fitsilis, M.; Meyer, R.; Bottger, U.; Waser, R. Current status and challenges of ferroelectric memory devices. *Microelectronic Engineering* **2005**, *80*, 296-304. DOI: 10.1016/j.mee.2005.04.084.

(19) Izyumskaya, N.; Alivov, Y. I.; Cho, S. J.; Morkoç, H.; Lee, H.; Kang, Y. S. Processing, Structure, Properties, and Applications of PZT Thin Films. *Critical Reviews in Solid State and Materials Sciences* **2007**, *32* (3-4), 111-202. DOI: 10.1080/10408430701707347.

(20) Pinnow, C.-U.; Mikolajick, T. Material Aspects in Emerging Nonvolatile Memories. *Journal of The Electrochemical Society* **2004**, *151* (6). DOI: 10.1149/1.1740785.

(21) Sakoda, T.; Moise, T. S.; Summerfelt, S. R.; Colombo, L.; Xing, G.; Gilbert, S. R.; Loke, A. L. S.; Ma, S.; Kavari, R.; Wills, L. A.; et al. Hydrogen-Robust Submicron IrOx/Pb(Zr, Ti)O3/Ir Capacitors for Embedded Ferroelectric Memory. *Japanese Journal of Applied Physics* **2001**, *40* (4S). DOI: 10.1143/jjap.40.2911.

(22) Boescke, T. S.; Muller, J.; Brauhaus, D.; Schroder, U.; Bottger, U. Ferroelectricity in hafnium oxide thin films. *Applied Physics Letters* **2011**, *99* (10). DOI: 10.1063/1.3634052.

(23) Muller, J.; Boscke, T. S.; Schroder, U.; Mueller, S.; Brauhaus, D.; Bottger, U.; Frey, L.; Mikolajick, T. Ferroelectricity in Simple Binary ZrO2 and HfO2. *Nano Lett* **2012**, *12* (8), 4318-4323. DOI: 10.1021/nl302049k From NLM PubMed-not-MEDLINE.

(24) Shekhawat, A.; Walters, G.; Yang, N.; Guo, J.; Nishida, T.; Moghaddam, S. Data retention and low voltage operation of Al(2)O(3)/Hf(0.5)Zr(0.5)O(2) based ferroelectric tunnel junctions. *Nanotechnology* **2020**, *31* (39), 39LT01. DOI: 10.1088/1361-6528/ab9cf7 From NLM PubMed-not-MEDLINE.

(25) Hur, J.; Tasneem, N.; Choe, G.; Wang, P.; Wang, Z.; Khan, A. I.; Yu, S. Direct comparison of ferroelectric properties in Hf(0.5)Zr(0.5)O(2) between thermal and plasma-enhanced atomic layer deposition. *Nanotechnology* **2020**, *31* (50), 505707. DOI: 10.1088/1361-6528/aba5b7 From NLM PubMed-not-MEDLINE.

(26) Materano, M.; Mittmann, T.; Lomenzo, P. D.; Zhou, C.; Jones, J. L.; Falkowski, M.; Kersch, A.; Mikolajick, T.; Schroeder, U. Influence of Oxygen Content on the Structure and Reliability of Ferroelectric HfxZr1–xO2 Layers. *ACS Applied Electronic Materials* **2020**, *2* (11), 3618-3626. DOI: 10.1021/acsaelm.0c00680.

(27) Mukundan, V.; Consiglio, S.; Triyoso, D. H.; Tapily, K.; McBriarty, M. E.; Schujman, S.; Beckmann, K.; Hazra, J.; Kaushik, V.; Cady, N.; et al. Ferroelectric Phase Content in 7 nm Hf(1

−x)ZrxO2 Thin Films Determined by X - Ray - Based Methods. *physica status solidi (a)* **2021**, *218* (10). DOI: 10.1002/pssa.202100024.
(28) Shekhawat, A.; Hsain, H. A.; Lee, Y.; Jones, J. L.; Moghaddam, S. Effect of ferroelectric and interface films on the tunneling electroresistance of the Al(2)O(3)/Hf(0.5)Zr(0.5)O(2)based ferroelectric tunnel junctions. *Nanotechnology* **2021**, *32* (48). DOI: 10.1088/1361-6528/ac1ebe From NLM PubMed-not-MEDLINE.
(29) Crowell, J. E. Chemical methods of thin film deposition: Chemical vapor deposition, atomic layer deposition, and related technologies. *Journal of Vacuum Science & Technology A* **2003**, *21* (5), S88-S95. DOI: 10.1116/1.1600451.
(30) Shim, J. H.; Choi, H. J.; Kim, Y.; Torgersen, J.; An, J.; Lee, M. H.; Prinz, F. B. Process–property relationship in high-k ALD SrTiO3 and BaTiO3: a review. *Journal of Materials Chemistry C* **2017**, *5* (32), 8000-8013. DOI: 10.1039/c6tc05158h.
(31) Puurunen, R. L. Surface chemistry of atomic layer deposition: A case study for the trimethylaluminum/water process. *Journal of Applied Physics* **2005**, *97* (12). DOI: 10.1063/1.1940727.
(32) George, S. M. Atomic Layer Deposition: An Overview. *Chemical Reviews* **2010**, *110* (1), 111-131. DOI: 10.1021/cr900056b.
(33) TECHCET. Critical Materials Report and Market Briefings. **2021**.
(34) Raisanen, P. I.; Ritala, M.; Leskela, M. Atomic layer deposition of Al2O3 films using AlCl3 and Al((OPr)-Pr-i)(3) as precursors. *Journal of Materials Chemistry* **2002**, *12* (5), 1415-1418. DOI: 10.1039/b201385c.
(35) Aarik, J.; Aidla, A.; Mandar, H.; Uustare, T. Atomic layer deposition of titanium dioxide from TiCl4 and H2O: investigation of growth mechanism. *Applied Surface Science* **2001**, *172* (1-2), 148-158. DOI: 10.1016/s0169-4332(00)00842-4.
(36) Kukli, K.; Ritala, M.; Aarik, J.; Uustare, T.; Leskela, M. Influence of growth temperature on properties of zirconium dioxide films grown by atomic layer deposition. *Journal of Applied Physics* **2002**, *92* (4), 1833-1840. DOI: 10.1063/1.1493657.
(37) Park, H. B.; Cho, M.; Park, J.; Lee, S. W.; Hwang, C. S.; Kim, J.-P.; Lee, J.-H.; Lee, N.-I.; Kang, H.-K.; Lee, J.-C.; et al. Comparison of HfO2 films grown by atomic layer deposition using HfCl4 and H2O or O3 as the oxidant. *Journal of Applied Physics* **2003**, *94* (5), 3641-3647. DOI: 10.1063/1.1599980.
(38) Groner, M. D.; Fabreguette, F. H.; Elam, J. W.; George, S. M. Low-temperature Al2O3 atomic layer deposition. *Chemistry of Materials* **2004**, *16* (4), 639-645. DOI: 10.1021/cm0304546.
(39) Hausmann, D. M.; Kim, E.; Becker, J.; Gordon, R. G. Atomic layer deposition of hafnium and zirconium oxides using metal amide precursors. *Chemistry of Materials* **2002**, *14* (10), 4350-4358. DOI: 10.1021/cm020357x.

(40) Abendroth, B.; Moebus, T.; Rentrop, S.; Strohmeyer, R.; Vinnichenko, M.; Weling, T.; Stocker, H.; Meyer, D. C. Atomic layer deposition of TiO2 from tetrakis(dimethylamino) titanium and H2O. *Thin Solid Films* **2013**, *545*, 176-182. DOI: 10.1016/j.tsf.2013.07.076.
(41) Chang, J. P.; Lin, Y. S. Highly conformal ZrO2 deposition for dynamic random access memory application. *Journal of Applied Physics* **2001**, *90* (6), 2964-2969. DOI: 10.1063/1.1389756.
(42) Kukli, K.; Ritala, M.; Leskelä, M.; Sajavaara, T.; Keinonen, J.; Jones, A. C.; Roberts, J. L. Atomic Layer Deposition of Hafnium Dioxide Films from 1-Methoxy-2-methyl-2-propanolate Complex of Hafnium. *Chemistry of Materials* **2003**, *15* (8), 1722-1727. DOI: 10.1021/cm021328p.
(43) Musgrave, C. B., and Roy G Gordon. Precursors for Atomic Layer Deposition of High-k Dielectrics. *Future Fab International: Section 7 Process Gases, Chemicals and Materials* **2005**, *18*, 126-128.
(44) Lim, B. S.; Rahtu, A.; Gordon, R. G. Atomic layer deposition of transition metals. *Nature Materials* **2003**, *2* (11), 749-754. DOI: 10.1038/nmat1000.
(45) Park, T. J.; Sivasubramani, P.; Wallace, R. M.; Kim, J. Effects of growth temperature and oxidant feeding time on residual C- and N-related impurities and Si diffusion behavior in atomic-layer-deposited La2O3 thin films. *Applied Surface Science* **2014**, *292*, 880-885. DOI: 10.1016/j.apsusc.2013.12.072.
(46) Boysen, N.; Zanders, D.; Berning, T.; Beer, S. M. J.; Rogalla, D.; Bock, C.; Devi, A. Atomic layer deposition of dielectric Y2O3 thin films from a homoleptic yttrium formamidinate precursor and water. *Rsc Advances* **2021**, *11* (5), 2565-2574. DOI: 10.1039/d0ra09876k.
(47) Majumder, P.; Jursich, G.; Kueltzo, A.; Takoudis, C. Atomic Layer Deposition of Y[sub 2]O[sub 3] Films on Silicon Using Tris(ethylcyclopentadienyl) Yttrium Precursor and Water Vapor. *Journal of The Electrochemical Society* **2008**, *155* (8). DOI: 10.1149/1.2929825.
(48) Kim, W.-H.; Maeng, W. J.; Moon, K.-J.; Myoung, J.-M.; Kim, H. Growth characteristics and electrical properties of La2O3 gate oxides grown by thermal and plasma-enhanced atomic layer deposition. *Thin Solid Films* **2010**, *519* (1), 362-366. DOI: 10.1016/j.tsf.2010.07.108.
(49) Dickson, R. S.; Dobney, B. J.; Eastwood, F. W. PREPARATION OF CYCLOPENTADIENE FROM ITS DIMER. *Journal of Chemical Education* **1987**, *64* (10), 898-898. DOI: 10.1021/ed064p898.
(50) Niinistö, J.; Mäntymäki, M.; Kukli, K.; Costelle, L.; Puukilainen, E.; Ritala, M.; Leskelä, M. Growth and phase stabilization of HfO2 thin films by ALD using novel precursors. *Journal of Crystal Growth* **2010**, *312* (2), 245-249. DOI: 10.1016/j.jcrysgro.2009.10.028.
(51) Baek, J.-h.; Choi, W.-h.; Kim, H.; Cheon, S.; Byun, Y.; Jeon, W.; Park, J.-S. Plasma-enhanced atomic layer deposited HfO2 films using a novel heteroleptic cyclopentadienyl-based Hf precursor. *Ceramics International* **2021**, *47* (20), 29030-29035. DOI: 10.1016/j.ceramint.2021.07.065.

(52) Blanquart, T.; Niinisto, J.; Aslam, N.; Banerjee, M.; Tomczak, Y.; Gavagnin, M.; Longo, V.; Puukilainen, E.; Wanzenboeck, H. D.; Kessels, W. M. M.; et al. Zr(NEtMe)(2)(guan-NEtMe)(2) as a Novel Atomic Layer Deposition Precursor: ZrO2 Film Growth and Mechanistic Studies. *Chemistry of Materials* **2013**, *25* (15), 3088-3095. DOI: 10.1021/cm401279v.
(53) Cleary, J. M.; Arno, J. I.; Hendrix, B. C.; Naito, D.; Battle, S.; Gregg, J. N.; Wodjenski, M. J.; Xu, C. Solid precursor-based delivery of fluid utilizing controlled solids morphology. US 2007.
(54) Cassir, M.; Goubin, F.; Bernay, C.; Vernoux, P.; Lincot, D. Synthesis of ZrO2 thin films by atomic layer deposition: growth kinetics, structural and electrical properties. *Applied Surface Science* **2002**, *193* (1-4), 120-128. DOI: 10.1016/s0169-4332(02)00247-7.
(55) Mukhopadhyay, A. B.; Musgrave, C. B.; Fdez Sanz, J. Atomic layer deposition of hafnium oxide from hafnium chloride and water. *J Am Chem Soc* **2008**, *130* (36), 11996-12006. DOI: 10.1021/ja801616u From NLM PubMed-not-MEDLINE.

Chapter 2

Atomic Layer Deposition of Y_2O_3 Films Using Liquid Yttrium Precursor Tris(*sec*-butylcyclopentadienyl)yttrium and Water

ABSTRACT

Atomic layer deposition (ALD) of Y_2O_3 thin films was studied using a novel homoleptic yttrium ALD precursor: tris(*sec*-butylcyclopentadienyl)yttrium [$Y(^sBuCp)_3$]. $Y(^sBuCp)_3$ is a liquid at room temperature. The thermogravimetry curve for $Y(^sBuCp)_3$ is clean, with no indication of decomposition or residue formation. Thermogravimetry–differential thermal analysis measurements showed that $Y(^sBuCp)_3$ is stable for 18 weeks at 190 °C. $Y(^sBuCp)_3$ has a homoleptic structure. Thus, a reduction in manufacturing costs is expected compared with those associated with heteroleptic precursors because additional chemical synthesis steps are usually necessary to produce heteroleptic compounds. In addition, ALD of Y_2O_3 was demonstrated using $Y(^sBuCp)_3$ and water as a co-reactant. The deposition temperature was varied from 200 to 350 °C. The growth rate was 1.7 Å/cycle. In addition, neither carbon nor nitrogen contamination was detected in the Y_2O_3 films by X-ray photoelectron spectroscopy. Furthermore, smooth films were confirmed by X-ray secondary-electron microscopy. The root-mean-square roughness was measured to be 0.660 nm by atomic force microscopy. Metal–insulator–semiconductor (MIS) Pt–Y_2O_3–Si devices were fabricated to evaluate the electrical properties of the Y_2O_3 films. An electric breakdown field of −6.5 MV/cm and a leakage current density of ~3.2×10^{-3} A/cm^2 at 1 MV/cm were determined. The permittivity of Y_2O_3 was estimated to be 11.5 at 100 kHz. Therefore, compared with conventional solid precursors, $Y(^sBuCp)_3$ is suitable for use in ALD manufacturing processes.

INTRODUCTION

Yttrium oxide (Y_2O_3) is well known to exhibit attractive properties, including a high melting point (~2410 °C), high dielectric constant (~15), wide bandgap (~5.5 eV), and high refractive index. [1] It has been used in several industrial applications such as ceramics, dielectric insulators, superconductors, optical films, [2] protective films, [3] and buffer layers. In the energy field, thin-film solid oxide fuel cells (TF-SOFCs) are promising as next-generation high-efficiency energy sources. [4, 5] To fabricate TF-SOFCs, defect-free yttria-stabilized zirconia (YSZ) and yttria-doped ceria (YDC) electrolyte films with thicknesses less than 100 nm are required. [6-8] In microelectronics, Y_2O_3 is promising as a next-generation gate insulating film material. Recent studies have revealed that the dielectric constant (k) and crystal stability of materials such as ZrO_2, HfO_2, and La_2O_3 are improved by doping with Y_2O_3. [9-12] These Y_2O_3-containing thin films are mainly deposited by physical vapor deposition (PVD), [2, 11, 12] chemical vapor deposition (CVD), [3] or atomic layer deposition (ALD) [4, 6-9, 13] processes.

The importance of the ALD process has recently increased because of its ability to prepare thin films with a uniform smooth surface. [13, 14] However, almost all conventional yttrium ALD precursors are poorly suited for industrial use because they are solids at room temperature. As an example, tris(2,2,6,6,-tetramethyl-3,5-heptanedione)yttrium [$Y(thd)_3$] is the most commonly used yttrium ALD precursor. However, $Y(thd)_3$ is difficult to use in mass production processes because it is a solid and has a high melting point of 176 °C. The ALD growth rate [i.e., growth per cycle (GPC)] for $Y(thd)_3$ is 0.2 Å/cycle. [15] As an example, a film thickness greater than 100 nm is typically required for protective films; thus, a higher GPC is desirable. [3] When $Y(thd)_3$ is used in the ALD process, its GPC is low; hence, productivity is too low for thicker films to be obtained.

Several yttrium ALD precursors have been studied thus far. One such example is tris(*N*,*N*′-diisopropylacetamidinate) [$Y(^{i}Pr_2amd)_3$]. [16] It exhibits a relatively high ALD growth rate of 0.8 Å/cycle; however, its melting point is greater than 220 °C. Cyclopentadienyl-type ALD precursors have also been reported. Tris(cyclopentadienyl) yttrium [$Y(Cp)_3$] and tris(methylcyclopentadienyl) yttrium [$Y(MeCp)_3$] have high ALD growth rates of 1.5–1.8 and 1.2–1.3 Å/cycle, respectively. [17] However, their melting points are 296 and 124 °C, respectively.

Ideally, the melting point of yttrium ALD precursors should be lowered to overcome several problems, including clogging of supply lines, particle formation, and complex purification processes. Alkyl-Cp-type yttrium precursors [$Y(RCp)_3$], which have comparatively low melting points, have also been recently developed. [18-20] Tris(ethylcyclopentadienyl) yttrium [$Y(EtCp)_3$], tris(*n*-propylcyclopentadienyl) yttrium [$Y(^{n}PrCp)_3$], and tris(isopropylcyclopentadienyl) yttrium [$Y(^{i}PrCp)_3$] have melting points of 48, 66, and 55 °C, respectively. Tris(*n*-butylcyclopentadienyl) yttrium [$Y(^{n}BuCp)_3$] is a liquid precursor at room temperature, and a crystalline Y_2O_3 film has been prepared by ALD using [$Y(^{n}BuCp)_3$]. [21] However, with increasing alkyl chain lengths, the vapor pressure was

found to worsen compared with that for precursors with shorter chain lengths.

Another approach to improving several precursor properties is to develop heteroleptic precursors. The liquid yttrium ALD precursor (^{i}PrCp)$_2$Y(^{i}Pr-amd), which has a high vapor pressure and a growth rate of 0.6 Å/cycle, has been reported. [22] However, the synthetic routes for producing such heteroleptic precursors are usually complicated. In addition, the disproportionation reaction of the precursors must be suppressed. As a result, the cost of heteroleptic precursors is greater than that of homoleptic precursors.

Given the above considerations, from the perspectives of manufacturing cost, disproportionation reaction, melting point, and vapor pressure, we expected homoleptic alkyl-Cp-type yttrium precursors [Y(RCp)$_3$] to be promising as a basic structure; we therefore modified its alkyl chain structure. In the present study, the yttrium precursor tris(*sec*-butylcyclopentadienyl)yttrium(III) [Y(^{s}BuCp)$_3$] (Table 1), which is a liquid at room temperature, was developed. We carried out ALD testing using the [Y(^{s}BuCp)$_3$] precursor with water as a co-reactant.

Table 1 Composition of ALD precursors for yttrium oxide film.

Name	Y(thd)$_3$	Y(^{i}Pr-AMD)$_3$	Y(MeCp)$_3$	(^{i}PrCp)$_2$Y(^{i}Pr-AMD)	Y(^{s}BuCp)$_3$
Reference	15	16	17	22	This work
Structure	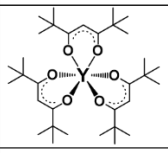	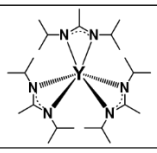	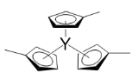	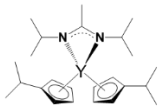	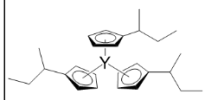
State	Solid	Solid	Solid	✓ Liquid	✓ Liquid
Ligand	✓ Homoleptic	✓ Homoleptic	✓ Homoleptic	Heteroleptic	✓ Homoleptic

EXPERIMENTAL

Characterization of Y(^{s}BuCp)$_3$ precursor

The ^{1}H-NMR data for Y(^{s}BuCp)$_3$ were obtained using a JEOL ECA-400. Thermogravimetric analysis (TGA) was carried out at 10 Torr in an Ar-filled glovebox using a Rigaku ThermoPlus2 TG8120. Thermal decomposition temperature was measured by differential scanning calorimetry (DSC) with a Bruker AXS DSC 3100.

ALD testing of Y(^{s}BuCp)$_3$ precursor with water

Y_2O_3 films were deposited using a commercial ALD apparatus (NCD Lucida D100) equipped with a cross-flow ALD reactor; water was used as the co-reactant. Prior to deposition, Si(100) substrates were cut to 25 mm × 25 mm and subsequently cleaned with 0.5% HF solution for 1 min to remove the native oxide layer. The cleaned wafers were dried using N_2 gas and immediately loaded into the ALD chamber. Before the ALD process, the wafer was heated for 30 min to stabilize

its temperature. The $Y(^{s}BuCp)_3$ was provided by ADEKA (CAS no. 847153-22-4, product name: Y-5000). The $Y(^{s}BuCp)_3$ precursor was added to a stainless steel canister and heated at 175 °C. The precursor supply method was vapor drawing using Ar carrier gas at 50 sccm. The chamber pressure was controlled at ~0.75 Torr by Ar process gas.

Characterization of deposited Y_2O_3 films

Yttrium deposition was measured by X-ray fluorescence (XRF) analysis using a Rigaku ZSX Primus IVi. The stoichiometry and elemental bonding states in the films were characterized by X-ray photoelectron spectroscopy (XPS) using a Thermo Fisher Scientific K-Alpha. The film morphology and thickness were studied by field-emission scanning electron microscopy (FE-SEM) and atomic force microscopy (AFM) with a Hitachi High-Tech S-4800 and a Bruker Multimode 8, respectively. The scanning mode in AFM measurement is “Peak Force Tapping”. The tip for AFM is Bruker SCANASYST-AIR. The film thickness and the crystallinity were evaluated by X-ray reflectivity (XRR) and X-ray diffraction (XRD) measurements using a Rigaku Ultima IV.

Electric characterization of Y_2O_3 films

The electric properties of the obtained Y_2O_3 films were evaluated by preparing metal–insulator–semiconductor (MIS) structures of Pt/Y_2O_3/*p*-Si. The deposition temperature of the Y_2O_3 layer was 300 °C. The Pt electrodes were deposited onto the Y_2O_3 films through a shadow mask at room temperature by DC magnetron sputtering using a Sanyu Electron SC-701MC. The thicknesses of the Pt electrode, Y_2O_3 layer, and *p*-Si substrate were 100 nm, 19.4 nm, and 0.5 mm, respectively. Capacitance–voltage (*C–V*) curves for the MIS structure were recorded using a precision LCR meter (Agilent, 4980A). The current–voltage (*I–V*) curves were also acquired (Keithley, Sourcemeter 2450). The probe station was coaxial probe.

RESULTS AND DISCUSSION

Chemical identification of $Y(^{s}BuCp)_3$ precursor

The synthesized $Y(^{s}BuCp)_3$ was confirmed by ^{1}H-NMR measurement. Figure 1 shows the ^{1}H-NMR spectrum of $Y(^{s}BuCp)_3$. The signal of each proton on the cyclopentadienyl ring appeared at 6.011 and 5.866 ppm as a multiplet. The coupling to the proton on the tertiary carbon atom showed as a hexaplet at 2.489 ppm. The methyl group on the *sec*-butyl group showed as a multiplet at 0.982 ppm. The ethyl group on the *sec*-butyl group showed as a multiplet at 1.391 ppm (2 H) and a triplet at 0.819 ppm (3 H). Each peak was overlapped or a multiplet because the *sec*-butyl Cp ligand has a stereocenter on the alpha carbon. On the basis of the ^{1}H NMR analysis results, $Y(^{s}BuCp)_3$ was considered a chiral compound.

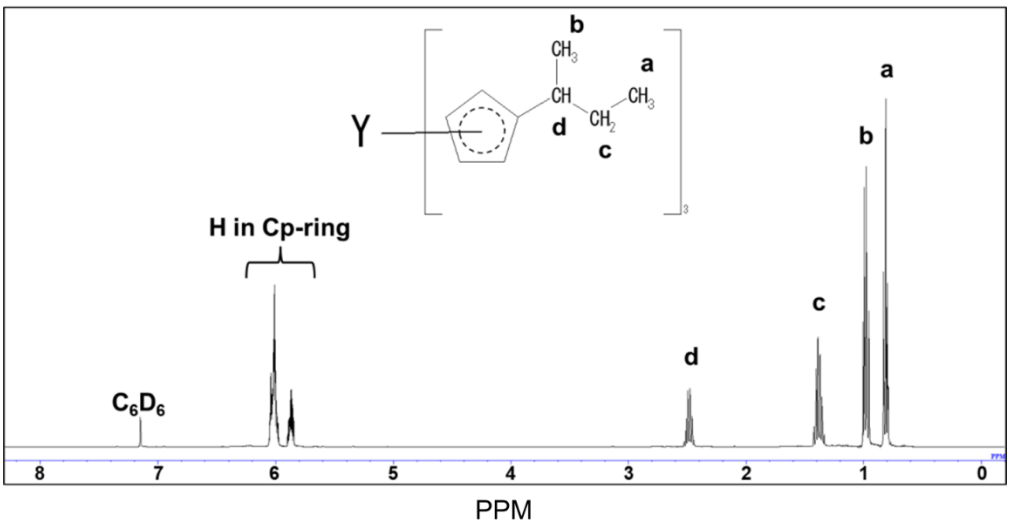

Fig. 1 ^{1}H-NMR spectrum of Y(^{s}BuCp)$_3$.

Figure 2 shows the vapor pressure variations with temperature of the Y(^{s}BuCp)$_3$ precursor. The vapor pressure of Y(^{s}BuCp)$_3$ was 0.1 Torr at 149 °C. The vapor pressure of Y(^{n}BuCp)$_3$ has been reported to be 0.1 Torr at 150 °C. [20] Thus, the introduction of a branched alkyl structure slightly improved the vapor pressure.

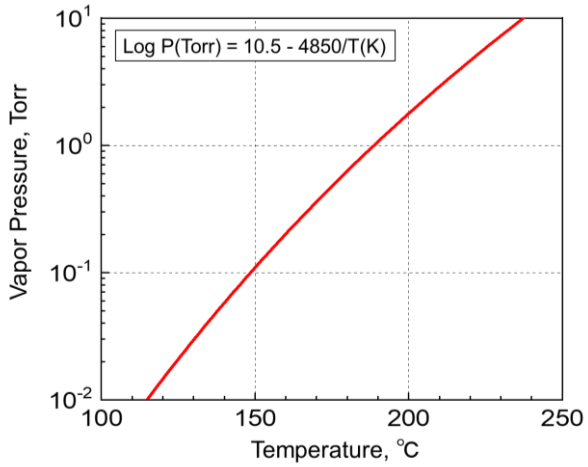

Fig. 2 Vapor pressure variations of Y(^{s}BuCp)$_3$ with temperature.

Figure 3(a) shows the TGA curves for Y(^{s}BuCp)$_3$ and conventional precursors such as the solid precursor Y(EtCp)$_3$ and the liquid precursor Y(^{n}BuCp)$_3$. The curve for Y(^{s}BuCp)$_3$ is clean, with no indication of decomposition or residue formation at 10 Torr. The 50% volatile temperature ($TG_{1/2}$) was 197 °C. The $TG_{1/2}$ for Y(EtCp)$_3$ was 186 °C; it thus exhibits greater volatility than Y(^{s}BuCp)$_3$

even though it is a solid. Compared with Y(^{n}BuCp)$_3$, Y(^{s}BuCp)$_3$ exhibits greater volatility. The $TG_{1/2}$ for Y(^{n}BuCp)$_3$ was 219 °C because of its linear and alkyl chain structure. For hydrocarbon molecules with the same molecular weight, a compound with a branched structure will exhibit a lower boiling point than one with a linear structure. [23] A branched alkyl chain of the precursor is critical for achieving greater volatility. With the introduction of a *sec*-butyl group, the volatility of the Y(^{s}BuCp)$_3$ precursor was improved and became similar to that of the Y(EtCp)$_3$ precursor.

Figure 3(b) shows DSC thermograms for the Y(^{s}BuCp)$_3$ and conventional precursors. A thermal decomposition peak was not observed at a temperature less than 400 °C for any of the precursors. These results indicate that the Y(RCp)$_3$ base structure exhibits high thermal stability. Y(^{s}BuCp)$_3$ and Y(^{n}BuCp)$_3$ were liquid precursors; melting was therefore not observed in the investigated temperature range. Y(^{s}BuCp)$_3$ has three chiral centers; thus, four types of diastereomers are possible, excluding enantiomers, because it contains eight stereoisomer structures (i.e., RRR, SRR, RRS, SRS, RSR, SSR, RSS, and SSS). In general, stereoisomer mixtures have lower melting points than single-structure compounds because of poor crystallization of the molecule. [24] Y(^{s}BuCp)$_3$ is expected to have a lower melting point than Y(^{n}BuCp)$_3$. That is, Y(^{s}BuCp)$_3$ is expected to remain a liquid over a wide temperature range.

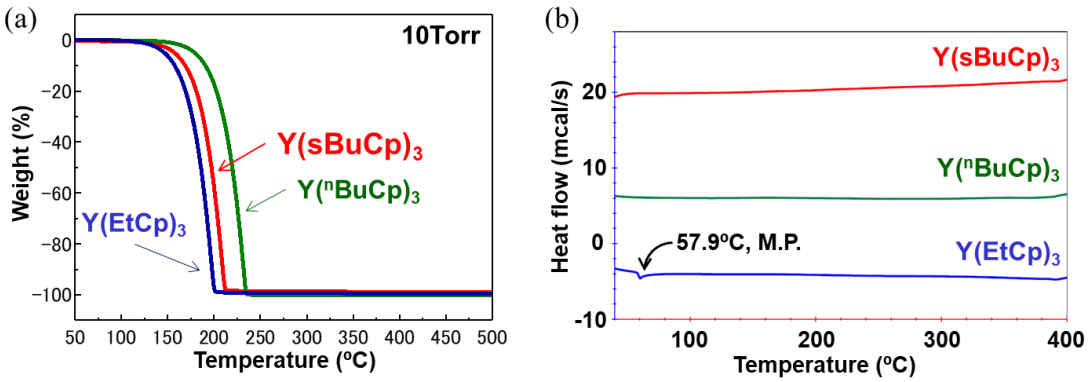

Fig. 3 (a) TGA curves for Y(^{s}BuCp)$_3$ and conventional precursors Y(EtCp)$_3$ and Y(^{n}BuCp)$_3$ (b) DSC thermograms of Y(^{s}BuCp)$_3$ and conventional precursors Y(EtCp)$_3$ and Y(^{n}BuCp)$_3$

Long-term thermal stability of Y(^{s}BuCp)$_3$ precursor

An ALD precursor is heated to a high temperature during the ALD process. Long-term thermal stability at the vaporization temperature for more than a few months is critical for ALDs used industrially, where long-life precursors enable films to be continuously produced without stopping the production line. The DSC results indicate that Y(RCp)$_3$-type complexes exhibit high thermal stability. We therefore evaluated the long-term thermal stability of Y(^{s}BuCp)$_3$ as a novel compound. Figure 4 (a) shows TGA curves recorded during the long-term thermal stability test. The Y(^{s}BuCp)$_3$ was heated

at 190 °C, which is the temperature at which it vaporizes at 1 Torr, and periodically characterized by TGA and ^{1}H-NMR. The results show very clean TG curves before and after the sample was heated at 190 °C for 18 weeks.

Figure 4 (b) presents ^{1}H-NMR spectra acquired during the long-term thermal stability test. The spectrum of Y(^{s}BuCp)$_3$ did not change before or after it was heated at 190 °C for 18 weeks. Therefore, Y(^{s}BuCp)$_3$ was confirmed to exhibit excellent long-term thermal stability for at least 18 weeks.

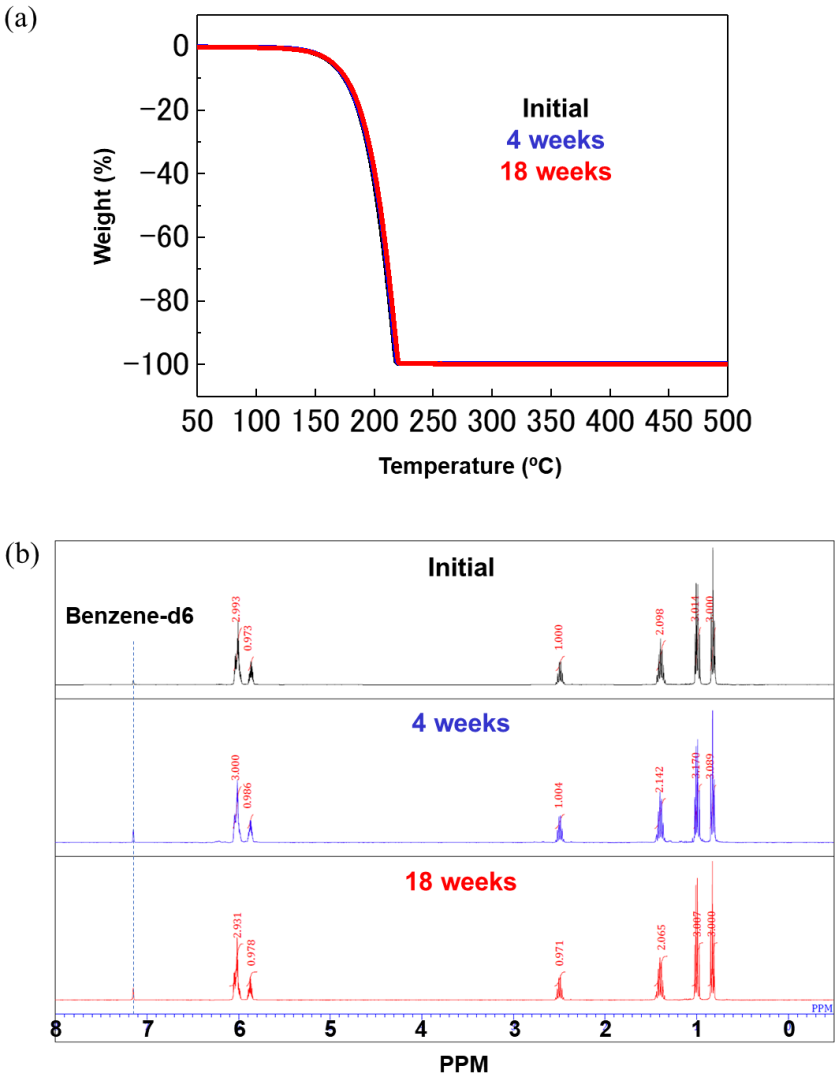

Fig. 4 (a) TGA curves recorded during long-term thermal stability test of Y(^{s}BuCp)$_3$ at 190 °C for 18 weeks. (b) ^{1}H-NMR spectra of Y(^{s}BuCp)$_3$ acquired during long-term thermal stability test at 190 °C for 18 weeks.

ALD testing of $Y(^sBuCp)_3$ precursor with water

The ALD sequence involves dosing and purging steps for the metal complex, and the use of a co-reactant. The dosing and purging times should be optimized to enable the fabrication of ultra-thin, conformal films with high uniformity. Experiments to determine the optimal dosing and purging times were carried out for ALD of Y_2O_3 using the $Y(^sBuCp)_3$ precursor with water as a co-reactant. To remove the moisture in the ALD chamber, various water purge times were investigated at 250 °C. Figure 5 (a) shows that a higher growth rate was achieved at 10 and 30 s, although a constant growth rate was observed when the purge time was longer than 60 s. The results show that adsorption of $Y(^sBuCp)_3$ was affected by remaining moisture when the water purge time was shorter than 30 s in our ALD reactor. Therefore, the deposition was carried out using a water purge time of 60 s.

Figure 5 (b) shows that saturation occurred when the $Y(^sBuCp)_3$ supply time on the Si substrate was varied at 250 °C. The results show that self-limited film growth occurred. The $Y(^sBuCp)_3$ was confirmed to be saturated when the supply time was 30 s or longer. Under our experimental conditions, the saturation time was long compared with those for conventional precursors. [17, 18, 21] $Y(^sBuCp)_3$ exhibits volatility similar to that of $Y(RCp)_3$; we therefore considered that this difference was caused by our experimental conditions. To reduce the saturation time, the partial pressure of $Y(^sBuCp)_3$ should be increased in the ALD chamber to improve precursor adsorption onto the substrate. For further improvement, a higher precursor heating temperature and bubbling of the precursor supply are promising. The saturated film growth rate was ~1.7 Å/cycle at 250 °C.

The $Y(^sBuCp)_3$ purge time was also optimized. Figure 5 (c) shows the $Y(^sBuCp)_3$ purge time dependence of the film growth rate at 250 °C. A constant growth rate was observed when the purge time was 15 s or longer. Small variations in the growth rate were confirmed at shorter purge times because of incomplete purging of the metal precursor. Because carbon contamination originating from the ligand was a concern in this range of short purge times, a purge time of at least 15 s was considered necessary.

On the basis of the above results, the standard pulsing ALD sequence was designed as follows: 30 s supply of metal precursor with carrier gas, followed by 15 s Ar purge, 0.2 s pulse of water, and finally 60 s purge with Ar gas. We used this standard sequence to evaluate the ALD behavior of $Y(^sBuCp)_3$.

Figure 5 (d) shows the film thickness as a function of the number of ALD cycles. The film thickness was measured by XRR. The thickness increased linearly with increasing number of ALD cycles at 250 and 300 °C. These results indicate that the film grew at a constant rate; thus, $Y(^sBuCp)_3$ demonstrated excellent thickness control characteristics. The results thus far verify the linear dependence and the saturation behavior; we therefore concluded that $Y(^sBuCp)_3$ exhibits an ALD-type growth mode.

ALD behavior of $Y(^sBuCp)_3$ at 250 °C was confirmed; we therefore next investigated the

deposition temperature dependence in the range 200–350 °C. Figure 5 (e) shows the growth rate at various deposition temperatures. In this experiment, Y_2O_3 films were deposited by ALD onto Si substrates for 50 cycles. The growth rate reached 1.5 Å/cycle at 250 °C. The maximal growth rate at 300 °C was found to be 1.8 Å/cycle. The growth rate was 1.3–1.8 Å/cycle in the temperature range 200–350 °C. These values are similar to those reported for thermal ALD of Y_2O_3 using cyclopentadienyl yttrium precursors such as $Y(Cp)_3$, $Y(MeCp)_3$, $Y(EtCp)_3$, $Y(iPrCp)_3$, and $Y(^nBuCp)_3$.[17, 18, 21, 25] The growth rate decreased with increasing deposition temperature beyond 300 °C. The yttrium intensity detected by XRF also decreased when the deposition temperature was greater than 300 °C because $Y(^sBuCp)_3$ was desorbed as a result of the greater thermal energy at higher temperatures during the ALD process. According to the DSC measurement results, the thermal decomposition temperature of $Y(^sBuCp)_3$ is greater than 400 °C. Thus, we deduced that the decrease in the growth rate was not a result of thermal decomposition but rather desorption at higher temperatures.

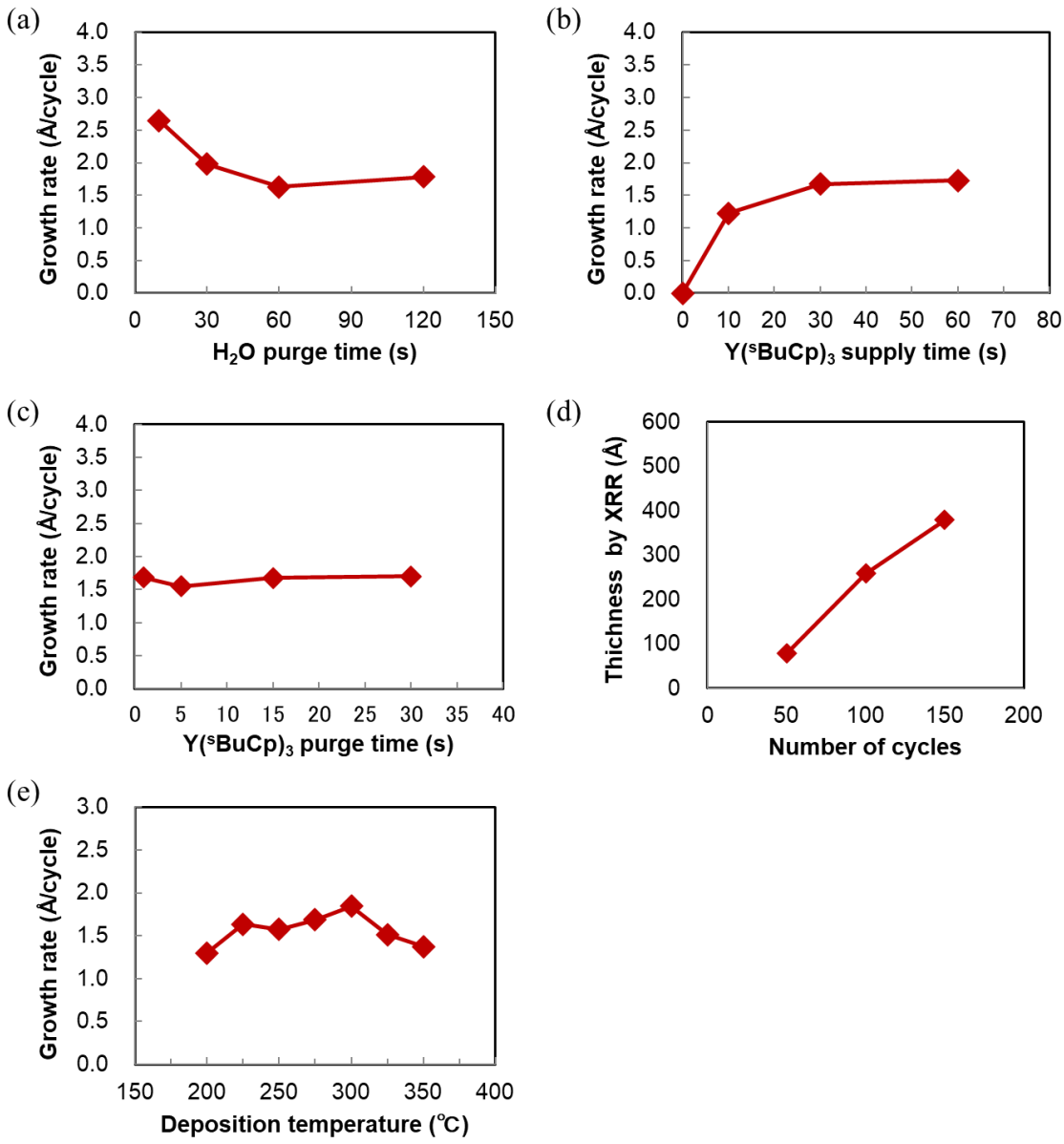

Fig. 5 (a) Growth rate for Y_2O_3 films as function of water purge time at 250 °C. (b) Saturation of Y_2O_3 film growth rate with increasing $Y(^sBuCp)_3$ supply time at 250 °C. (c) Y_2O_3 film growth rate as function of the $Y(^sBuCp)_3$ purge time at 250 °C. (d) Film thickness as function of number of ALD cycles at 250. (e) Growth rate for Y_2O_3 films as function of deposition temperature.

We compared the growth rate achieved using $Y(^sBuCp)_3$ as a precursor with those achieved using conventional precursors. $Y(thd)_3$ showed a low growth rate of 0.2 Å/cycle with O_3 as a co-reactant. [10] $Y(^iPr_2amd)_3$ enabled Y_2O_3 film growth at 0.8 Å/cycle. [11] The heteroleptic precursor $(^iPrCp)_2Y(^iPr\text{-}amd)$ showed a growth rate of 0.6 Å/cycle. [16] We concluded that $Y(^sBuCp)_3$ enables a higher growth rate than the conventional precursors, thereby enabling greater productivity of Y_2O_3

films.

Film properties of $Y(^{s}BuCp)_3$ precursor with water

The film concentration and impurities in the films were measured by XPS analysis. Figure 6 (a-c) shows XPS depth profiles for films deposited at (a) 200 °C, (b) 250 °C, and (c) 300 °C. The results confirm that high-purity Y_2O_3 was deposited at all three investigated temperatures. The oxygen concentration slightly increased with increasing deposition temperature. For the above films, the Y/O ratio was found to be 0.74, 0.71, and 0.69, respectively, indicating the formation of hydroxylated or reduced Y_2O_{3-x} at low deposition temperatures.

Figure 6 (d-f) shows the Y 3*d*, O 1*s*, and C 1*s* regions of the XPS spectra of the deposited films. The Y main peaks (d) appeared at 156.8 and 158.8 eV. The O 1*s* spectra (e) of the Y_2O_3 films show a Y–O peak at ~529.5 eV. The peak at 200 °C was shifted to lower energy because of an insufficient oxidation reaction due to the low deposition temperature. No peak attributable to Y–OH was observed in the spectra of any of the films. In addition, neither C (f) nor N impurities were detected in any of the films.

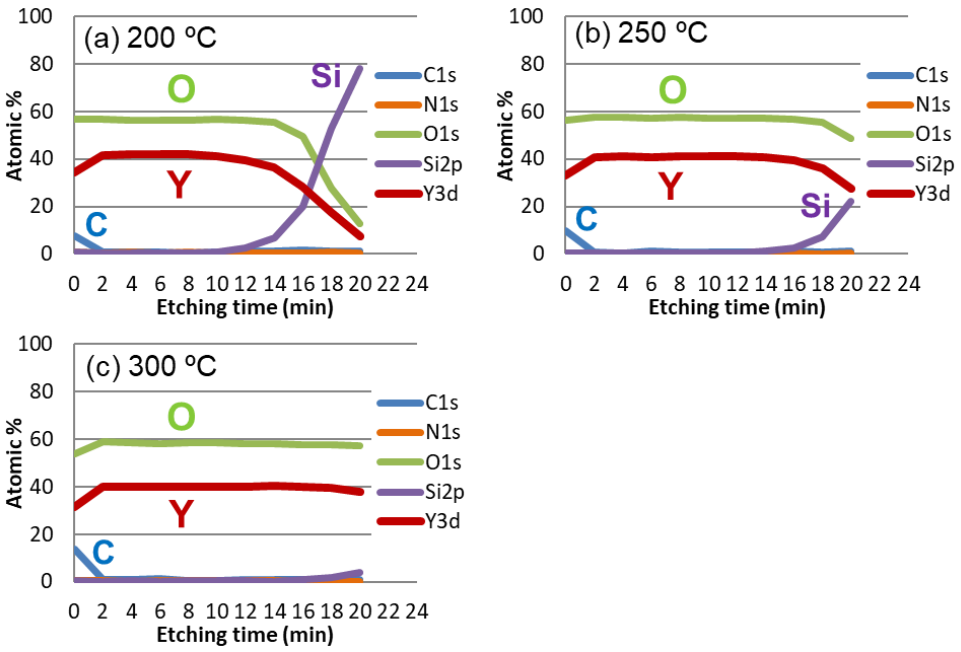

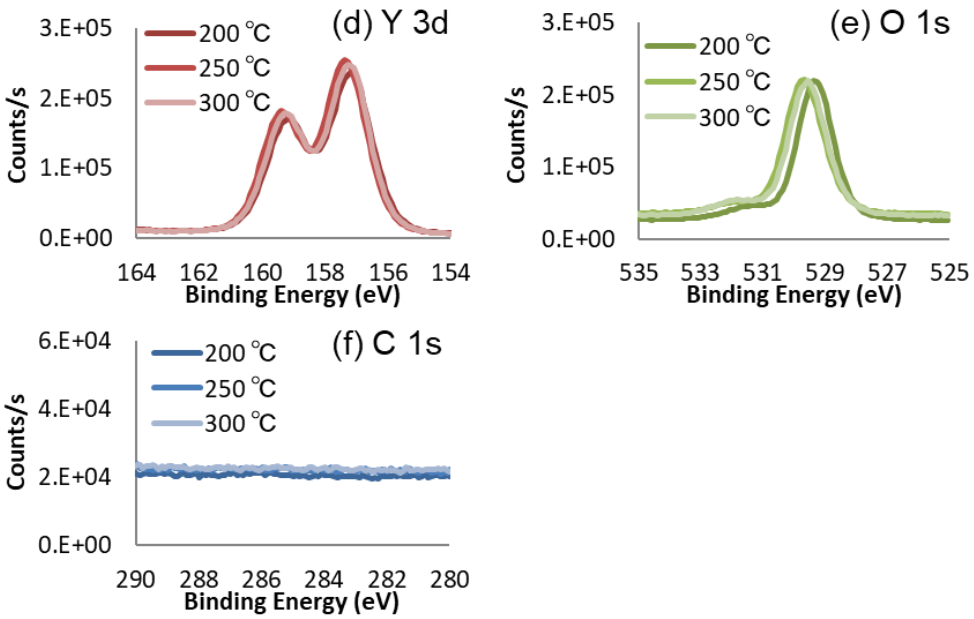

Fig. 6 XPS depth profiles for Y_2O_3 films deposited at (a) 200 °C, (b) 250 °C, and (c) 300 °C. XPS spectra of Y_2O_3 films deposited at (d) 200 °C, (e) 250 °C, and (f) 300 °C.

Figure 7 (a) shows FE-SEM images of the Y_2O_3 films deposited onto *p*-type Si(100) substrates. Continuous films with a smooth surface and a thickness of 23.1 nm were deposited at 200 °C. Isolated particles were not detected on the surface.

Figure 7 (b) shows a three-dimensional AFM image of a Y_2O_3 film deposited onto a *p*-type Si(100) substrate at 200 °C. The film thickness was 23.1 nm, and the scanned area was 1.0 μm × 1.0 μm. The imaging results indicate that the film had a smooth surface. The root mean square (RMS) roughness determined by AFM measurement was 0.66 nm, which is lower than the roughness values of Y_2O_3 films deposited using conventional precursors. [16, 17]

Figure 7 (c) shows that the 23.1-nm-thick Y_2O_3 film on a Si substrate was crystalline, as indicated by XRD measurements. The results confirmed that the as-deposited Y_2O_3 film was crystallized without annealing. Peaks associated with (222), (400), (332), (431), (440), and (622) planes were observed, indicating that the crystal phase is mainly cubic. [26, 27] A monoclinic-rich film can be deposited at high temperatures. In addition, the structure of the film is affected by the oxygen partial pressure, deposition pressure, and the substrate. The XRD pattern showed no additional peaks caused by impurities.

These film characterization results confirm that the $Y(^sBuCp)_3$ precursor can easily provide a high-quality Y_2O_3 film.

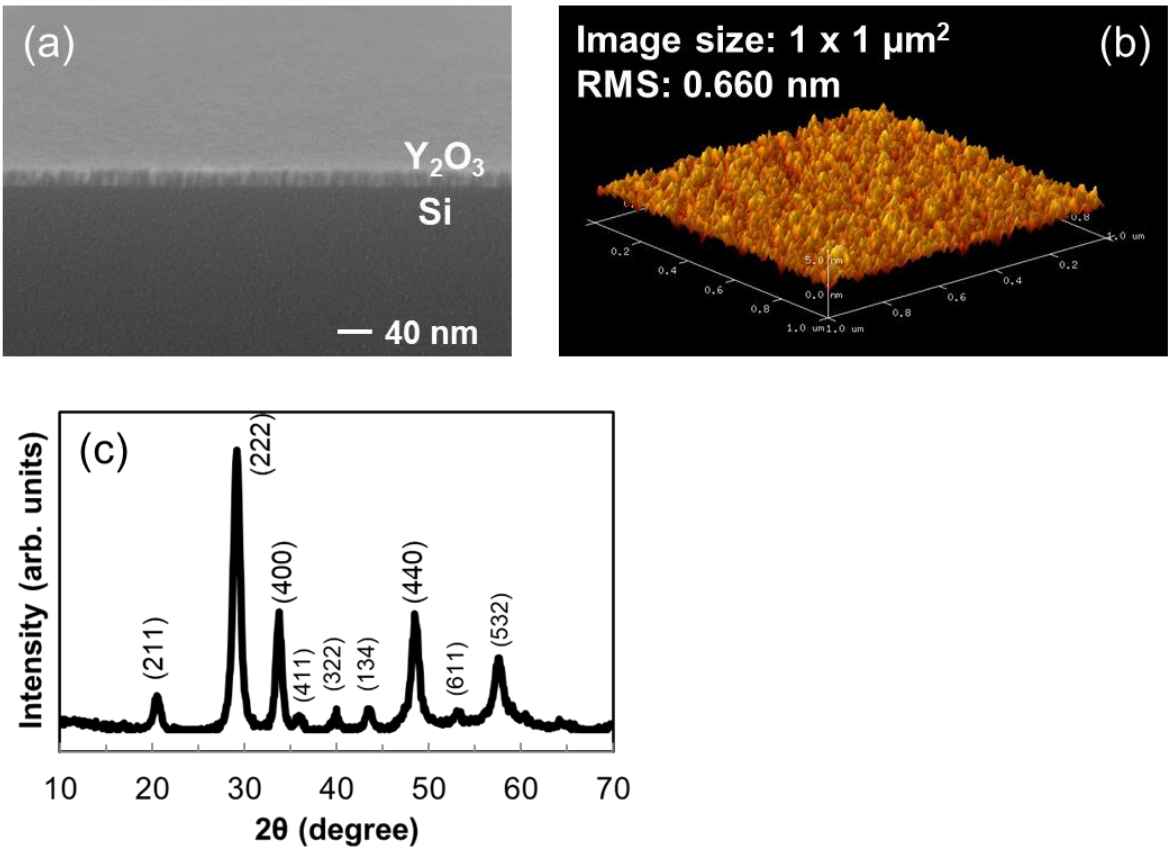

Fig. 7 (a) FE-SEM image of Y_2O_3 film deposited onto Si substrate at 200 °C. (b) Three-dimensional AFM image of Y_2O_3 film deposited onto Si substrate at 200 °C. (c) XRD pattern for Y_2O_3 film on Si substrate. The reflections were indexed on the basis of PDF card no. 151761.

Electric properties of Y_2O_3 films

Figure 8 (a) shows *C–V* curves for a Pt/Y_2O_3/*p*-Si MIS capacitor. The thickness and deposition temperature of the Y_2O_3 layer were 19.4 nm and 300 °C, respectively, and the area of the Pt top electrode was 0.0154 mm^2. The measurement was conducted at 25 °C and a frequency of 100 kHz. The voltage range was from 3 V to –3 V. The sweep rate was 0.48 V/s. When a negative bias was applied, the capacitance value was 80 pF. From these results, the dielectric constant for the Y_2O_3 layer was estimated to be 11.5, which is similar to previously reported values of ~10 ($Y(Cp)_3$ and $Y(MeCp)_3$).[17, 28] However, when a positive bias was applied to the MIS capacitor, the capacitance substantially decreased because of the formation of a depletion layer in the *p*-Si.

Figure 8 (b) shows leakage current density vs. electric field curves for the Pt/Y_2O_3/*p*-Si MIS capacitor. The voltage range was from 0 V to –20 V. The sweep rate and compliance current were 0.48 V/s and 100 mA, respectively. The leakage current density at 1 MV/cm and breakdown electric field were approximately 3.2×10^{-3} A/cm^2 and 6.5 MV/cm, respectively. These values are comparable to those for a previously reported MIS capacitor fabricated using a Y_2O_3 layer prepared from solid or

heteroleptic ALD precursors. [17, 29] Thus, these results indicate that a Y_2O_3 layer with high electronic performance could be attained even when a liquid homoleptic ALD precursor was used.

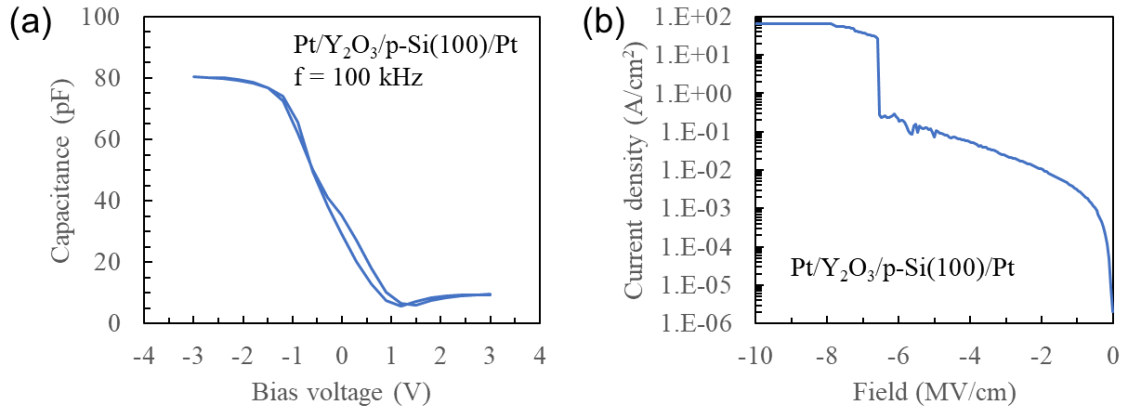

Fig. 8 (a) *C–V* curves for Pt/Y_2O_3/*p*-Si capacitor. The deposition temperature for the Y_2O_3 layer was 300 °C. (b) Leakage current density vs. electric field curves for Pt/Y_2O_3/*p*-Si capacitor. The deposition temperature for the Y_2O_3 layer was 300 °C.

SUMMARY AND CONCLUSIONS

We have demonstrated ALD of Y_2O_3 films using a newly developed yttrium precursor, $Y(^sBuCp)_3$. $Y(^sBuCp)_3$ is a liquid at room temperature and exhibits high volatility because of its branched alkyl chain structure. In addition, a lower melting point is expected because of its stereoisomerism. This molecular design imparted the precursor with industrially preferred properties. $Y(^sBuCp)_3$ also exhibits high thermal stability, exhibiting a lifetime of at least 18 weeks at 190 °C. This evaluation is ongoing, so the lifetime might be longer than 18 weeks. In addition, like the conventional $Y(RCp)_3$ precursor, $Y(^sBuCp)_3$ exhibits a high growth rate and a wide ALD window. The deposited Y_2O_3 films exhibit high purity, high crystallinity, and a smooth surface. The Y_2O_3 films prepared from $Y(^sBuCp)_3$ also exhibit high electronic performance. Therefore, we conclude that $Y(^sBuCp)_3$ is an attractive Y_2O_3 precursor for industrial use.

ACKNOWLEDGMENTS

We are grateful to ADEKA for providing the $Y(^sBuCp)_3$ precursor and ^{1}H-NMR, vapor pressure, TGA, and DSC data.

This work was partly supported by “Crossover Alliance to Create the Future with People, Intelligence and Materials” and Advanced Research Infrastructure for Materials and Nanotechnology (ARIM) Japan from the Ministry of Education, Culture, Sports, Science and Technology (MEXT).

REFERENCES

(1) Hubbard, K. J.; Schlom, D. G. Thermodynamic stability of binary oxides in contact with silicon. *Journal of Materials Research* **1996**, *11* (11), 2757-2776. DOI: 10.1557/jmr.1996.0350.

(2) Atanassov, G.; Thielsch, R.; Popov, D. Optical properties of TiO2, Y2O3 and CeO2 thin films deposited by electron beam evaporation. *Thin Solid Films* **1993**, *223* (2), 288-292. DOI: 10.1016/0040-6090(93)90534-v.

(3) Bonnet, G.; Lachkar, M.; Larpin, J. P.; Colson, J. C. Organometallic chemical vapor deposition of rare earth oxide thin films. Application for steel protection against high temperature oxidation. *Solid State Ionics* **1994**, *72*, 344-348. DOI: 10.1016/0167-2738(94)90171-6.

(4) Chang, I.; Ji, S.; Park, J.; Lee, M. H.; Cha, S. W. Ultrathin YSZ Coating on Pt Cathode for High Thermal Stability and Enhanced Oxygen Reduction Reaction Activity. *Advanced Energy Materials* **2015**, *5* (10). DOI: 10.1002/aenm.201402251.

(5) Park, J.; Chang, I.; Paek, J. Y.; Ji, S.; Lee, W.; Cha, S. W.; Lee, J.-M. Fabrication of the large area thin-film solid oxide fuel cells. *CIRP Annals* **2014**, *63* (1), 513-516. DOI: 10.1016/j.cirp.2014.03.065.

(6) Shim, J. H.; Chao, C. C.; Huang, H.; Prinz, F. B. Atomic layer deposition of yttria-stabilized zirconia for solid oxide fuel cells. *Chemistry of Materials* **2007**, *19* (15), 3850-3854. DOI: 10.1021/cm070913t.

(7) Fan, Z.; Chao, C.-C.; Hossein-Babaei, F.; Prinz, F. B. Improving solid oxide fuel cells with yttria-doped ceria interlayers by atomic layer deposition. *Journal of Materials Chemistry* **2011**, *21* (29). DOI: 10.1039/c1jm11550b.

(8) Park, J.; Lee, Y.; Chang, I.; Cho, G. Y.; Ji, S.; Lee, W.; Cha, S. W. Atomic layer deposition of yttria-stabilized zirconia thin films for enhanced reactivity and stability of solid oxide fuel cells. *Energy* **2016**, *116*, 170-176. DOI: 10.1016/j.energy.2016.09.094.

(9) Bernay, C.; Ringuedé, A.; Colomban, P.; Lincot, D.; Cassir, M. Yttria-doped zirconia thin films deposited by atomic layer deposition ALD: a structural, morphological and electrical characterisation. *Journal of Physics and Chemistry of Solids* **2003**, *64* (9-10), 1761-1770. DOI: 10.1016/s0022-3697(03)00105-7.

(10) Wang, S. J.; Ong, C. K.; Xu, S. Y.; Chen, P.; Tjiu, W. C.; Huan, A. C. H.; Yoo, W. J.; Lim, J. S.; Feng, W.; Choi, W. K. Electrical properties of crystalline YSZ films on silicon as alternative gate dielectrics. *Semiconductor Science and Technology* **2001**, *16* (3), L13-L16. DOI: 10.1088/0268-1242/16/3/101.

(11) Zhao, Y.; Kita, K.; Kyuno, K.; Toriumi, A. Higher-k LaYOx films with strong moisture resistance. *Applied Physics Letters* **2006**, *89* (25). DOI: 10.1063/1.2420794.

(12) Dai, J. Y.; Lee, P. F.; Wong, K. H.; Chan, H. L. W.; Choy, C. L. Epitaxial growth of yttrium-stabilized HfO2 high-kgate dielectric thin films on Si. *Journal of Applied Physics* **2003**, *94* (2),

912-915. DOI: 10.1063/1.1585116.
(13) Paek, J. Y.; Chang, I.; Park, J. H.; Ji, S.; Cha, S. W. A study on properties of yttrium-stabilized zirconia thin films fabricated by different deposition techniques. *Renewable Energy* **2014**, *65*, 202-206. DOI: 10.1016/j.renene.2013.08.043.
(14) George, S. M. Atomic Layer Deposition: An Overview. *Chemical Reviews* **2010**, *110* (1), 111-131. DOI: 10.1021/cr900056b.
(15) Putkonen, M.; Sajavaara, T.; Johansson, L. S.; Niinistö, L. Low-Temperature ALE Deposition of Y2O3 Thin Films from β-Diketonate Precursors. *Chemical Vapor Deposition* **2001**, *7* (1), 44-50. DOI: 10.1002/1521-3862(200101)7:1<44::Aid-cvde44>3.0.Co;2-q.
(16) de Rouffignac, P.; Park, J.-S.; Gordon, R. G. Atomic Layer Deposition of Y2O3 Thin Films from Yttrium Tris(N,N'-diisopropylacetamidinate) and Water. *Chemistry of Materials* **2005**, *17* (19), 4808-4814. DOI: 10.1021/cm050624+.
(17) Niinistö, J.; Putkonen, M.; Niinistö, L. Processing of Y2O3 Thin Films by Atomic Layer Deposition from Cyclopentadienyl-Type Compounds and Water as Precursors. *Chemistry of Materials* **2004**, *16* (15), 2953-2958. DOI: 10.1021/cm040145v.
(18) Majumder, P.; Jursich, G.; Kueltzo, A.; Takoudis, C. Atomic Layer Deposition of Y[sub 2]O[sub 3] Films on Silicon Using Tris(ethylcyclopentadienyl) Yttrium Precursor and Water Vapor. *Journal of The Electrochemical Society* **2008**, *155* (8). DOI: 10.1149/1.2929825.
(19) Dubourdieu, C. Y2O3 films grown by a novel ALD process from Y(EtCp)3 and water enabling Y-based silicates in direct contact with Si with sub-nm EOTs In ALD conference, 2011.
(20) Blasco, N. Recent Development of Ligand Chemistries for Next Generation Conformal PEALD/ALD of Metal & Oxides. In ALD conference, Kyoto, Japan; 2014.
(21) Abdulagatov, A. I.; Amashaev, R. R.; Ashurbekova, K. N.; Ramazanov, S. M.; Palchaev, D. K.; Maksumova, A. M.; Rabadanov, M. K.; Abdulagatov, I. M. Atomic Layer Deposition of Y2O3 Using Tris(butylcyclopentadienyl)yttrium and Water. *Russian Microelectronics* **2019**, *48* (1), 1-12. DOI: 10.1134/s1063739719010025.
(22) Park, I.-S.; Chan Jung, Y.; Seong, S.; Ahn, J.; Kang, J.; Noh, W.; Lansalot-Matras, C. Atomic layer deposition of Y2O3 films using heteroleptic liquid (iPrCp)2Y(iPr-amd) precursor. *J. Mater. Chem. C* **2014**, *2* (43), 9240-9247. DOI: 10.1039/c4tc01405g.
(23) Bruice, P. Y. *Handbook of Organic Chemistry Fifth Edition*; Kagakudojin, 2009.
(24) Prankerd, R. J.; Elsabee, M. Z. Thermal analysis of chiral drug mixtures: the DSC behavior of mixtures of ephedrine HCl and pseudoephedrine HCl enantiomers. *Thermochimica Acta* **1995**, *248*, 147-160. DOI: 10.1016/0040-6031(94)01885-k.
(25) Xu, R.; Selvaraj, S. K.; Azimi, N.; Takoudis, C. G. Growth Characteristics and Properties of Yttrium Oxide Thin Films by Atomic Layer Deposition from Novel Y(iPrCp)3 Precursor and O3. *ECS Transactions* **2013**, *50* (13), 107-116. DOI: 10.1149/05013.0107ecst.

(26) Jayasankar, K.; Pandey, A.; Mishra, B. K.; Das, S. Evaluation of microstructural parameters of nanocrystalline Y2O3 by X-ray diffraction peak broadening analysis. *Materials Chemistry and Physics* **2016**, *171*, 195-200. DOI: 10.1016/j.matchemphys.2016.01.005.
(27) Marder, R.; Chaim, R.; Chevallier, G.; Estournes, C. Densification and polymorphic transition of multiphase Y2O3 nanoparticles during spark plasma sintering. *Materials Science and Engineering: A* **2011**, *528* (24), 7200-7206. DOI: 10.1016/j.msea.2011.06.044.
(28) Boysen, N.; Zanders, D.; Berning, T.; Beer, S. M. J.; Rogalla, D.; Bock, C.; Devi, A. Atomic layer deposition of dielectric Y2O3 thin films from a homoleptic yttrium formamidinate precursor and water. *Rsc Advances* **2021**, *11* (5), 2565-2574. DOI: 10.1039/d0ra09876k.
(29) Lee, J.-S.; Kim, W.-H.; Oh, I.-K.; Kim, M.-K.; Lee, G.; Lee, C.-W.; Park, J.; Lansalot-Matras, C.; Noh, W.; Kim, H. Atomic layer deposition of Y2O3 and yttrium-doped HfO2 using a newly synthesized Y(iPrCp)2(N-iPr-amd) precursor for a high permittivity gate dielectric. *Applied Surface Science* **2014**, *297*, 16-21. DOI: 10.1016/j.apsusc.2014.01.032.

Chapter 3

Atomic Layer Deposition of HfO_2 Films Using Novel Cl-Free Hafnium Precursor Tetrakis(1-(N,N-dimethylamino)-2-propoxy)hafnium, $Hf(dmap)_4$

ABSTRACT

Atomic layer deposition (ALD) of HfO_2 thin films was studied using a novel homoleptic hafnium ALD precursor: tetrakis(1-(*N*,*N*-dimethylamino)-2-propoxy)hafnium [$Hf(dmap)_4$]. This precursor is a liquid at room temperature and has been shown by differential scanning calorimetry (DSC) analysis to be stable at temperatures as high as 371 °C. Compared with the conventional Hf precursor tetrakis(ethylmethylamido)hafnium(IV) (TEMAH), $Hf(dmap)_4$ exhibits a substantially greater decomposition temperature because of its alkoxide structure. $Hf(dmap)_4$ is a volatile compound that shows a very clean thermogravimetry curve without decomposition or residue formation at 10 Torr. We carried out ALD of HfO_2 using $Hf(dmap)_4$ with O_3 or H_2O as an oxidant. As the wafer temperature was increased from 250 to 400 °C, the film growth rate slightly increased from 0.35 Å/cycle to 0.55 Å/cycle. Therefore, $Hf(dmap)_4$ can be used for ALD at higher deposition temperatures than TEMAH. However, the film growth rate was lowered by the sterically hindered ligand structure of the precursor. We evaluated the saturation behavior of the growth rate in experiments where the $Hf(dmap)_4$ supply time was varied from 5 to 30 s. As a result, a constant film growth rate was observed because of ALD saturation when the precursor supply time was 10 s or longer in the temperature range 350–400 °C. This result indicates that $Hf(dmap)_4$ was not decomposed and behaved as an ALD precursor at 400 °C. We concluded that $Hf(dmap)_4$ is a promising precursor for high-temperature ALD.

INTRODUCTION

Hafnium(IV) oxide (HfO_2) is well known as an attractive compound for use in semiconductor devices because of its high dielectric constant (~25), wide bandgap energy (~5.7 eV), high refractive index, and good chemical stability. [1-3] It has been used in various industrial applications, including as a gate dielectric material in CMOS devices and a capacitor dielectric material in DRAM devices. [4] In addition, HfO_2 is attracting attention as a nonvolatile memory material for ferroelectric random-access memory (FeRAM) and resistive random-access memory (ReRAM). [5-7] In general, HfO_2 films are deposited by physical vapor deposition (PVD) or chemical vapor deposition (CVD). [8-10] PVD and CVD exhibit high film growth rates, enabling high productivity. However, step coverage with PVD and CVD is insufficient in principle, which makes the deposition HfO_2 films on nanosized three-dimensional structures difficult. Hence, atomic layer deposition (ALD) processes have been used to deposit HfO_2 films that exhibit good coverage and high purity and are free of pinholes. [11, 12] To obtain high-quality HfO_2 films, high-temperature processing is important to control the crystal phase of HfO_2. Therefore, the ALD of HfO_2 requires a precursor with a wide deposition temperature range.

Numerous precursors have been developed for ALD of HfO_2, including halides, alkylamides, alkoxides, and β-diketonates. As an example of a halide-type precursor, hafnium(IV) chloride ($HfCl_4$) is widely used in industrial applications because of its high thermal stability. However, it has chlorine atoms in its structure and therefore generates corrosive byproducts and contaminants in the resultant HfO_2 film. In addition, it is a solid precursor that exhibits low volatility and is therefore difficult to use in ALD. [13] Amide-type precursors such as tetrakis(dimethylamido)hafnium(IV) (TDMAH) and tetrakis(ethylmethylamido)hafnium(IV) (TEMAH) have shown good ALD behavior at temperatures near 250 °C. However, they exhibit low thermal stability and are therefore difficult to use at temperatures greater than 300 °C because of thermal decomposition. [14, 15] Cyclopentadienyl (Cp) precursors tend to exhibit ALD behavior at high temperatures, and numerous Cp-containing precursors have been reported. Dimethylbis(cyclopentadienyl)hafnium(IV) (Cp_2HfMe_2) shows self-limiting ALD growth with a growth rate of 0.42 Å/cycle at 350 °C; however, it is a solid. [16, 17] Niinistö et al. studied four novel cyclopentadienyl precursors—$(CpMe)_2HfMe_2$, $Cp_2Hf(OMe)_2$, $(CpMe)_2Hf(OMe)Me$, and $(CpMe)_2Hf(OMe)_2$—and found that $(CpMe)_2Hf(OMe)Me$ is a liquid precursor. The growth rate using $(CpMe)_2Hf(OMe)Me$ was ~0.5 Å/cycle at substrate temperatures from 350 to 500 °C. [18] Cyclopentadienyl-alkylamido precursors cyclopentadienyl tris(dimethylamino) hafnium ($CpHf(NMe_2)_3$) and methylcyclopentadienyl tris(dimethylamino) hafnium ($(CpMe)Hf(NMe_2)_3$) have also been reported. These precursors show higher growth rates (~0.75 Å/cycle at 250–350 °C) compared with $(CpMe)_2Hf(OMe)Me$. [19] A novel cyclopentadienyl-alkylamido precursor having a crosslinked structure between Cp and the alkylamine ligand has recently been reported. (η5:η1- $Cp(CH_2)_2NMe)Hf(NEtMe)_2$ (MAP-Hf01, Mecaro Co. Ltd.) shows greater thermal stability than $CpHf(NMe_2)_3$ and a growth rate of ~0.65 Å/cycle from 200 to 400 °C. [20] However, the

manufacturing steps for chemically synthesizing and purifying cyclopentadienyl precursors having such a heteroleptic structure are complicated. Thus, heteroleptic precursor manufacturing costs have been gradually rising compared with those of homoleptic precursors. In addition, the ligands in heteroleptic precursors undergo thermal decomposition or ligand redistribution reactions upon long time heating in the precursor container for precursor vapor supply into the ALD chamber, to generate the eliminated ligands and the reaction by-products. [21] It is thus plausible that these compound afford mixtures of heteroleptic Hf(IV) precursors by ligand redistribution reactions. Given these facts, we consider that heteroleptic precursor is not always the best structure. Therefore, a new hafnium precursor that exhibits high thermal stability, a low melting point, and a one kind of ligand in the molecule is necessary.

Several alkoxide precursors have been investigated as homoleptic-structured ALD precursors. HfO_2 films having good electrical properties were obtained by atomic layer controlled chemical vapor deposition (ALCVD) using hafnium(IV) *tert*-butoxide ($Hf(OtBu)_4$). [21] However, $Hf(OtBu)_4$ contains an unsaturated four-coordinate metal center and the *tert*-butoxide ligand is easily decomposed by trace moisture under inert gas. [22] Therefore, an alkoxide precursor having an unsaturated four-coordinate metal center is difficult to handle and use in ALD processes. In efforts to attain more stable complexes, researchers found that the bidentate donor-functionalized alkoxide ligand 1-methoxy-2-methyl-2-propanolate ($OCMe_2CH_2OMe$, mmp) increases the coordination number of highly positively charged central metal atoms and inhibits oligomerization in metal alkoxides; $Hf(mmp)_4$ produced monoclinic-phase HfO_2 films by ALD in the temperature range 275–425 °C, although thermal decomposition did not lead to perfect saturation. [23]

In the present study, to achieve high temperature ALD greater than 300 °C using Cl-free structure, we focused on an aminoalkoxide structure combined with both an alkoxide and amine as a novel liquid hafnium precursor. We have previously synthesized numerous Hf aminoalkoxide compounds and identified good candidates for use as ALD precursors. [24] In this paper, we report an example of a Hf aminoalkoxide precursor, tetrakis(1-(*N*,*N*-dimethylamino)-2-propoxy)hafnium [$Hf(dmap)_4$] (Table 1).

Table 1 Composition of ALD precursors for hafnium oxide film.

Name	$HfCl_4$	TEMAH	$CpHf(NMe_2)_3$	$Hf(mmp)_4$	$Hf(dmap)_4$
Reference	13	15	19	23	This work
Structure		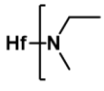	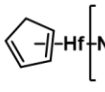	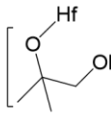	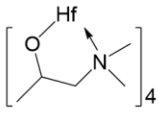
State	Solid	✓ Liquid	✓ Liquid	✓ Liquid	✓ Liquid
Contamination	Cl	✓ None	✓ None	✓ None	✓ None
Ligand	✓ Homoleptic	✓ Homoleptic	Heteroleptic	✓ Homoleptic	✓ Homoleptic
Temperature	✓ 250-500 ℃	<300 ℃	✓ 200-350 ℃	✓ 275–425 ℃	✓ 300-400 ℃
Saturation	✓ Good	✓ Good	✓ Good	Poor	✓ Good

EXPERIMENTAL

Volatility and thermal stability testing

Thermogravimetric analysis (TGA) of $Hf(dmap)_4$ was carried out at 10 Torr in an Ar-filled glovebox using a Rigaku ThermoPlus2 TG8120. The thermal decomposition temperature was measured using sealed pans by differential scanning calorimetry (DSC) with a Bruker AXS DSC 3100.

ALD testing of $Hf(dmap)_4$ precursor with oxidants

HfO_2 films were deposited using a cross-flow ALD reactor (Arradiance GEMStar XT) with water or O_3 as a co-reactant. Prior to deposition, Si(100) substrates were cut into 25 mm × 25 mm squares and cleaned with 0.5% hydrofluoric acid (HF) solution for 1 min to remove the native oxide layer. The cleaned wafer was then dried under N_2 gas and immediately loaded into the ALD chamber. Before the ALD process, the wafer was heated for 30 min to stabilize its temperature. The $Hf(dmap)_4$ was provided by ADEKA Corp. [product name: ADEKA ORCERA $Hf(dmap)_4$]. The $Hf(dmap)_4$ precursor was added to a stainless canister and heated at 150 °C. The precursor supply method was vapor drawing using Ar carrier gas at 50 sccm. The chamber pressure was controlled at ~0.20 Torr by Ar process gas. The ALD cycles were performed in the following sequences. O_3 ALD: $Hf(dmap)_4$ (supply time: 5–30 s)/Ar purge (15 s)/O_3 (10 s)/Ar purge (15 s). H_2O ALD: $Hf(dmap)_4$ (supply time: 5–30 s)/Ar purge (15 s)/H_2O (0.1 s)/Ar purge (45 s).

Characterization of deposited HfO_2 films

Hafnium deposition was measured by X-ray fluorescence (XRF) with a Rigaku ZSX Primus IVi. The stoichiometry and elemental bonding states in the films were studied by X-ray photoelectron spectroscopy (XPS) using a Thermo Fisher Scientific K-Alpha. The film thickness and the morphology were evaluated by field-emission scanning electron microscopy (FE-SEM) and atomic force microscopy (AFM), respectively, which were conducted with a Hitachi High-Tech S-4800 and a Bruker Multimode 8, respectively. The crystallinity was characterized by X-ray diffraction (XRD)

using a Rigaku Ultima IV.

Electric characterization of HfO_2 films

The electric properties of the HfO_2 films were evaluated using metal–insulator–semiconductor (MIS) structures of Pt/HfO_2/*p*-Si. The thicknesses of the Pt electrode and *p*-Si substrate were 100 nm and 0.5 mm, respectively. Capacitance–voltage (*C*–*V*) curves for the MIS structure were measured using a precision LCR meter (Agilent, 4980A). The current–voltage (*I*–*V*) curves were also evaluated (Keithley, Sourcemeter 2450). HfO_2 films were annealed in vacuum at 600 °C under Ar flow for 1 min using an infrared-lamp heating system (ADVANCE RIKO, RTP-6).

RESULTS AND DISCUSSION

Volatility and thermal stability of $Hf(dmap)_4$ precursor

Figure 1 shows the vapor pressure variations with temperature of the $Hf(dmap)_4$. The vapor pressure of the $Hf(dmap)_4$ reached 1.0 Torr at 153 °C, and that of the $HfCl_4$ reached 1.0 Torr at 190 °C. Thus, $Hf(dmap)_4$ exhibits greater volatility than $HfCl_4$.

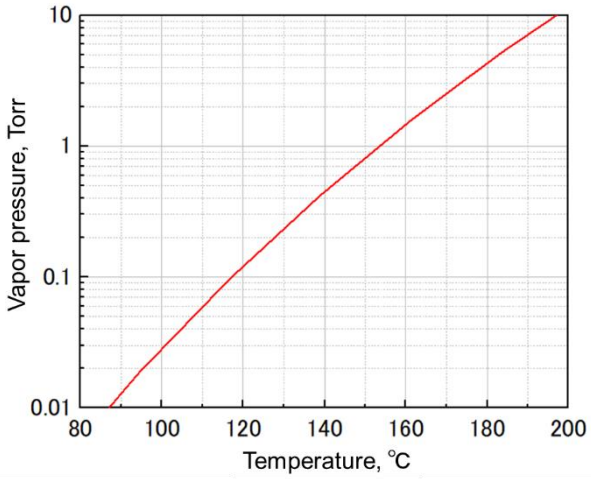

Fig. 1 Variation of the vapor pressure of $Hf(dmap)_4$ as a function of temperature.

Figure 2 (a) shows the TGA curves of $Hf(dmap)_4$ and conventional precursors, including the solid precursor $HfCl_4$ and the liquid precursor TEMAH. The TGA curve of $Hf(dmap)_4$ is clean, with a single step without decomposition or residue formation at 10 Torr. The 50% volatile temperature ($TG_{1/2}$) was 172 °C. Compared with the $HfCl_4$, the $Hf(dmap)_4$ exhibited greater volatility. The $TG_{1/2}$ of $HfCl_4$ was 184 °C, and that of TEMAH was 100 °C, indicating that it is more volatile than $Hf(dmap)_4$.

Figure 2 (b) shows the DSC thermograms of $Hf(dmap)_4$ and TEMAH. $Hf(dmap)_4$ is a liquid

precursor at room temperature; thus, no peaks are observed from room temperature to the thermal decomposition temperature. A thermal decomposition peak was observed at temperatures greater than 371.2 °C in the thermogram of $Hf(dmap)_4$. However, TEMAH's thermal decomposition peak was confirmed to appear at 280.7 °C or higher. These results indicate that $Hf(dmap)_4$ exhibits greater thermal stability than TEMAH; thus, $Hf(dmap)_4$ can be used at temperatures greater than 300 °C in the ALD process. TEMAH is difficult to use at temperatures greater than 300 °C because of its tendency to thermally decompose. [14]

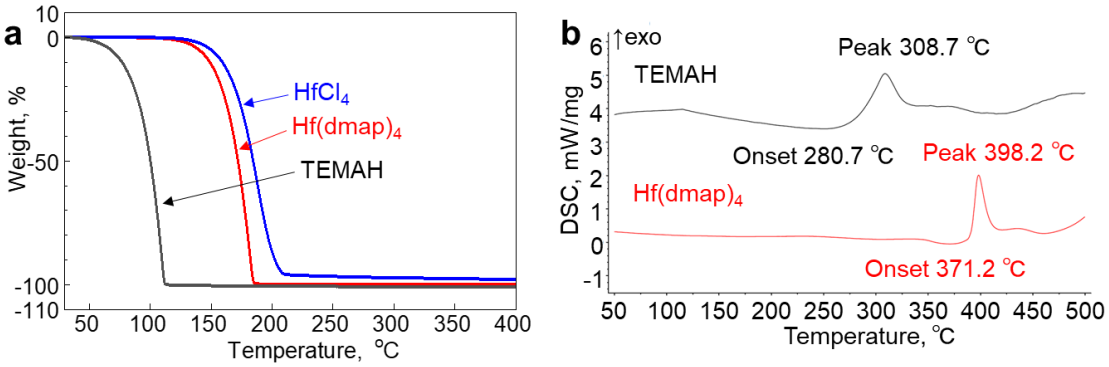

Fig. 2 (a) TGA curve of $Hf(damp)_4$ and conventional precursors TEMAH and $HfCl_4$ at 10 Torr. (b) DSC thermograms of $Hf(dmap)_4$ and TEMAH.

ALD testing of the $Hf(dmap)_4$ precursor

An evaluation of the optimal dosing time was carried out to study its effect on the growth rate using $Hf(dmap)_4$ with O_3 and water as co-reactants. The $Hf(dmap)_4$ dosing time was varied at 375 °C. Figure 3 (a) shows the thickness per cycle as a function of the $Hf(dmap)_4$ dose. The film growth rate was converted from Hf intensity of XRF. The film growth rate increased as the $Hf(dmap)_4$ dosing time was increased from 5 to 10 s. The $Hf(dmap)_4$ growth rate saturated when the Hf precursor dosing time was longer than 10 s. The Hf precursor half-reaction reached a self-limited state. The saturated growth rate was 0.46±0.5 Å/cycle (O_3) and 0.37±0.3 Å/cycle (H_2O) at 375 °C.

The O_3 dosing time was optimized. Figure 3 (b) shows a constant growth rate was observed when the dosing time was 10 s or longer. Small variations in the growth rate were confirmed at shorter dosing times because of incomplete oxidation of the metal precursor. Because carbon contamination originating from the ligand was a concern in this range of short dosing times, a dosing time of at least 10 s was considered necessary.

The H_2O dosing time was also optimized. Figure 3 (c) shows a constant growth rate was observed when the dosing time was 0.1 s or longer. The $Hf(dmap)_4$ growth rate saturated when the H_2O dosing time was longer than 0.1 s.

Figure 3 (d) shows the temperature dependence of the growth rate in a $Hf(dmap)_4 + O_3/H_2O$ ALD test process. When O_3 was used as a co-reactant, the film growth rate increased slightly as the deposition temperature was increased from 300 to 375 °C. When the deposition temperature was increased to 400 °C, the film growth rate increased because thermal decomposition began. To confirm the thermal decomposition temperature of $Hf(dmap)_4$ on the substrate during the ALD process, a pyrolysis test was carried out without a co-reactant. For the pyrolysis test in the ALD chamber, $Hf(dmap)_4$ vapor was supplied for 1000 s, which is the same dosing time as the ALD test condition, which was 10 s for 100 times (1000 s in total). The film growth was not observed during the pyrolysis test from 300 to 375 °C, indicating that $Hf(dmap)_4$ was not decomposed in this temperature range. At 400 °C, film growth started without a co-reactant, indicating that $Hf(dmap)_4$ decomposed on the substrate as a result of thermal energy without a co-reactant; thus, a Hf-containing oxide film was detected. When H_2O was used as a co-reactant in ALD, the film growth rate in the temperature range 300–375 °C was lower than when O_3 was used. The film growth rate also increased at 400 °C because of thermal decomposition.

Figure 3 (e) shows the film thickness as a function of the number of ALD cycles. The film thickness was measured by X-ray reflectometry (XRR) and FE-SEM. The thickness increases linearly with increasing number of ALD cycles at 375 °C. This result indicates that the film grew with a constant growth rate; that is, $Hf(dmap)_4$ exhibits excellent thickness-control characteristics. The linear dependence and saturation behavior were verified, and we therefore concluded that $Hf(dmap)_4$ exhibited ALD-type growth behavior.

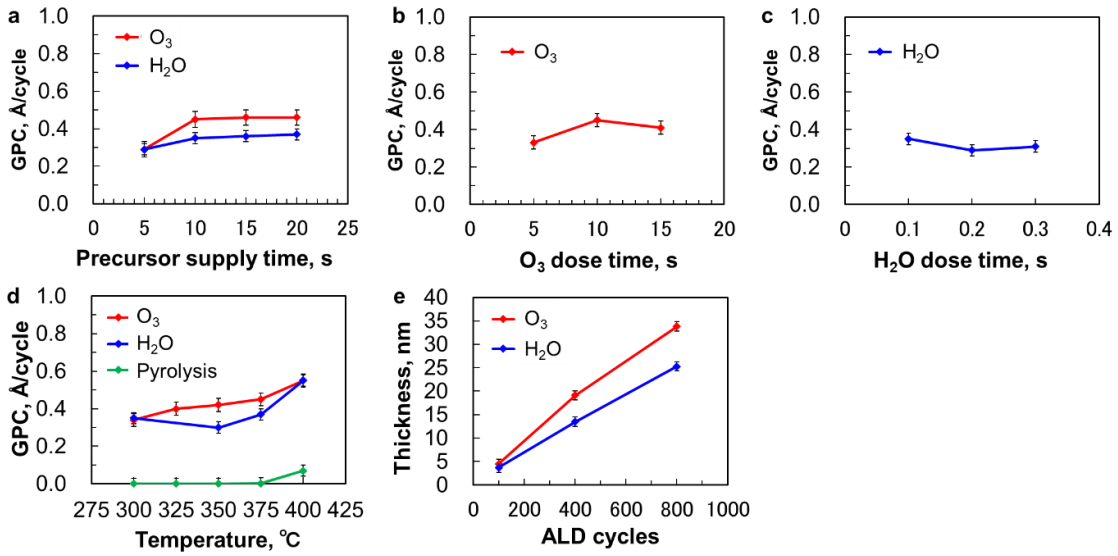

Fig. 3 (a) Growth rate as a function of the $Hf(dmap)_4$ supply time at a substrate temperature of 375 °C when O_3 and H_2O were used as co-reactants. (b) Growth rate as a function of the O_3 dose time at a substrate temperature of 375 °C. (c) Growth rate as a function of the H_2O dose time at a substrate

temperature of 375 °C. (d) Temperature dependence of the growth rate of $Hf(dmap)_4$ + O_3 or H_2O during ALD and the growth rate of $Hf(dmap)_4$ in a pyrolysis test. (e) Film thickness as a function of the number of ALD cycles when O_3 and H_2O were used as co-reactants at 375 °C.

Characterization of HfO_2 films deposited by $Hf(dmap)_4$ precursor with O_3 and water co-reactants

The film concentration and impurities in the film were measured by XPS analysis. Table 2 shows the composition of the as-deposited HfO_2 films obtained at each deposition temperature (350, 375, and 400 °C) when O_3 or H_2O was used as a co-reactant. The corresponded XPS depth profiles and high-resolution spectra are displayed in Figure 4. The film deposited at 350 °C using O_3 as a co-reactant contained 2.4±0.7 at% of carbide as an impurity. This carbide contamination was reduced with increasing deposition temperature. At 400 °C, impurities were not detected in the film. The O/Hf ratio was 1.69, which is lower than the stoichiometric O/Hf ratio. The Hf 4f5/2 and Hf 4f7/2 peaks of HfO_2 corresponded to 19.4 eV and 17.7 eV. The noticeable and broadened shoulders appeared at the lower binding energy side of Hf 4f7/2. The tailing is probably a result of oxygen deficiency and thus this indicates that HfO_2 suboxides were also generated in the film. This lower O/Hf ratio is attributed to $Hf(dmap)_4$ having a bulky ligand, which likely reduced its reactivity. The lower O/Hf ratio can be improved by process optimization such as a higher O_3 partial pressure during the ALD process and multi feeding and purge sequence to eliminate bulky ligands. The film deposited at 350 °C using H_2O as a co-reactant also contained 9.2±0.7 at% carbon and carbide, 1.9±0.2 at% nitrogen, and 1.3±0.3 at% silicon as impurities. H_2O is less reactive than O_3; it therefore led to greater contamination compared with that in the O_3 ALD films. Using a higher deposition temperature can reduce the amount of impurities. However, 3.7±0.5 at% carbide contamination remained even when the deposition temperature was increased to 400 °C. The O/Hf ratio was 1.66, indicating that the H_2O content was insufficient. This situation can likely be improved by extending the H_2O dosing time. For comparison, TEMAH and $HfCl_4$ ALD were conducted using H_2O as a co-reactant. At 300 °C, TEMAH generated a HfO_2 film that included 3.4±0.4 at% carbon contamination because of thermal decomposition of TEMAH. When $HfCl_4$ was used, 1.2±0.5 at% carbon, 6.0±0.9 at% silicon, and <0.2 at% chlorine impurities were detected in the film deposited at 380 °C. Therefore, $Hf(dmap)_4$ + O_3 ALD can be used to deposit high-purity HfO_2 films at 400 °C.

Table 2 Composition of as-deposited hafnium oxide films grown on silicon using a different co-reactant, as characterized by XPS.

Precursor	Reactant	T_{growth}, ºC	Hf, at%	O, at%	C, at%	N, at%	Si, at%	Cl, at%	O/Hf ratio
$Hf(dmap)_4$	O_3	350	35.4±0.5	61.7±0.5	2.4±0.7	<0.2	<0.4	<0.1	1.74

$Hf(dmap)_4$	O_3	375	37.4±0.3	60.8±0.6	<0.5	<0.5	<0.8	<0.1	1.63
$Hf(dmap)_4$	O_3	400	37.2±0.2	62.8±0.4	<0.4	<0.1	<0.4	<0.1	1.69
$Hf(dmap)_4$	H_2O	350	33.1±0.4	54.6±1.1	9.2±0.7	1.9±0.2	1.3±0.3	<0.1	1.65
$Hf(dmap)_4$	H_2O	375	36.3±0.6	59.6±1.0	4.1±0.4	<0.2	<0.1	<0.1	1.64
$Hf(dmap)_4$	H_2O	400	36.3±0.2	60.1±0.4	3.7±0.5	<0.1	<0.1	<0.1	1.66
TEMAH	H_2O	300	33.9±0.2	62.6±0.3	3.4±0.4	<0.3	<0.2	<0.1	1.85
$HfCl_4$	H_2O	380	32.2±0.4	60.4±0.8	1.2±0.5	<0.1	6.0±0.9	<0.2	1.88

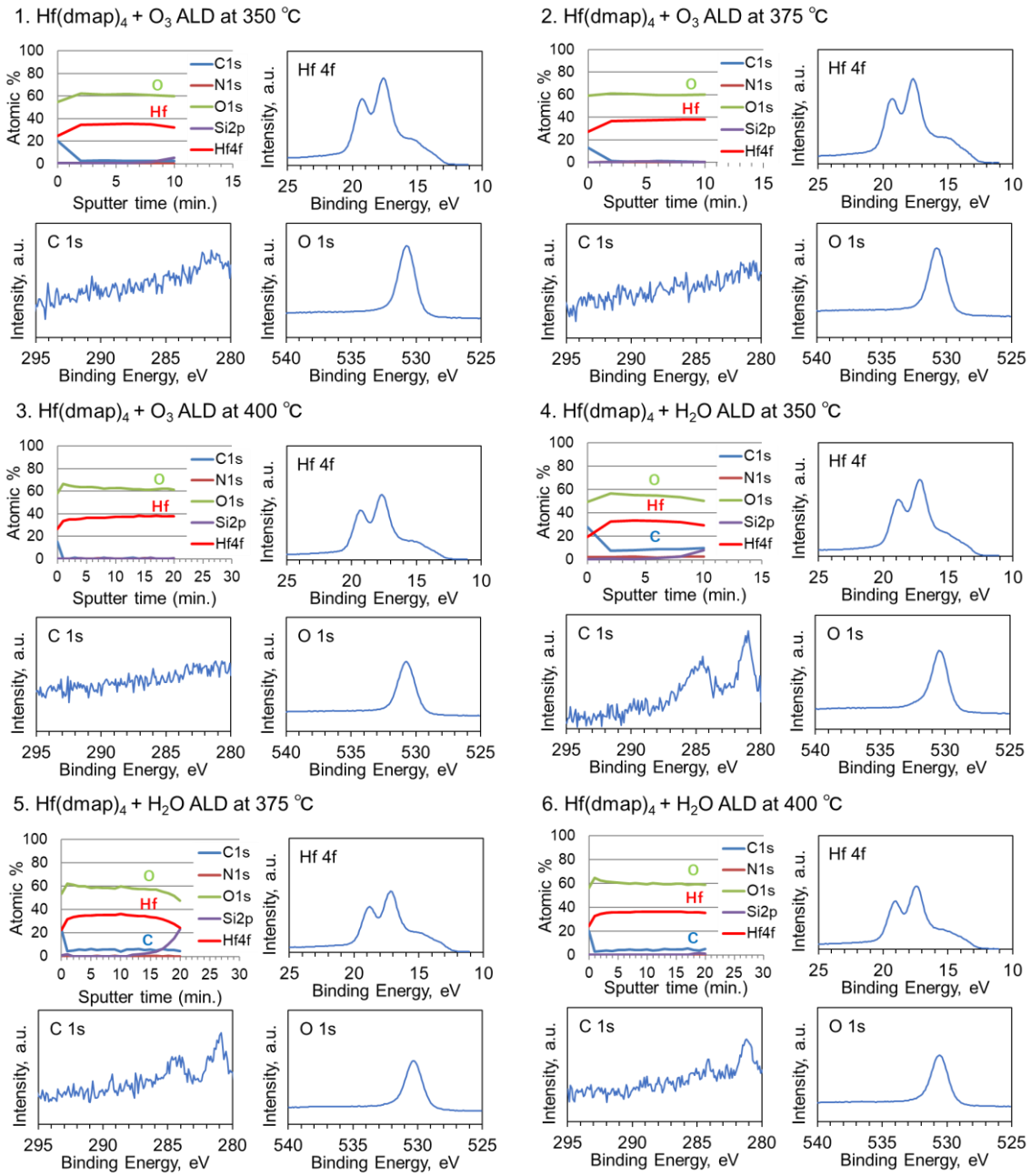

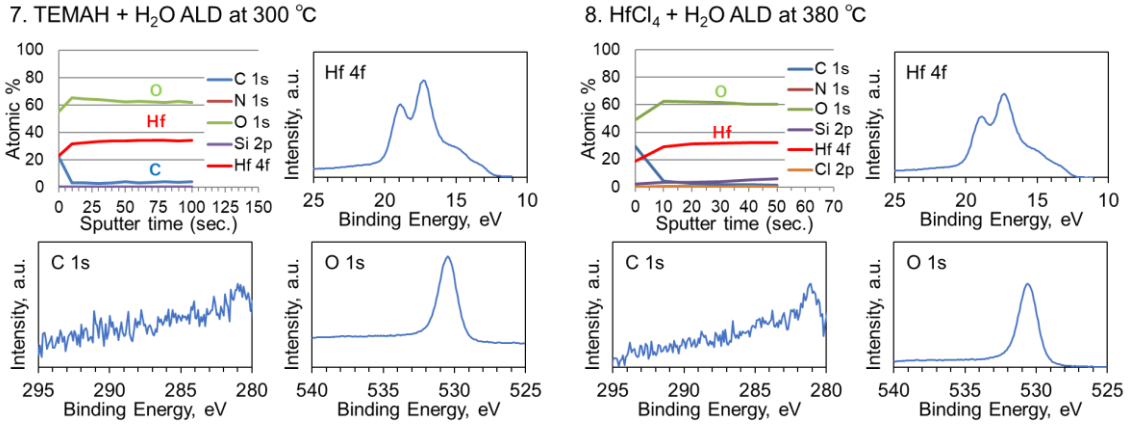

Fig. 4 XPS spectra of HfO_2 films made by $Hf(dmap)_4$ + O_3 or H_2O ALD and conventional precursors TEMAH and HCl_4 + H_2O ALD corresponding to Table 2.

Figure 5 shows XRD patterns of HfO_2 films with a thickness of 20–30 nm, deposited from $Hf(dmap)_4$ with O_3 (a) or H_2O (b) as a co-reactant at temperatures ranging from 350 to 400 °C. Crystalline peaks were not observed in the patterns of the films deposited at 350 °C with either O_3 or H_2O; thus, the films were amorphous. Impurities likely influence the crystallinity. Crystalline peaks were observed in the patterns of films deposited at temperatures greater than 375 °C. The intensity of these reflections increased with increasing deposition temperature. The diffraction peaks matched those of monoclinic HfO_2 (JCPDS card No. 34-104). At deposition temperatures greater than 375 °C, crystalline HfO_2 films can be deposited using $Hf(dmap)_4$ and either co-reactant, without post-annealing.

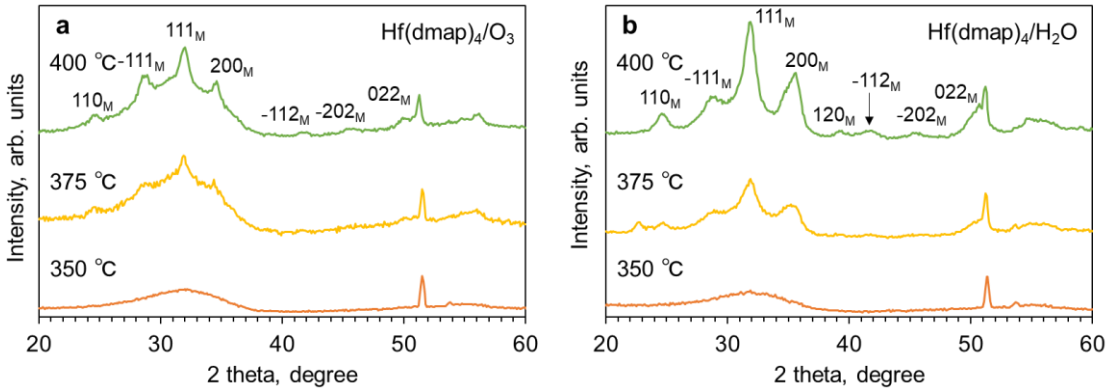

Fig. 5 XRD patterns of HfO_2 films with thicknesses of 20–30 nm, deposited onto silicon using $Hf(dmap)_4$ + O_3 (a) or H_2O (b) as a co-reactant. The HfO_2 films' thicknesses were 18.2 (a, 350 °C), 31.4 (a, 375 °C), 33.9 (a, 400 °C), 19.9 (b, 350 °C), 26.8 (b, 375 °C), and 33.8 nm (b, 400 °C).

Table 3 shows the rms roughness values and HfO_2 film thicknesses obtained by AFM and

FE-SEM measurements. The corresponded AFM and FE-SEM images are displayed in Figure 6 and 7. For the films deposited at 350 °C, the O_3 and H_2O films exhibited low rms roughness values of 0.38±0.03 nm (O_3) and 0.30±0.03 nm (H_2O). An amorphous HfO_2 film was deposited at 350 °C; thus, a very smooth HfO_2 film was grown. At deposition temperatures greater than 375 °C, the rms values increased to 1.37±0.07 nm (O_3, 375 °C), 1.59±0.08 nm (O_3, 400 °C), 0.90±0.05 nm (H_2O, 375 °C), and 1.11±0.06 nm (H_2O, 400 °C) because of crystallization of the HfO_2 films. To reduce film contamination, higher deposition temperatures are necessary. However, a deposition temperature greater than 375 °C led to a HfO_2 film having a rough surface because of crystallization. We therefore investigated thinner film surfaces to restrain grain growth. HfO_2 films with a thickness of ~10 nm were deposited at each deposition temperature of 350, 375, and 400 °C using O_3 as a co-reactant. The rms values were 0.20±0.03, 0.17±0.03, and 0.19±0.03 nm, respectively. These films exhibited very smooth surfaces, and their XRD patterns did not show diffraction peaks. Therefore, these HfO_2 films were amorphous.

Table 3 Rms roughness values and thicknesses of HfO_2 films.

Co-reactant	T_{growth}, °C	Thickness of HfO_2, nm	rms, nm
O_3	350	18.2±1.2	0.38±0.03
O_3	375	31.4±0.4	1.37±0.07
O_3	400	33.9±1.7	1.59±0.08
O_3	350	10.5±0.5	0.20±0.03
O_3	375	10.4±0.5	0.17±0.03
O_3	400	10.6±0.5	0.19±0.03
H_2O	350	19.9±1.0	0.30±0.03
H_2O	375	26.8±1.3	0.90±0.05
H_2O	400	33.8±1.7	1.11±0.06

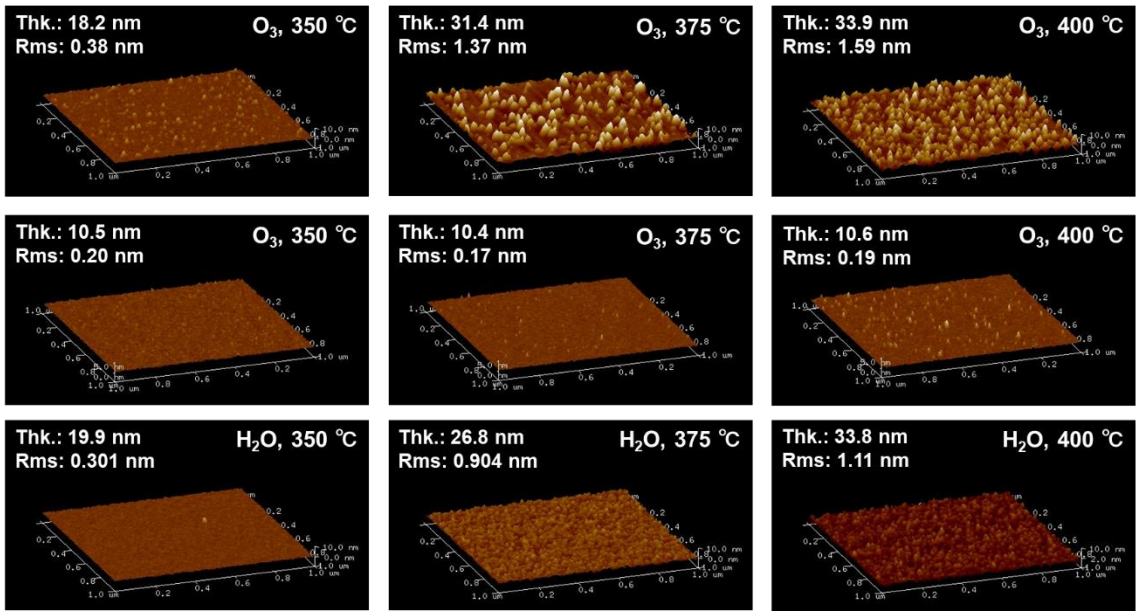

Fig. 6 AFM images of HfO_2 films made by $Hf(dmap)_4$ + O_3 or H_2O ALD.

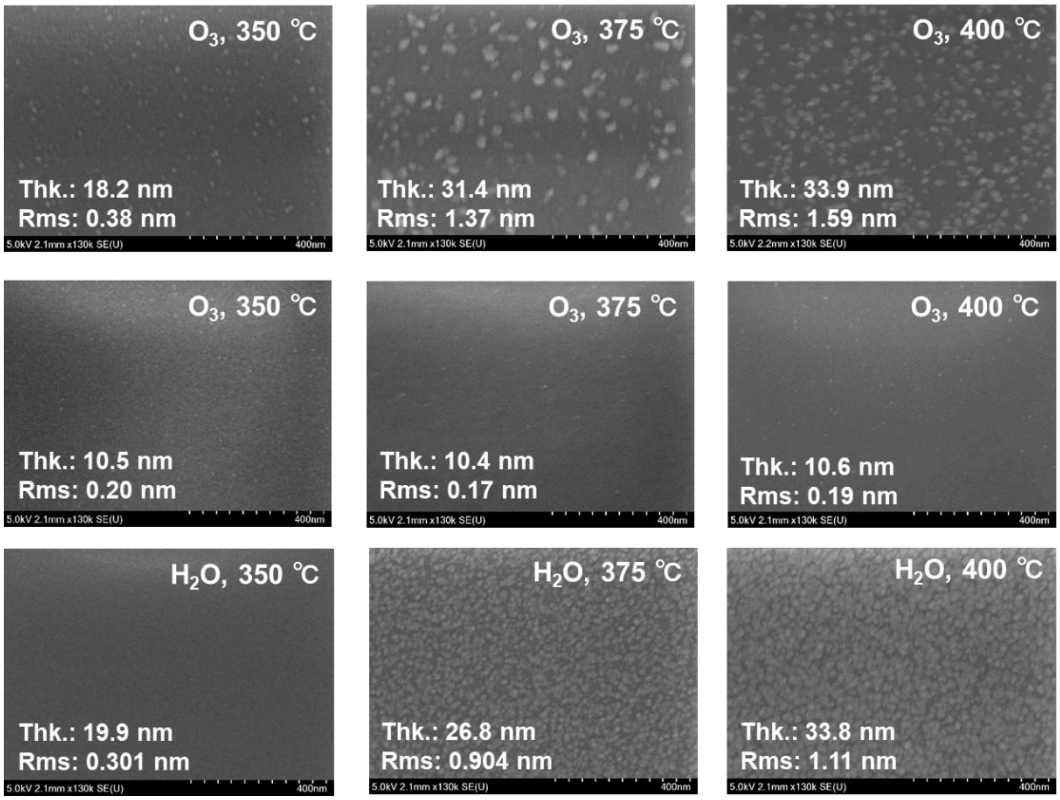

Fig. 7 FE-SEM images of HfO_2 films made by $Hf(dmap)_4$ + O_3 or H_2O ALD.

Electric characterization of HfO_2 films deposited by $Hf(dmap)_4$ precursor with O_3

Figure 8 (a) shows *C–V* curves for the Pt/HfO_2/*p*-Si MIS capacitors before and after the capacitors were annealed at 600 °C for 1 min. The area of the top Pt electrode was 0.0154 mm^2, and the thickness and deposition temperature for the HfO_2 layer were 10.5 nm and 350 °C, respectively. When a negative bias was applied, the capacitance values of both of the MIS capacitors were 0.26 nF. The results indicate that the dielectric constant of the HfO_2 layers was ~19.4, which is similar to the previously reported value ~21.4 (TEMAH). [25] However, when a positive bias was applied to the MIS capacitors, the capacitance values substantially decreased because of the formation of a depletion layer in the *p*-Si. A counterclockwise hysteresis was observed in the *C–V* curves, likely because holes were trapped at the interface between the HfO_2 and the *p*-Si, resulting in a shift of the flatband voltage due to the screening of the electric field. The hysteresis of the MIS capacitor was narrowed when the device was annealed at 600 °C for 1 min.

Figure 8 (b) shows the leakage current density versus electric field curves for the Pt/HfO_2/*p*-Si MIS capacitor. The leakage current density at 1 MV/cm and breakdown electric field were approximately 1.7×10^{-7} A/cm^2 and 6.4 MV/cm, respectively. These values are similar to or better than those previously reported for MIS capacitors fabricated using a HfO_2 layer prepared from solid or heteroleptic ALD precursors. [13-15, 20, 23, 25] The leakage current density of the MIS capacitor at 1 MV/cm was 1.2×10^{-7} A/cm^2 and did not substantially change upon annealing at 600 °C for 1 min. Thus, these results indicate that a HfO_2 layer with high electronic performance could be attained even when a liquid homoleptic ALD precursor [$Hf(dmap)_4$] was used.

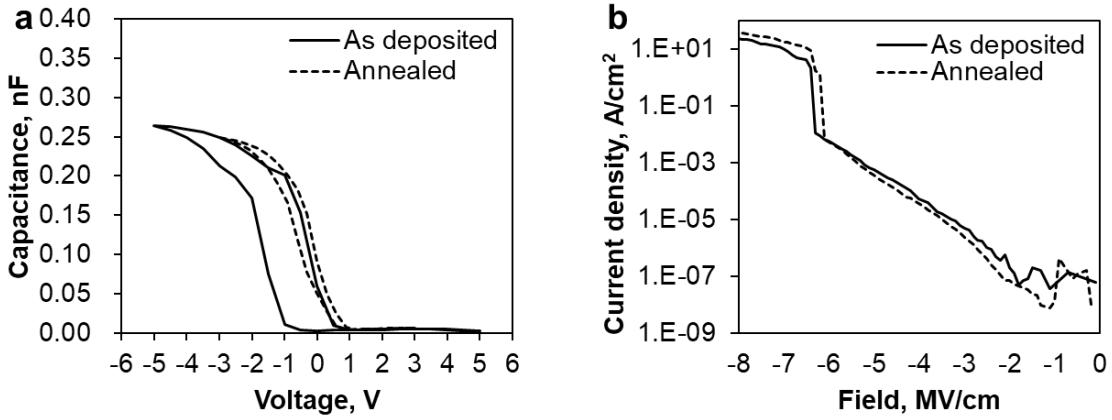

Fig. 8 Electric characterization of as deposited (solid line) and annealed (dashed line) HfO_2 films (a) *C–V* curves of the Pt/HfO_2/*p*-Si MIS capacitor at a frequency of 100 kHz. The HfO_2 film deposition temperature was at 350 °C. The MIS structure was Pt/HfO_2 (10.5 nm)/*p*-type Si/Pt. The post-annealing was conducted at 600 °C for 1 min. (b) *I–V* curves of the Pt/HfO_2/*p*-Si MIS capacitors before and after annealing at 600 °C for 1 min. The thickness and deposition temperature of the HfO_2 layer were 10 nm and 350 °C, respectively.

SUMMARY AND CONCLUSIONS

We evaluated a newly developed hafnium precursor, $Hf(dmap)_4$, which is a liquid at room temperature and exhibits thermal stability to temperatures as high as 400 °C. These properties are a great advantage of $Hf(dmap)_4$ compared with amide-type precursors such as TDMAH and TEMAH. $Hf(dmap)_4$ exhibits greater volatility (1.0 Torr at 153 °C) than $HfCl_4$. Even though $Hf(dmap)_4$ exhibits high thermal stability, there is no chlorine atom in the molecule. Thus, unlike $HfCl_4$, $Hf(dmap)_4$ does not generate corrosive byproducts or chlorine contaminants in the resultant film. $Hf(dmap)_4$ has a one type of ligand in the molecule. Thus, a reduction of manufacturing costs is expected compared with those associated with heteroleptic-structured precursors because additional chemical synthesis manufacturing steps are usually necessary to make heteroleptic-structured compounds.

We demonstrated ALD of HfO_2 films using $Hf(dmap)_4$ with O_3 or H_2O as a co-reactant. The ALD window was estimated to range from 300 to 375 °C. Thermal decomposition of $Hf(dmap)_4$ was observed at 400 °C on Si substrates by pyrolysis tests. The film growth rate was at 0.46 Å/cycle (O_3) and 0.37 Å/cycle (H_2O) at 375 °C. XPS analysis showed that a high-purity HfO_2 film was deposited at temperatures greater than 375 °C when O_3 was used as a co-reactant. The H_2O co-reactant resulted in a small amount of carbon contamination in the film. The HfO_2 film with a thickness of ~30 nm was crystalized at deposition temperature greater than 375 °C without a post-annealing process. A thinner HfO_2 film with a thickness of ~10 nm thickness exhibited a very smooth surface irrespective of the deposition temperature. A HfO_2 layer with high electronic performance could be deposited at 350 °C using O_3 co-reactant even when a liquid ALD precursor [$Hf(dmap)_4$] was used. Thus, these data indicate that there is still room for improvement of the electronic performance deposited by $Hf(dmap)_4$ greater than 375 °C. We deduce that these film properties were achieved by high temperature ALD realized by excellent thermal stability of $Hf(dmap)_4$. Therefore, we conclude that $Hf(dmap)_4$ is an excellent candidate as a HfO_2 ALD precursor for use in the temperature range 300–400 °C.

ACKNOWLEDGMENTS

We are grateful to ADEKA Corporation for providing the $Hf(dmap)_4$ precursor and its vapor pressure, TGA, and DSC data.

This work was partly supported by “Crossover Alliance to Create the Future with People, Intelligence and Materials” and Advanced Research Infrastructure for Materials and Nanotechnology (ARIM) Japan from the Ministry of Education, Culture, Sports, Science and Technology (MEXT).

REFERENCES

(1) Robertson, J. High dielectric constant gate oxides for metal oxide Si transistors. *Reports on Progress in Physics* **2006**, *69* (2), 327-396. DOI: 10.1088/0034-4885/69/2/r02.

(2) Wong, H.; Iwai, H. On the scaling issues and high- κ replacement of ultrathin gate dielectrics for nanoscale MOS transistors. *Microelectronic Engineering* **2006**, *83* (10), 1867-1904. DOI: 10.1016/j.mee.2006.01.271.
(3) Choi, J. H.; Mao, Y.; Chang, J. P. Development of hafnium based high-k materials—A review. *Materials Science and Engineering: R: Reports* **2011**, *72* (6), 97-136. DOI: 10.1016/j.mser.2010.12.001.
(4) Robertson, J.; Wallace, R. M. High-K materials and metal gates for CMOS applications. *Materials Science and Engineering: R: Reports* **2015**, *88*, 1-41. DOI: 10.1016/j.mser.2014.11.001.
(5) Müller, J.; Schröder, U.; Böscke, T. S.; Müller, I.; Böttger, U.; Wilde, L.; Sundqvist, J.; Lemberger, M.; Kücher, P.; Mikolajick, T.; et al. Ferroelectricity in yttrium-doped hafnium oxide. *Journal of Applied Physics* **2011**, *110* (11). DOI: 10.1063/1.3667205.
(6) Park, M. H.; Lee, Y. H.; Mikolajick, T.; Schroeder, U.; Hwang, C. S. Review and perspective on ferroelectric HfO2-based thin films for memory applications. *MRS Communications* **2018**, *8* (3), 795-808. DOI: 10.1557/mrc.2018.175.
(7) Chen, Y. ReRAM: History, Status, and Future. *IEEE Transactions on Electron Devices* **2020**, *67* (4), 1420-1433. DOI: 10.1109/ted.2019.2961505.
(8) He, G.; Liu, M.; Zhu, L. Q.; Chang, M.; Fang, Q.; Zhang, L. D. Effect of postdeposition annealing on the thermal stability and structural characteristics of sputtered HfO2 films on Si (100). *Surface Science* **2005**, *576* (1-3), 67-75. DOI: 10.1016/j.susc.2004.11.042.
(9) Van Elshocht, S.; Baklanov, M.; Brijs, B.; Carter, R.; Caymax, M.; Carbonell, L.; Claes, M.; Conard, T.; Cosnier, V.; Daté, L.; et al. Bulk Properties of MOCVD-Deposited HfO[sub 2] Layers for High k Dielectric Applications. *Journal of The Electrochemical Society* **2004**, *151* (10). DOI: 10.1149/1.1784822.
(10) Cheynet, M. C.; Pokrant, S.; Tichelaar, F. D.; Rouvière, J.-L. Crystal structure and band gap determination of HfO2 thin films. *Journal of Applied Physics* **2007**, *101* (5). DOI: 10.1063/1.2697551.
(11) Hausmann, D. M.; Kim, E.; Becker, J.; Gordon, R. G. Atomic layer deposition of hafnium and zirconium oxides using metal amide precursors. *Chemistry of Materials* **2002**, *14* (10), 4350-4358. DOI: 10.1021/cm020357x.
(12) Gusev, E. P.; Cabral, C.; Copel, M.; D'Emic, C.; Gribelyuk, M. Ultrathin HfO2 films grown on silicon by atomic layer deposition for advanced gate dielectrics applications. *Microelectronic Engineering* **2003**, *69* (2-4), 145-151. DOI: 10.1016/s0167-9317(03)00291-0.
(13) Park, H. B.; Cho, M.; Park, J.; Lee, S. W.; Hwang, C. S.; Kim, J.-P.; Lee, J.-H.; Lee, N.-I.; Kang, H.-K.; Lee, J.-C.; et al. Comparison of HfO2 films grown by atomic layer deposition using HfCl4 and H2O or O3 as the oxidant. *Journal of Applied Physics* **2003**, *94* (5), 3641-3647. DOI: 10.1063/1.1599980.

(14) Kukli, K.; Ritala, M.; Sajavaara, T.; Keinonen, J.; Leskelä, M. Atomic Layer Deposition of Hafnium Dioxide Films from Hafnium Tetrakis(ethylmethylamide) and Water. *Chemical Vapor Deposition* **2002**, *8* (5), 199-204. DOI: 10.1002/1521-3862(20020903)8:5<199::Aid-cvde199>3.0.Co;2-u.

(15) Kukli, K.; Pilvi, T.; Ritala, M.; Sajavaara, T.; Lu, J.; Leskelä, M. Atomic layer deposition of hafnium dioxide thin films from hafnium tetrakis(dimethylamide) and water. *Thin Solid Films* **2005**, *491* (1-2), 328-338. DOI: 10.1016/j.tsf.2005.05.050.

(16) Samuel, E.; Rausch, M. D. .pi.-Cyclopentadienyl and .pi.-indenyl compounds of titanium, zirconium, and hafnium containing .sigma.-bonded organic substituents. *Journal of the American Chemical Society* **2002**, *95* (19), 6263-6267. DOI: 10.1021/ja00800a018.

(17) Niinistö, J.; Putkonen, M.; Niinistö, L.; Stoll, S. L.; KukliAlso at: University of Tartu, K.; SajavaaraAlso at: K. U. Leuven, I. T.; Ritala, M.; Leskelä, M. Controlled growth of HfO2 thin films by atomic layer deposition from cyclopentadienyl-type precursor and water. *Journal of Materials Chemistry* **2005**, *15* (23). DOI: 10.1039/b417866c.

(18) Niinistö, J.; Putkonen, M.; Niinistö, L.; Song, F.; Williams, P.; Heys, P. N.; Odedra, R. Atomic Layer Deposition of HfO2 Thin Films Exploiting Novel Cyclopentadienyl Precursors at High Temperatures. *Chemistry of Materials* **2007**, *19* (13), 3319-3324. DOI: 10.1021/cm0626583.

(19) Niinistö, J.; Mäntymäki, M.; Kukli, K.; Costelle, L.; Puukilainen, E.; Ritala, M.; Leskelä, M. Growth and phase stabilization of HfO2 thin films by ALD using novel precursors. *Journal of Crystal Growth* **2010**, *312* (2), 245-249. DOI: 10.1016/j.jcrysgro.2009.10.028.

(20) Baek, J.-h.; Choi, W.-h.; Kim, H.; Cheon, S.; Byun, Y.; Jeon, W.; Park, J.-S. Plasma-enhanced atomic layer deposited HfO2 films using a novel heteroleptic cyclopentadienyl-based Hf precursor. *Ceramics International* **2021**, *47* (20), 29030-29035. DOI: 10.1016/j.ceramint.2021.07.065.

(21) Lin, Y. S.; Puthenkovilakam, R.; Chang, J. P. Dielectric property and thermal stability of HfO2 on silicon. *Applied Physics Letters* **2002**, *81* (11), 2041-2043. DOI: 10.1063/1.1506207.

(22) Bradley, D. C. Metal alkoxides as precursors for electronic and ceramic materials. *Chemical Reviews* **2002**, *89* (6), 1317-1322. DOI: 10.1021/cr00096a004.

(23) Kukli, K.; Ritala, M.; Leskelä, M.; Sajavaara, T.; Keinonen, J.; Jones, A. C.; Roberts, J. L. Atomic Layer Deposition of Hafnium Dioxide Films from 1-Methoxy-2-methyl-2-propanolate Complex of Hafnium. *Chemistry of Materials* **2003**, *15* (8), 1722-1727. DOI: 10.1021/cm021328p.

(24) Nishida, A.; Hatase, M.; Yoshino, T.; Ooe, Y.; Mitsui, C. METHOD FOR MANUFACTURING THIN FILM. Japan WO/2022/107769, PCT/JP2021/042094, 2022.

(25) Park, S.; Park, B.-E.; Yoon, H.; Lee, S.; Nam, T.; Cheon, T.; Kim, S.-H.; Cheon, H.; Im, S.; Seong, T.; et al. Comparative study on atomic layer deposition of HfO2via substitution of ligand structure with cyclopentadiene. *Journal of Materials Chemistry C* **2020**, *8* (4), 1344-1352. DOI: 10.1039/c9tc05778a.

Chapter 4

Atomic Layer Deposition of ZrO_2 Films Using Novel Liquid Cl-Free Zirconium Precursor Tetrakis(1-(N,N-dimethylamino)-2-propoxy)zirconium, $Zr(dmap)_4$

ABSTRACT

Atomic layer deposition (ALD) of ZrO_2 thin films were studied using a novel homoleptic zirconium ALD precursor, tetrakis(1-(*N*,*N*-dimethylamino)-2-propoxy)zirconium [$Zr(dmap)_4$]. This precursor is a liquid at room temperature and was shown by differential scanning calorimetry (DSC) analysis to exhibit high thermal stability at temperatures as high as 390 °C. $Zr(dmap)_4$ is a volatile compound and shows a clean thermogravimetry curve without decomposition or residue formation at 760 Torr. We carried out ALD of ZrO_2 films using $Zr(dmap)_4$ as a precursor and O_3 as an oxidant. The growth rate of the ZrO_2 films was studied in the temperature range 300–400 °C. The film growth rate increased from 0.18 to 0.53 Å/cycle with increasing wafer temperature. This deposition behavior is usually caused by thermal decomposition. To confirm the thermal decomposition of the precursor, the saturation behavior of the growth rate was evaluated from 350 to 400 °C. The $Zr(dmap)_4$ supply time was varied from 5 to 15 s, and a constant film growth rate as a result of ALD saturation was observed in the temperature range 350–400 °C when the precursor supply time was 10 s or longer. This result indicates that $Zr(dmap)_4$ was not decomposed and functioned as an ALD precursor at temperatures as high as 400 °C. We speculate that the increase in the film growth rate with increasing deposition temperature was likely caused by eliminated ligands. At lower deposition temperatures, eliminated ligands might have inhibited the adsorption of precursor molecules. The inhibitory effect was diminished with increasing wafer temperature because the ligands were desorbed from the substrate. We concluded that $Zr(dmap)_4$ is a promising precursor for high-temperature ALD of ZrO_2 film.

INTRODUCTION

Zirconium oxide (ZrO_2) is as an attractive compound because of its high dielectric constant (~25), wide bandgap energy (~5.8 eV), high refractive index, and good chemical stability. [1-5] It has been used in various industrial applications, including as a gate dielectric in complementary metal oxide semiconductor (CMOS) devices and as a capacitor dielectric in dynamic random access memory (DRAM) devices. [6-8] In addition, ZrO_2 is attracting attention as a ferroelectric and antiferroelectric material for nonvolatile memory, pyroelectric energy harvesting, and electrocaloric cooling technology. [9-11] In general, ZrO_2 films are deposited by physical vapor deposition (PVD) or chemical vapor deposition (CVD). [4, 12, 13] PVD and CVD are capable of high film growth rates, enabling films to be deposited with high productivity. However, the step coverage is insufficient in principle, making the deposition of thin conformal films on nanosized three-dimensional structures difficult. [14] Hence, atomic layer deposition (ALD) processes have been used to deposit ZrO_2 films that exhibit good coverage and high purity and are free of pinholes. [15, 16] Therefore, the ALD technology for ZrO_2 film deposition is critical; however, the commonly used ZrO_2 ALD precursors have some shortcomings. Zirconium chloride ($ZrCl_4$) has high thermal stability and therefore enables ZrO_2 to be deposited over wide temperature range when used as an ALD precursor. [16, 17] However, $ZrCl_4$ has chlorine atoms in its molecular structure; it therefore generates corrosive byproducts and introduces chlorine contaminants into the resultant film. In addition, it is a solid precursor that exhibits low volatility; thus, $ZrCl_4$ is difficult to use in industrial applications. Alkylamide-type precursors such as tetrakis(dimethylamido)zirconium(IV) (TDMAZ) and tetrakis(ethylmethylamido)zirconium(IV) (TEMAZ) are widely used for the ALD of ZrO_2 films because of their high volatility and high film growth rate. [18-22] However, TDMAZ and TEMAZ have low thermal stability, which makes them difficult to use at temperatures greater than 300 °C. Cyclopentadienyl (Cp)-type heteroleptic precursors tend to exhibit ALD behavior at high temperatures, and many such precursors have been reported. [23-27] However, such heteroleptic structures require additional manufacturing steps for their chemical synthesis. In addition, purification processes for mono-cyclopentadienyl precursors are complicated because of synthesis byproducts such as metallocene compounds. Consequently, the manufacturing cost of heteroleptic precursors is gradually rising compared with that of homoleptic precursors. The development of new zirconium precursors that exhibit high thermal stability, a low melting point, and a homoleptic structure is therefore needed.

We have sought novel ALD precursors that exhibit high thermal stability, a low melting point, and a homoleptic molecular structure and have found a aminoalkoxide structure that satisfies these requirements. The Hf aminoalkoxide precursor tetrakis(1-(*N*,*N*-dimethylamino)-2-propoxy)hafnium [$Hf(dmap)_4$] is a liquid at room temperature and has a ALD window corresponding to 400 °C. [28] In this paper, we describe the thermal properties, ALD behavior, and ZrO_2 film growth of conventional ALD precursors and a Zr aminoalkoxide precursor, tetrakis(1-(*N*,*N*-dimethylamino)-

2-propoxy)zirconium [$Zr(dmap)_4$] (Table 1).

Table 1 Composition of ALD precursors for zirconium oxide film.

Name	$ZrCl_4$	TEMAZ	$CpZr(NMe_2)_3$	Cp_2ZrMe_2	$Zr(dmap)_4$
Reference	16, 17	18	26	23	This work
Structure	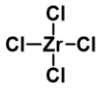	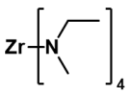	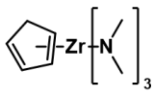	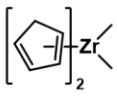	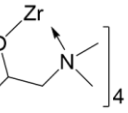
State	Solid	✓ Liquid	✓ Liquid	✓ Liquid	✓ Liquid
Halide	Cl	✓ None	✓ None	✓ None	✓ None
Ligand	✓ Homoleptic	✓ Homoleptic	Heteroleptic	Heteroleptic	✓ Homoleptic
Temperature	✓ 250-500 ℃	<300 ℃	<300 ℃	✓ <350 ℃	✓ 300-400 ℃

EXPERIMENTAL

Volatility and thermal stability testing

Thermogravimetric analysis (TGA) of $Zr(dmap)_4$ was carried out at 10 Torr in an argon glovebox using Rigaku ThermoPlus2 TG8120. The thermal decomposition temperature was measured by differential scanning calorimetry (DSC) with a Bruker AXS DSC 3100.

ALD testing of the $Zr(dmap)_4$ precursor with oxidants

ZrO_2 films were deposited in a cross-flow ALD reactor (NCD Lucida D100) using water or O_3 as a co-reactant. Prior to deposition, Si (100) substrates were cut to 25 mm × 25 mm and cleaned in 0.5% HF solution for 1 min to remove the native oxide layer. The cleaned wafer was then dried with N_2 gas and loaded into the ALD chamber immediately. Before the ALD process, the wafer was heated for 30 min to stabilize its temperature. The $Zr(dmap)_4$ precursor was synthesized by the method described in literature and provided by ADEKA [Product name: ADEKA ORCERA $Zr(dmap)_4$]. [29] The $Zr(dmap)_4$ precursor was added to a stainless steel canister and heated at 150 °C. The precursor supply method was vapor drawing using Ar carrier gas at 50 sccm. The chamber pressure was controlled at ~0.20 Torr by Ar process gas. The ALD cycles were performed in the following sequence. O_3 ALD: $Zr(dmap)_4$ (supply time: 5–15 s)/Ar purge (15 s)/O_3 (10 s)/Ar purge (15 s). H_2O ALD: $Zr(dmap)_4$ (supply time: 5–15 s)/Ar purge (15 s)/H_2O (0.1 s)/Ar purge (45 s).

Characterization of deposited ZrO_2 films

Zirconium deposition was measured by X-ray fluorescence (XRF) analysis with a Rigaku ZSX Primus IVi. The stoichiometry and elemental bonding states in the films were characterized by X-ray photoelectron spectroscopy (XPS) using a Thermo Fisher Scientific K-Alpha. The film morphology and the thickness were evaluated by field-emission scanning electron microscopy (FE-

SEM) and atomic force microscopy (AFM) conducted on a Hitachi High-Tech S-4800 and a Bruker Multimode 8, respectively. The crystallinity was investigated by X-ray diffraction (XRD) analysis using a Rigaku Ultima IV.

Electric characterization of ZrO_2 films

The electric properties of the obtained ZrO_2 films were evaluated by preparing metal–insulator–semiconductor (MIS) structures of Pt/ZrO_2/*p*-Si. The deposition temperature of the ZrO_2 layer was 350 °C. The Pt electrodes were deposited onto the ZrO_2 films through a shadow mask at room temperature by DC magnetron sputtering using a Sanyu Electron SC-701MC. The thicknesses of the Pt electrode and *p*-Si substrate were 100 nm and 0.5 mm, respectively. Capacitance–voltage (*C–V*) curves for the MIS structure were acquired using a precision LCR meter (Agilent, 4980A). The current–voltage (*I–V*) curves were also acquired (Keithley, Sourcemeter 2450).

The antiferroelectric properties of the ZrO_2 films were evaluated using MIM structures of TiN/ZrO_2/TiN/*p*-Si. The deposition temperature of the ZrO_2 layer was 340 °C. The TiN top electrodes were deposited onto the ZrO_2 films through a shadow mask at room temperature by DC magnetron sputtering using a Shibaura Mechatronics Corporation CFS-4EP-LL. The thicknesses of the TiN top and bottom electrode and the *p*-Si substrate were 100 nm, 50 nm, and 0.5 mm, respectively. The ferroelectric properties were measured using a ferroelectric tester (Radiant, Multiferroic II). ZrO_2 films were annealed in vacuum at 600 °C under Ar flow for 1 min using an infrared-lamp heating system (ADVANCE RIKO, RTP-6).

RESULTS AND DISCUSSION

Volatility and thermal stability of the $Zr(dmap)_4$ precursor

Figure 1(a) shows the TGA curves of the $Zr(dmap)_4$ precursor and the conventional precursors TEMAZ and $CpZr(NMeEt)_3$. The TG curve of $Zr(dmap)_4$ shows a clean single-step, without decomposition or residue formation at 760 Torr. The 50% volatile temperature ($TG_{1/2}$) which indicates the volatility of the ALD precursors was 250 °C. Compared with the TEMAZ and $CpZr(NMeEt)_3$, the $Zr(dmap)_4$ showed lower volatility because of its bulky ligand structure. The vapor pressure of the $Zr(dmap)_4$ was 1.0 Torr at 153 °C. Figure 1(b) shows the DSC thermograms of the $Zr(dmap)_4$ and the conventional precursors TEMAZ and $CpZr(NMeEt)_3$. $Zr(dmap)_4$ is a liquid precursor at room temperature; thus, no peaks appeared in its thermogram in the temperature range from room temperature to its thermal decomposition temperature. The thermal decomposition peak of $Zr(dmap)_4$ was observed >390.0 °C. By contrast, the thermal decomposition peaks of the TEMAZ and $CpZr(NMeEt)_3$ precursors were confirmed to appear at >248.8 °C and >283.7 °C, respectively. These data indicate that $Zr(dmap)_4$ exhibits greater thermal stability than TEMAZ and $CpZr(NMeEt)_3$ and

can therefore be used in ALD processes at temperatures greater than 300 °C.

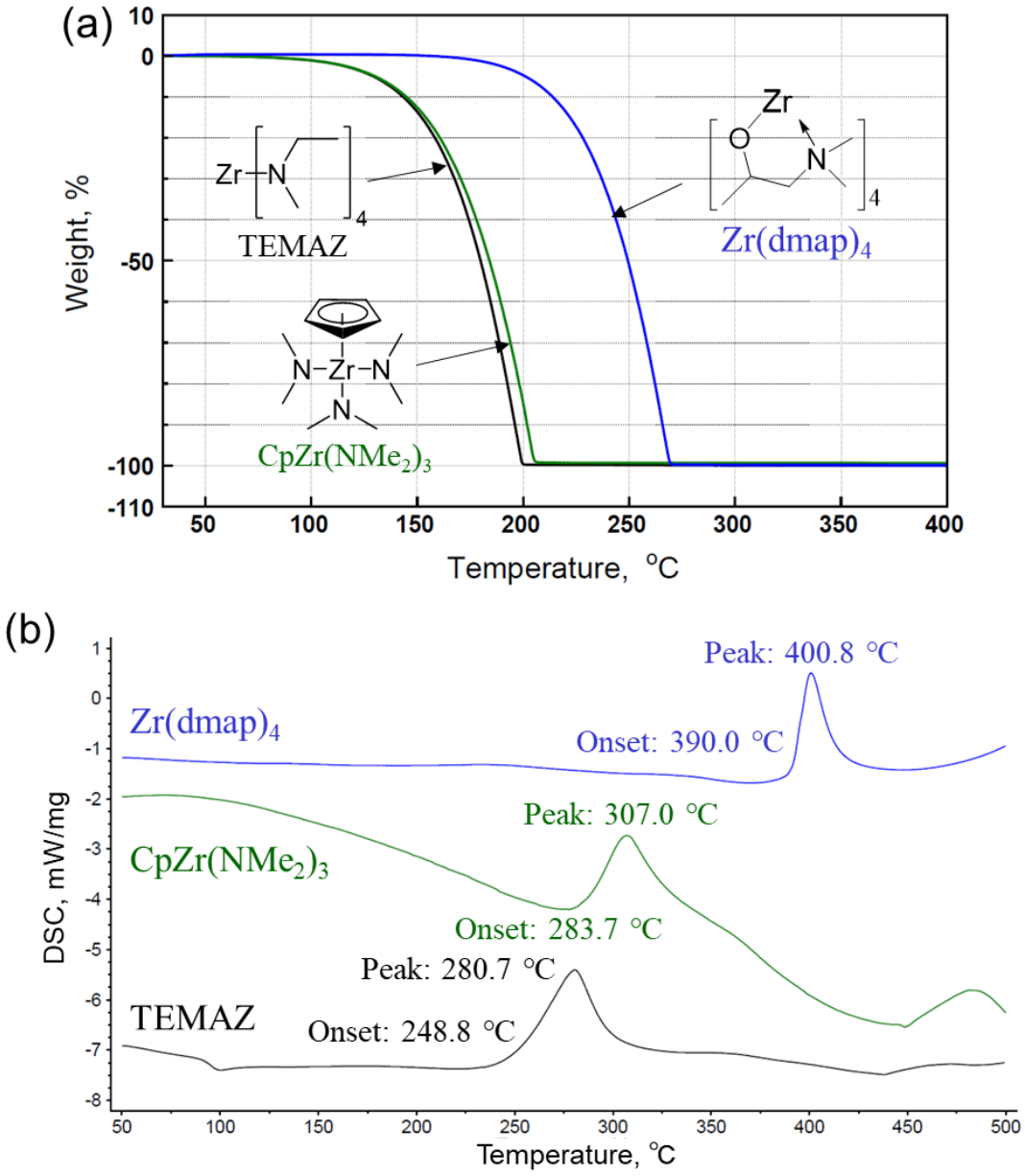

Fig. 1 Volatility and thermal stability of the $Zr(dmap)_4$ precursor and two conventional Zr precursors: (a) thermogravimetric analysis (TGA) curves and (b) differential scanning calorimetry (DSC) thermograms.

ALD testing of the $Zr(dmap)_4$ precursor

The optimal dosing time was evaluated to study its effect on the growth rate using $Zr(dmap)_4$ with O_3 as a co-reactant. The $Zr(dmap)_4$ dosing time was varied at temperatures ranging from 350 to 400 °C. Figure 2(a) shows the thickness per cycle as a function of the $Zr(dmap)_4$ dose. A constant film

growth rate was observed in the temperature range 350–375 °C. This observation indicates that the Zr precursor half-reaction reached a self-limiting state when the precursor was supplied for more than 5 s. The film growth rate increased as the $Zr(dmap)_4$ dosing time was increased from 5 to 10 s at 400 °C. The $Zr(dmap)_4$ growth rate became saturated when the precursor dosing time was longer than 10 s. The difference in saturation times at different temperatures is attributed mainly to the $Zr(dmap)_4$ precursor being adsorbed onto the substrate at lower temperatures but also being dissociated from substrate at higher temperatures. As a result, the saturation time increased at higher temperatures. The saturated growth rate was 0.31, 0.40, and 0.53 Å/cycle at 350, 375, and 400 °C, respectively. The film growth rate of TEMAZ has been reported to be 0.96 Å/cycle at 250 °C, and that of $CpZr(NMeEt)_3$ has been reported to be 0.9 Å/cycle at 300 °C. [27, 29] The $Zr(dmap)_4$ precursor exhibits a lower film growth rate than TEMAZ and $CpZr(NMeEt)_3$ but enables ALD at temperatures greater than 350 °C.

Figure 2(b) shows the deposition-temperature dependence of the growth rate of ZrO_2 films during the $Zr(dmap)_4 + O_3$ ALD test. The film growth rate increased slightly as the deposition temperature was increased from 300 to 400 °C. Precursor saturation was confirmed in a test of the $Zr(dmap)_4$ dosing time; this result therefore indicates that the saturated growth rate of $Zr(dmap)_4$ changed with the deposition temperature. To confirm the thermal decomposition temperature of the $Zr(dmap)_4$ on the substrate during the ALD process, a pyrolysis test was carried out without a co-reactant. In the pyrolysis test using the ALD chamber, $Zr(dmap)_4$ vapor was supplied for 1000 s, which is the same dosing time as the ALD test condition (10 s for 100 times, or 1000 s in total). Film growth was not observed during the pyrolysis test from 300 to 350 °C, indicating that $Zr(dmap)_4$ was not decomposed in this temperature range. At temperatures greater than 375 °C, film decomposition started in the absence of a co-reactant, indicating that $Zr(dmap)_4$ on the substrate was decomposed by thermal energy; a Zr-containing oxide film was consequently detected. However, an ALD precursor was not heated for 1000 s in the actual ALD sequence because of the co-reactant dose; we therefore considered that thermal decomposition at temperatures greater than 375 °C did not substantially affect the ALD behavior.

Figure 2(c) shows the film grown rate as a function of the ALD cycle number. The film thickness was measured by X-ray reflectivity (XRR). The thickness increased linearly with increasing number of ALD cycles at 350, 375, and 400 °C, indicating that the film grew at a constant rate; that is, $Zr(dmap)_4$ exhibits excellent thickness control characteristics. The results verified saturation behavior and a linear dependence of the growth rate on the number of cycles. We therefore conclude that $Zr(dmap)_4$ showed ALD-type growth behavior.

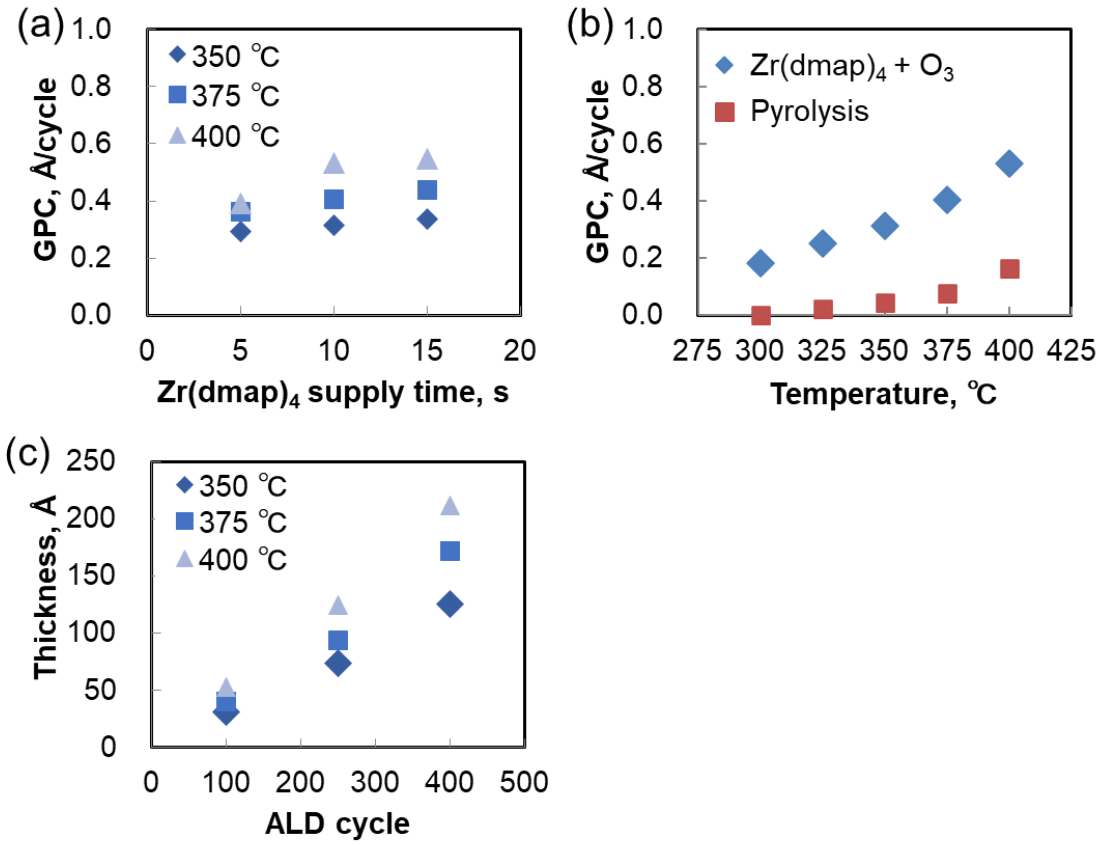

Fig. 2 ALD behavior of the $Zr(dmap)_4$ precursor using O_3 as a co-reactant. (a) Growth rate as a function of the $Zr(dmap)_4$ supply time at substrate temperatures of 350, 375, and 400 °C. (b) Temperature dependence of the growth rate of $Zr(dmap)_4$ films and a pyrolysis test. (c) Film thickness as a function of the number of ALD cycles at 350, 375, and 400 °C.

Characterization of ZrO_2 films deposited using the $Zr(dmap)_4$ precursor with O_3 or water

The film purity in terms of stoichiometry and atomic-scale contamination levels were measured using XPS. Table 2 shows the composition of as-deposited ZrO_2 films deposited onto the Si substrate at 350, 375, and 400 °C using O_3 or H_2O as a co-reactant. The corresponded XPS depth profiles and high-resolution spectra are displayed in Figure 3. Impurities were not detected in the film deposited using O_3 as a co-reactant. The film deposited at 350 °C using H_2O as a co-reactant contained 3.9 at% carbon and carbide as impurities. This carbon contamination was reduced with increasing deposition temperature, although the carbide content in the film remained at 2.4 at%. The carbide content could likely be reduced by extending the H_2O dosing time. The O/Zr ratio was similar to the ideal O/Zr composition, indicating that $Zr(dmap)_4$ exhibits high reactivity even though it contains a bulky ligand; thus, the oxidation reaction on the substrate proceeded completely, especially for O_3

ALD.

Table 2 Composition of zirconium oxide films grown on Si using $Zr(dmap)_4$ with different co-reactants, as measured by XPS.

Co-reactant	T_{growth}, °C	Zr, at%	O, at%	C, at%	N, at%	Si, at%	O/Zr ratio
O_3	350	32.3	66.4	0.0	0.0	1.3	2.06
O_3	375	33.8	65.7	0.0	0.0	0.5	1.94
O_3	400	33.1	66.9	0.0	0.0	0.0	2.02
H_2O	350	31.5	63.7	3.9	0.0	0.9	2.02
H_2O	400	32.5	65.1	2.4	0.0	0.0	2.00

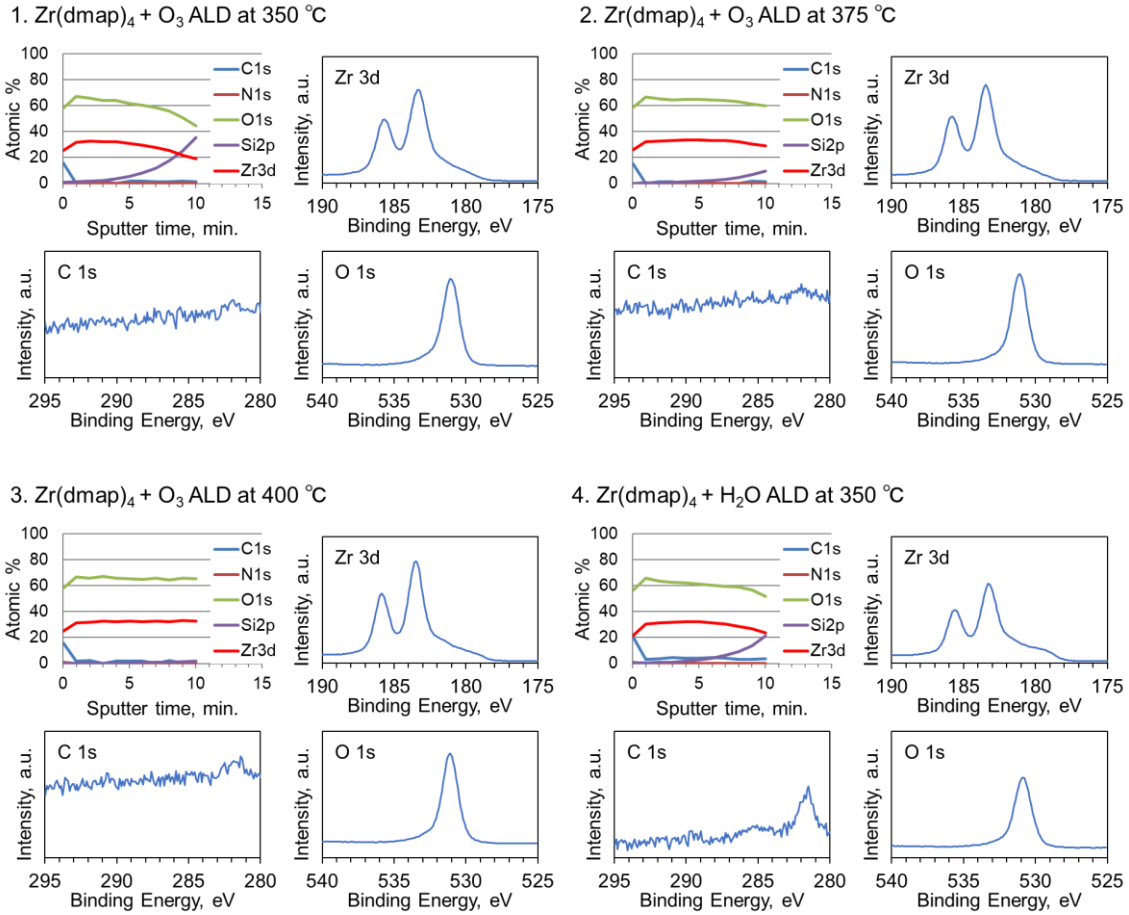

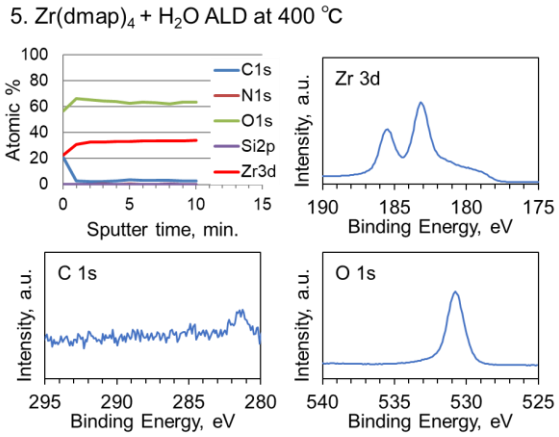

Fig. 3 XPS spectra of ZrO_2 films made by $Zr(dmap)_4$ + O_3 or H_2O ALD corresponding to Table 2.

Figure 4 shows XRD patterns of 12.5–26.1 nm-thick ZrO_2 films deposited from $Zr(dmap)_4$ using O_3 (a) or H_2O (b) as a co-reactant at temperatures ranging from 350 to 400 °C. Peaks were observed in the patterns of all the samples, indicating that the films were crystalline. The intensity of these reflections increased with increasing deposition temperature. The diffraction peaks matched those of the ZrO_2 tetragonal phase (JCPDS card no. 80-0965). The commonly observed monoclinic phase was not detected in studies where conventional precursors were used. [19, 27] Our results show that crystalline ZrO_2 films can be deposited using $Zr(dmap)_4$ and either co-reactant at temperatures greater than 350 °C, without a post-annealing process.

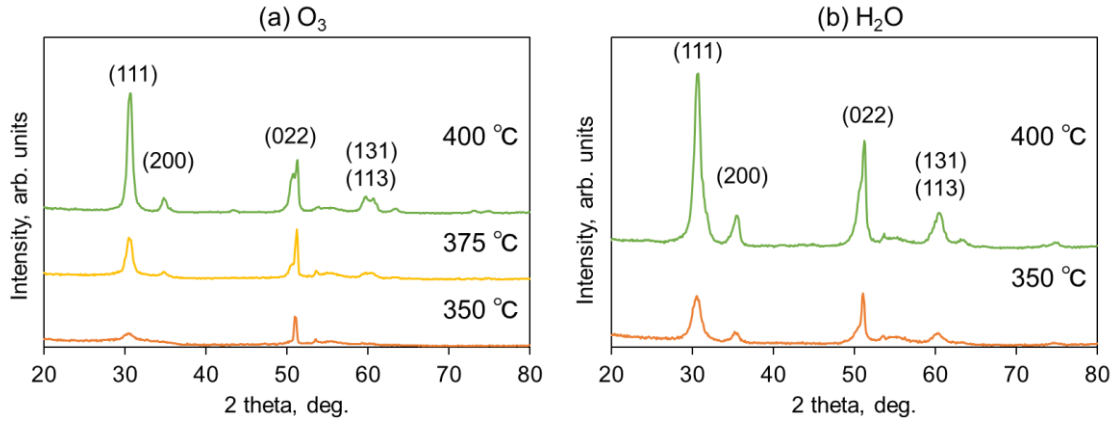

Fig. 4 XRD patterns of 12.5–26.1 nm-thick ZrO_2 films deposited onto Si using $Zr(dmap)_4$ and (a) O_3 or (b) H_2O as a co-reactant. The thicknesses of the ZrO_2 films were 12.5 nm (a, 350 °C), 17.2 nm (a, 375 °C), 21.1 nm (a, 400 °C), 15.5 nm (b, 350 °C), and 26.1 nm (b, 400 °C).

Table 3 shows the thicknesses and the rms roughness values of the ZrO_2 films, as measured by FE-SEM and AFM, respectively. The corresponded FE-SEM and AFM images are displayed in

Figure 5 and 6. For the films deposited at 350 °C, both the film deposited with O_3 as a co-reactant and that deposited with H_2O as a co-reactant show low rms values of 0.63 and 0.50 nm, respectively. When the deposition temperature was increased, the rms values slightly increased to 0.94 nm (O_3, 375 °C), 1.36 nm (O_3, 400 °C), and 0.71 nm (H_2O, 400 °C) because of crystallization of the ZrO_2 films. These results indicate that smooth ZrO_2 films can be prepared using $Zr(dmap)_4$ at temperatures greater than 350 °C.

Table 3 The rms roughness values and thicknesses of the ZrO_2 films, as determined by AFM and FE-SEM.

Co-reactant	T_{growth}, °C	Thickness of ZrO_2, nm	rms, nm
O_3	350	12.5	0.63
O_3	375	17.2	0.94
O_3	400	21.1	1.36
H_2O	350	15.5	0.50
H_2O	400	26.1	0.71

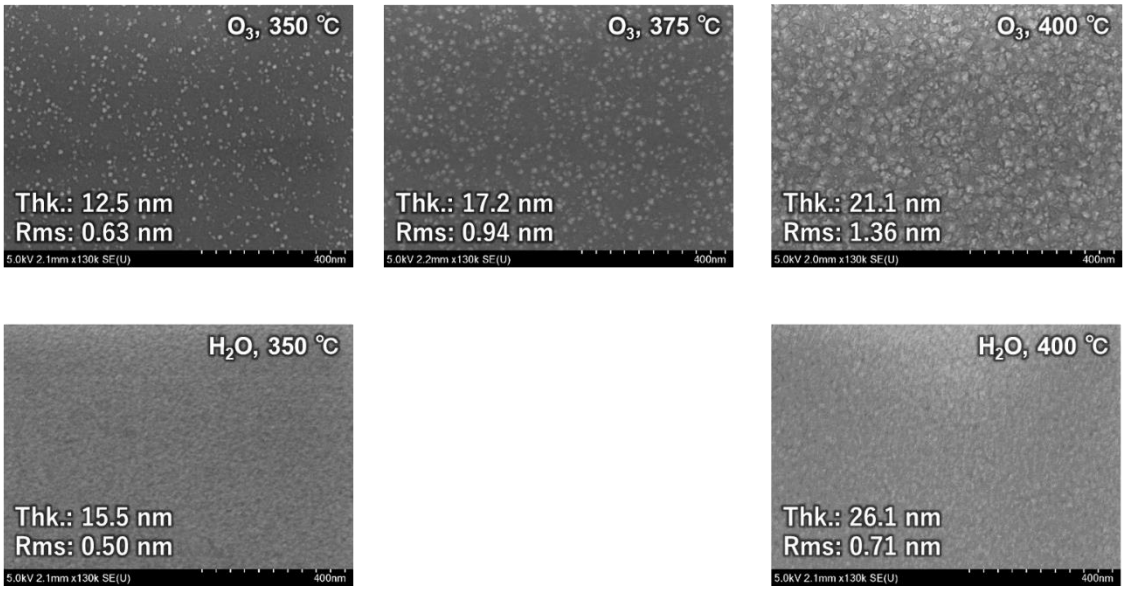

Fig. 5 FE-SEM images of ZrO_2 films made by $Zr(dmap)_4$ + O_3 or H_2O ALD corresponding to Table 3.

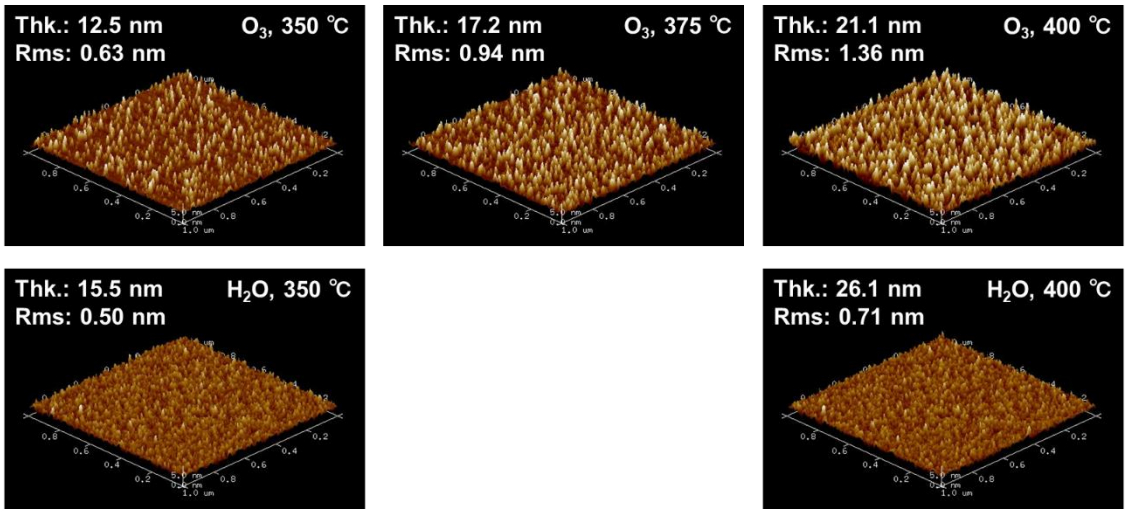

Fig. 6 AFM images of ZrO_2 films made by $Zr(dmap)_4$ + O_3 or H_2O ALD corresponding to Table 3.

Electric characterization of ZrO_2 films deposited using the $Zr(dmap)_4$ precursor with O_3

Figure 7(a) shows capacitance–voltage (*C–V*) curves for the Pt/ZrO_2/*p*-Si MIS capacitors. The size of top Pt electrode was 0.0154 mm^2, and the thickness and deposition temperature for the ZrO_2 layer were 10.5 nm and 350 °C, respectively. When a negative bias was applied, the capacitance value of the MIS capacitor became 0.32 nF. From this result, the dielectric constant of the ZrO_2 layers was roughly evaluated to be 23.6, which is similar to previously reported values ~26 (TEMAZ). [21, 29] However, when a positive bias was applied to the MIS capacitors, the capacitance values decreased substantially because of the formation of a depletion layer in the *p*-Si. A counterclockwise hysteresis was observed in the *C–V* curves. This behavior is likely attributable to holes being trapped at the interface between the ZrO_2 and *p*-Si, resulting in a shift of the flat-band voltage because of the screening of the electric field.

Figure 7(b) shows the leakage current density versus electric field curves for the Pt/ZrO_2/*p*-Si MIS capacitor. The leakage current density at −1 MV/cm and the breakdown electric field were approximately 5.2×10^{-7} A/cm^2 and 5.2 MV/cm, respectively. These values are comparable to or better than those of previously reported MIS capacitors fabricated using ZrO_2 layers prepared from conventional ALD precursors, including solid or heteroleptic ALD precursors. [17, 21, 23, 29] Thus, these results indicate that a ZrO_2 layer with high electronic performance can be attained even when a liquid homoleptic ALD precursor such as $Zr(dmap)_4$ is used.

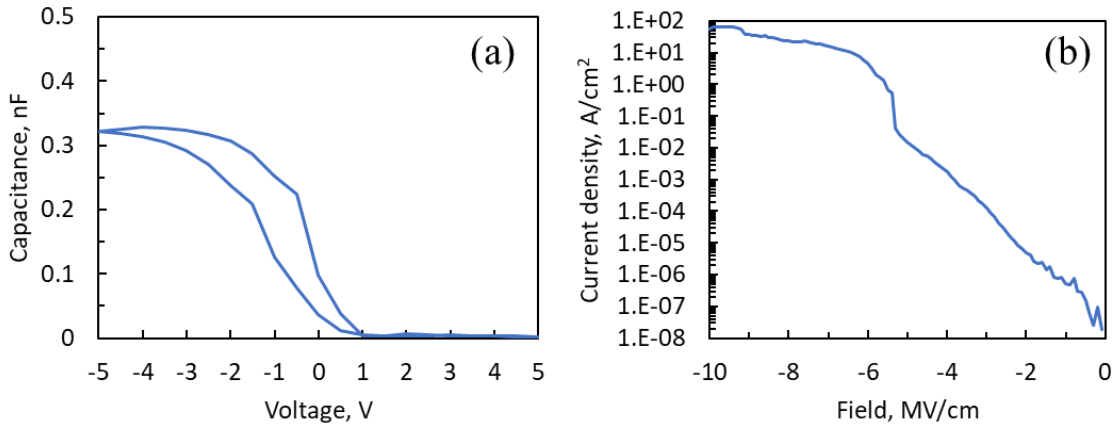

Fig. 7 Electric characterization of ZrO_2 films deposited at 350 °C. (a) *C–V* curves of a Pt/ZrO_2/*p*-Si MIS capacitor at a frequency of 100 kHz. (b) *I–V* curves of a Pt/HfO_2/*p*-Si MIS capacitor.

Figure 8 shows *P–E* curves for the TiN/ ZrO_2/TiN/*p*-Si MIM capacitors after the capacitors were annealed at 600 °C for 1 min. The area of the top TiN electrode was 0.015 mm^2, and the thickness and deposition temperature for the ZrO_2 layer were 12.1 nm and 340 °C. A ZrO_2 film was deposited at 340 °C using $Zr(dmap)_4$ with O_3 as a co-reactant. The *P–E* curves of the ZrO_2 film exhibited double loops and showed a small $2P_r$ value of 6.0 μC/cm^2, indicating that the film exhibited an antiferroelectric nature which is similar to previously reported. [9] These results show that the antiferroelectric ZrO_2 films can be easily fabricated even when a liquid homoleptic ALD precursor such as $Zr(dmap)_4$ is used.

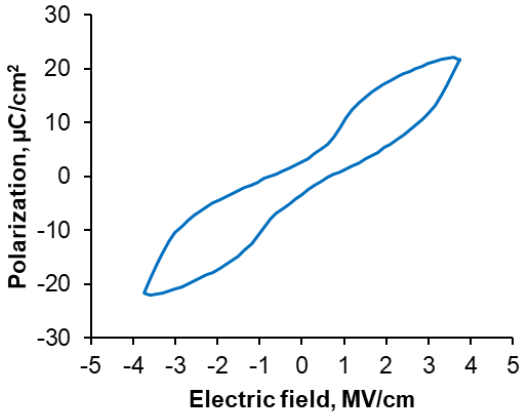

Fig. 8 Polarization versus electric field (*P–E*) curves for the ZrO_2 film.

SUMMARY AND CONCLUSIONS

We evaluated the newly developed zirconium precursor $Zr(dmap)_4$, which is a liquid at room temperature and exhibits high thermal stability at temperatures of nearly 400 °C. This thermal stability

is a great advantage of $Zr(dmap)_4$ over amide-type precursors such as TEMAZ and $CpZr(DMA)_3$. Compared with $ZrCl_4$, $Zr(dmap)_4$ exhibits greater volatility (1.0 Torr at 153 °C). Even though $Zr(dmap)_4$ exhibits high thermal stability, it does not contain chlorine in its molecular structure, thereby avoiding the generation of corrosive byproducts and chlorine contaminants in the film, unlike $ZrCl_4$. $Zr(dmap)_4$ has a homoleptic structure. Thus, it is expected to be less expensive to manufacture than heteroleptic precursors because heteroleptic precursors generally require additional manufacturing steps for their chemical synthesis.

We demonstrated ALD of ZrO_2 films using $Zr(dmap)_4$ with O_3 or H_2O as a co-reactant. The ALD window was estimated to range from 300 to 400 °C. The film growth rate when O_3 was used as a co-reactant was 0.31, 0.40, and 0.53 Å/cycle at 350, 375, and 400 °C, respectively. XPS analysis showed that high-purity ZrO_2 films could be deposited at temperatures greater than 350 °C when O_3 was used as a co-reactant. The use of H_2O as a co-reactant led to a small amount of carbon contamination in the resultant film. The ZrO_2 films deposited at all of the investigated temperatures were crystallized without a post-annealing process and exhibited a smooth surface. A ZrO_2 layer with high electronic performance and an antiferroelectric nature could be deposited at temperatures greater than 340 °C using O_3 coreactant. Thus, these data indicate that there is still room for improvement of the electronic performance of ZrO_2 film deposited by $Zr(dmap)_4$ greater than 375 °C. We deduce that these film properties were achieved by high-temperature ALD realized by the excellent thermal stability of $Zr(dmap)_4$. Therefore, we concluded that $Zr(dmap)_4$ is a strong candidate as a ZrO_2 ALD precursor for the temperature range 300–400 °C.

ACKNOWLEDGMENTS

We are grateful to ADEKA Corporation for providing the $Zr(dmap)_4$ precursor and its vapor pressure, TGA, and DSC data.

This work was partly supported by “Crossover Alliance to Create the Future with People, Intelligence and Materials” and Advanced Research Infrastructure for Materials and Nanotechnology (ARIM) Japan from the Ministry of Education, Culture, Sports, Science and Technology (MEXT).

REFERENCES

(1) Robertson, J. High dielectric constant gate oxides for metal oxide Si transistors. *Reports on Progress in Physics* **2006**, *69* (2), 327-396. DOI: 10.1088/0034-4885/69/2/r02.

(2) Robertson, J. Band offsets of wide-band-gap oxides and implications for future electronic devices. *Journal of Vacuum Science & Technology B* **2000**, *18* (3), 1785-1791. DOI: 10.1116/1.591472.

(3) Nohira, H.; Tsai, W.; Besling, W.; Young, E.; Petry, J.; Conard, T.; Vandervorst, W.; De Gendt, S.; Heyns, M.; Maes, J.; et al. Characterization of ALCVD-Al2O3 and ZrO2 layer using X-ray

photoelectron spectroscopy. *Journal of Non-Crystalline Solids* **2002**, *303* (1), 83-87. DOI: 10.1016/s0022-3093(02)00970-5.

(4) Ben Amor, S.; Rogier, B.; Baud, G.; Jacquet, M.; Nardin, M. Characterization of zirconia films deposited by rf magnetron sputtering. *Materials Science and Engineering B-Solid State Materials for Advanced Technology* **1998**, *57* (1), 28-39. DOI: 10.1016/s0921-5107(98)00205-0.

(5) Hubbard, K. J.; Schlom, D. G. Thermodynamic stability of binary oxides in contact with silicon. *Journal of Materials Research* **1996**, *11* (11), 2757-2776. DOI: 10.1557/jmr.1996.0350.

(6) Robertson, J.; Wallace, R. M. High-K materials and metal gates for CMOS applications. *Materials Science and Engineering: R: Reports* **2015**, *88*, 1-41. DOI: 10.1016/j.mser.2014.11.001.

(7) Gusev, E. P.; Cartier, E.; Buchanan, D. A.; Gribelyuk, M.; Copel, M.; Okorn-Schmidt, H.; D'Emic, C. Ultrathin high-K metal oxides on silicon: processing, characterization and integration issues. *Microelectronic Engineering* **2001**, *59* (1-4), 341-349. DOI: 10.1016/s0167-9317(01)00667-0.

(8) Panda, D.; Tseng, T. Y. Growth, dielectric properties, and memory device applications of ZrO2 thin films. *Thin Solid Films* **2013**, *531*, 1-20. DOI: 10.1016/j.tsf.2013.01.004.

(9) Muller, J.; Boscke, T. S.; Schroder, U.; Mueller, S.; Brauhaus, D.; Bottger, U.; Frey, L.; Mikolajick, T. Ferroelectricity in Simple Binary ZrO2 and HfO2. *Nano Lett* **2012**, *12* (8), 4318-4323. DOI: 10.1021/nl302049k From NLM PubMed-not-MEDLINE.

(10) Park, M. H.; Kim, H. J.; Kim, Y. J.; Moon, T.; Kim, K. D.; Hwang, C. S. Toward a multifunctional monolithic device based on pyroelectricity and the electrocaloric effect of thin antiferroelectric HfxZr1-xO2 films. *Nano Energy* **2015**, *12*, 131-140. DOI: 10.1016/j.nanoen.2014.09.025.

(11) Lu, B.; Li, P. L.; Tang, Z. H.; Yao, Y. B.; Gao, X. S.; Kleemann, W.; Lu, S. G. Large Electrocaloric Effect in Relaxor Ferroelectric and Antiferroelectric Lanthanum Doped Lead Zirconate Titanate Ceramics. *Scientific Reports* **2017**, *7*. DOI: 10.1038/srep45335.

(12) Smith, R. C.; Ma, T. Z.; Hoilien, N.; Tsung, L. Y.; Bevan, M. J.; Colombo, L.; Roberts, J.; Campbell, S. A.; Gladfelter, W. L. Chemical vapour deposition of the oxides of titanium, zirconium and hafnium for use as high-k materials in microelectronic devices. A carbon-free precursor for the synthesis of hafnium dioxide. *Advanced Materials for Optics and Electronics* **2000**, *10* (3-5), 105-114. DOI: 10.1002/1099-0712(200005/10)10:3/5<105::aid-amo402>3.3.co;2-a.

(13) Will, J.; Mitterdorfer, A.; Kleinlogel, C.; Perednis, D.; Gauckler, L. J. Fabrication of thin electrolytes for second-generation solid oxide fuel cells. *Solid State Ionics* **2000**, *131* (1-2), 79-96. DOI: 10.1016/s0167-2738(00)00624-x.

(14) Crowell, J. E. Chemical methods of thin film deposition: Chemical vapor deposition, atomic layer deposition, and related technologies. *Journal of Vacuum Science & Technology A* **2003**, *21* (5), S88-S95. DOI: 10.1116/1.1600451.

(15) Chang, J. P.; Lin, Y. S. Highly conformal ZrO2 deposition for dynamic random access memory application. *Journal of Applied Physics* **2001**, *90* (6), 2964-2969. DOI: 10.1063/1.1389756.
(16) Cassir, M.; Goubin, F.; Bernay, C.; Vernoux, P.; Lincot, D. Synthesis of ZrO2 thin films by atomic layer deposition: growth kinetics, structural and electrical properties. *Applied Surface Science* **2002**, *193* (1-4), 120-128. DOI: 10.1016/s0169-4332(02)00247-7.
(17) Kukli, K.; Ritala, M.; Aarik, J.; Uustare, T.; Leskela, M. Influence of growth temperature on properties of zirconium dioxide films grown by atomic layer deposition. *Journal of Applied Physics* **2002**, *92* (4), 1833-1840. DOI: 10.1063/1.1493657.
(18) Hausmann, D. M.; Kim, E.; Becker, J.; Gordon, R. G. Atomic layer deposition of hafnium and zirconium oxides using metal amide precursors. *Chemistry of Materials* **2002**, *14* (10), 4350-4358. DOI: 10.1021/cm020357x.
(19) Hausmann, D. M.; Gordon, R. G. Surface morphology and crystallinity control in the atomic layer deposition (ALD) of hafnium and zirconium oxide thin films. *Journal of Crystal Growth* **2003**, *249* (1-2), 251-261. DOI: 10.1016/s0022-0248(02)02133-4.
(20) Niinisto, J.; Kukli, K.; Heikkila, M.; Ritala, M.; Leskela, M. Atomic Layer Deposition of High-k Oxides of the Group 4 Metals for Memory Applications. *Advanced Engineering Materials* **2009**, *11* (4), 223-234. DOI: 10.1002/adem.200800316.
(21) Weinreich, W.; Tauchnitz, T.; Polakowski, P.; Drescher, M.; Riedel, S.; Sundqvist, J.; Seidel, K.; Shirazi, M.; Elliott, S. D.; Ohsiek, S.; et al. TEMAZ/O-3 atomic layer deposition process with doubled growth rate and optimized interface properties in metal-insulator-metal capacitors. *Journal of Vacuum Science & Technology A* **2013**, *31* (1). DOI: 10.1116/1.4766281.
(22) Miikkulainen, V.; Leskela, M.; Ritala, M.; Puurunen, R. L. Crystallinity of inorganic films grown by atomic layer deposition: Overview and general trends. *Journal of Applied Physics* **2013**, *113* (2). DOI: 10.1063/1.4757907.
(23) Putkonen, M.; Niinisto, J.; Kukli, K.; Sajavaara, T.; Karppinen, M.; Yamauchi, H.; Niinisto, L. ZrO2 thin films grown on silicon substrates by atomic layer deposition with Cp2Zr(CH3)(2) and water as precursors. *Chemical Vapor Deposition* **2003**, *9* (4), 207-212. DOI: 10.1002/cvde.200306254.
(24) Putkonen, M.; Niinisto, L. Zirconia thin films by atomic layer epitaxy. A comparative study on the use of novel precursors with ozone. *Journal of Materials Chemistry* **2001**, *11* (12), 3141-3147. DOI: 10.1039/b105272c.
(25) Niinisto, J.; Kukli, K.; Tamm, A.; Putkonen, M.; Dezelah, C. L.; Niinisto, L.; Lu, J.; Song, F.; Williams, P.; Heys, P. N.; et al. Advanced cyclopentadienyl precursors for atomic layer deposition of ZrO2 thin films. *Journal of Materials Chemistry* **2008**, *18* (28), 3385-3390. DOI: 10.1039/b802523a.

(26) Niinisto, J.; Hatanpaa, T.; Kariniemi, M.; Mantymaki, M.; Costelle, L.; Mizohata, K.; Kukli, K.; Ritala, M.; Leskela, M. Cycloheptatrienyl-Cyclopentadienyl Heteroleptic Precursors for Atomic Layer Deposition of Group 4 Oxide Thin Films. *Chemistry of Materials* **2012**, *24* (11), 2002-2008. DOI: 10.1021/cm2030735.
(27) Niinisto, J.; Kukli, K.; Kariniemi, M.; Ritala, M.; Leskela, M.; Blasco, N.; Pinchart, A.; Lachaud, C.; Laaroussi, N.; Wang, Z. Y.; et al. Novel mixed alkylamido-cyclopentadienyl precursors for ALD of ZrO2 thin films. *Journal of Materials Chemistry* **2008**, *18* (43), 5243-5247. DOI: 10.1039/b810922b.
(28) Nishida, A.; Hatase, M.; Yoshino, T.; Ooe, Y.; Mitsui, C. METHOD FOR MANUFACTURING THIN FILM. Japan WO/2022/107769, PCT/JP2021/042094, 2022.
(29) Yun, S. J.; Lim, J. W.; Lee, J. H. PEALD of zirconium oxide using tetrakis(ethylmethylamino)zirconium and oxygen. *Electrochemical and Solid State Letters* **2004**, *7* (12), F81-F84. DOI: 10.1149/1.1814591.

Chapter 5

Atomic Layer Deposition of Hafnium-Zirconium-Oxide Films Using a Novel Liquid Cocktail Precursor Containing $Hf(dmap)_4$ and $Zr(dmap)_4$

ABSTRACT

Hafnium-oxide-based films are attracting attention for use in ferroelectric devices because of their high compatibility with complementary metal-oxide semiconductor (COMS) processes and excellent ferroelectricity compared with that of perovskite-based films, even when the hafnium-oxide-based films are less than 10 nm thick. In particular, $Hf_xZr_{1-x}O_2$ (HZO) thin films exhibit high remanent polarization values. In this paper, atomic layer deposition (ALD) of HZO thin films was studied using a novel liquid homoleptic cocktail precursor known as FER-1, which is composed of tetrakis(1-(N,N-dimethylamino)-2-propoxy)hafnium [$Hf(dmap)_4$] and tetrakis(1-(N,N-dimethylamino)-2-propoxy)zirconium [$Zr(dmap)_4$] in a 1:1 mol% mixture. Among conventional ALD precursors, ZrO_2 precursors exhibit lower thermal stability than HfO_2 precursors; thus, the deposition temperature is limited by the Zr precursor processing temperature (320 °C). Both $Hf(dmap)_4$ and $Zr(dmap)_4$ have been shown by differential scanning calorimetry analysis to be stable at temperatures as high as 371 °C. These compounds have a similar vapor pressure, similar ALD window, and excellent mixture stability. FER-1 is a volatile compound that shows a very clean thermogravimetry curve without decomposition or residue formation at 10 Torr. We carried out ALD of HZO films using FER-1 and O_3 as an oxidant. ALD saturation was studied in the temperature range 260–400 °C and was observed at 360 °C. The film growth rate was 0.48 Å/cycle. The concentrations of Hf and Zr in the films were measured by X-ray photoelectron spectroscopic analysis and found to be 50:50 at%, which is the same as the Hf/Zr concentration ratio in the precursor mixture. These results indicate that film concentration can be controlled by manipulating the precursor concentration. Metal–insulator–metal TiN–HfO_2–TiN devices were fabricated to evaluate the ferroelectric properties of the HZO films deposited by ALD. The remanent polarization value of the ALD film deposited at 340 °C was 36.9 μC/cm^2. We concluded that FER-1 is a promising precursor for high-temperature ALD.

INTRODUCTION

Hafnium(IV) oxide (HfO_2) is an attractive compound for use in semiconductor devices because of its high dielectric constant (~25), wide bandgap energy (~5.7 eV), high refractive index, and good chemical stability. [1-3] It has been used in various industrial applications, including as a gate dielectric material in complementary metal oxide semiconductor (CMOS) devices and as a capacitor dielectric material in dynamic random access memory devices. [4] In addition, hafnium-oxide-based films are well suited for use in CMOS fabrication processes and exhibit excellent ferroelectricity compared with perovskite-based films such as $SrBi_2Ta_2O_9$ (SBT) and $Pb(Zr_xTi_{1-x})O_3$ (PZT), even when the hafnium oxide films are less than 10 nm thick. [5, 6] In particular, $Hf_xZr_{1-x}O_2$ (HZO) thin films exhibit high remanent polarization values and have attracted attention for use in ferroelectric devices such as ferroelectric random access memory, ferroelectric field-effect transistors, and ferroelectric tunnel junctions. [7-9]

In general, both HfO_2 and ZrO_2 films are deposited by physical vapor deposition (PVD) or chemical vapor deposition (CVD). [10-13] PVD and CVD exhibit high film growth rates, enabling high productivity. However, step coverage with PVD and CVD is insufficient in principle, which makes the deposition of HfO_2 and ZrO_2 films onto nanosized three-dimensional structures difficult. [14] Hence, atomic layer deposition (ALD) processes have been used to deposit HfO_2 and ZrO_2 films that exhibit good coverage and high purity and are free of pinholes. [15] To obtain high-quality HfO_2 and ZrO_2 films, high-temperature processing is important to control the crystal phase of HfO_2 and ZrO_2. [16]

As ALD precursors for ferroelectric HZO film, tetrakis(dimethylamido)hafnium(IV) (TDMAH), tetrakis(dimethylamido)zirconium(IV) (TDMAZ), tetrakis(ethylmethylamido)hafnium(IV) (TEMAH), tetrakis(ethylmethylamido)zirconium(IV) (TEMAZ), cyclopentadienyl tris(dimethylamino)hafnium ($CpHf(NMe_2)_3$), and tris(dimethylamino)zirconium ($CpZr(NMe_2)_3$) have been widely investigated. [7, 17-22] However, amide-type precursors such as TDMAH, TDMAZ, TEMAH, and TEMAZ exhibit low thermal stability and are therefore difficult to use at temperatures greater than 300 °C because of thermal decomposition. [15, 23] Cyclopentadienyl (Cp) amide-type precursors tend to exhibit ALD behavior at higher temperatures than amide-type precursors. However, $CpZr(NMe_2)_3$ is less thermally stable than $CpHf(NMe_2)_3$; thus, the HZO film deposition temperature is limited to the $CpZr(NMe_2)_3$ limitation temperature. [24] Therefore, the maximum ALD temperature that can be used in conjunction with $CpHf(NMe_2)_3$ and $CpZr(NMe_2)_3$ is 320 °C. [21, 22]

Table 1 Composition of ALD precursors for HZO films.

Name	TEMAZ	TEMAH	$CpZr(NMe_2)_3$	$CpHf(NMe_2)_3$	$Zr(dmap)_4$	$Hf(dmap)_4$
Reference		16			This study	This study
Structure	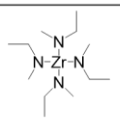	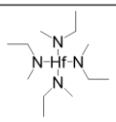	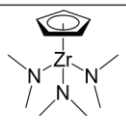	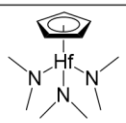	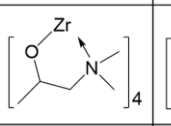	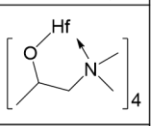
Ligand type	✓ Homoleptic	✓ Homoleptic	Heteroleptic	Heteroleptic	✓ Homoleptic	✓ Homoleptic
Temperature	<300 ℃	<300 ℃	<300 ℃	✓ 250-350 ℃	✓ 300-375 ℃	✓ 300-375 ℃

ALD generally comprises four steps: precursor dose, precursor purge, co-reactant dose, and co-reactant purge (Fig. 1(a)). The most common method of producing a HZO film by ALD is the supercycle process combined with binary ALD processes involving Hf and Zr precursors. An ALD sequence of an eight-step ternary process is needed to deposit a homogeneous film using two precursors (Fig. 1(b)), which increases the total processing time and, thus, the manufacturing cost of HZO films. In addition, supplying two precursors requires two supply lines in the ALD tool. The ALD tool thus becomes larger and more complicated, resulting in higher processing and maintenance costs and more complex device operation.

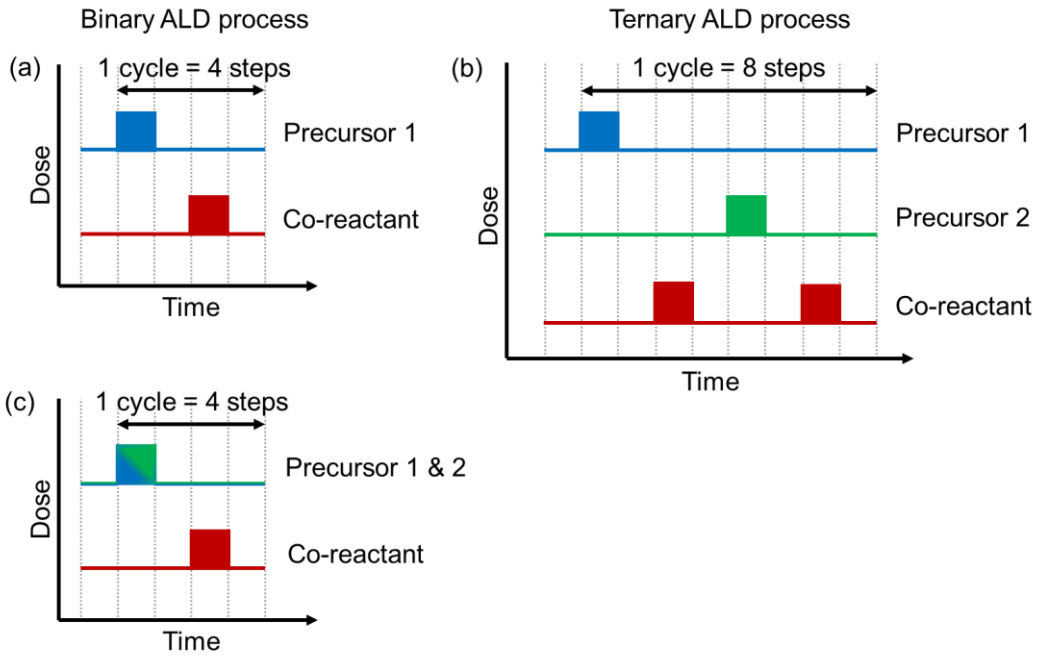

Fig. 1 Schematic of the ALD sequence: (a) the binary ALD process with one precursor and one co-reactant; (b) the ternary ALD process with two precursors and one co-reactant; and (c) the binary ALD process with a cocktail precursor and one co-reactant.

We have previously developed numerous Hf and Zr aminoalkoxide compounds and identified good candidates for use as ALD precursors. [25, 26] The Hf aminoalkoxide precursor tetrakis(1-

(*N*,*N*-dimethylamino)-2-propoxy)hafnium [$Hf(dmap)_4$] and the Zr aminoalkoxide precursor tetrakis(1-(*N*,*N*-dimethylamino)-2-propoxy)zirconium [$Zr(dmap)_4$] are liquids at room temperature and have been shown by differential scanning calorimetry (DSC) analysis to be stable at temperatures as high as 371 °C or greater.[27] In this paper, the ALD of HZO thin films was studied using a novel liquid homoleptic cocktail precursor: a $Hf(dmap)_4$ and $Zr(dmap)_4$ 1:1 mol% mixture named FER-1. The purpose of this study is to achieve high-temperature (>300 °C) ALD of a HZO film using a novel cocktail precursor with high thermal stability and a binary ALD process to achieve greater productivity and lower manufacturing costs. Similar thermal properties of the components and good mixture stability are critical for a cocktail precursor. If ligands are eliminated by decomposition, the same aminoalcohol-type byproduct will be generated because $Hf(damp)_4$ and $Zr(dmap)_4$ are homoleptic and have the same ligands in their molecular structures. The Cp amide-type precursors are heteroleptic and have both Cp and amide ligands in their molecular structures. When ligands are eliminated, Cp and amide-type byproducts will be generated. These byproducts can lead to a disproportionation reaction and Cp–Cp dimerization,[28] which is an exothermic reaction. Therefore, we believe that conventional Cp amide-type precursors are not desirable for use in cocktail precursors.

EXPERIMENTAL

Volatility and thermal stability testing

Thermogravimetric analysis (TGA) of the cocktail precursor was carried out at 10 Torr in an Ar-filled glovebox using a Rigaku ThermoPlus2 TG8120. The thermal decomposition temperature was measured by differential scanning calorimetry (DSC; Bruker AXS DSC 3100). The ^{1}H-NMR data for the cocktail precursor were obtained using a JEOL ECA-400 spectrometer.

ALD testing of cocktail precursor with oxidants

HZO films were deposited using a cross-flow ALD reactor (SAMCO AD-230LP-H) with O_3 as a co-reactant. Prior to deposition, Si(100) substrates were cut into 25 mm × 25 mm squares and cleaned with 0.5% hydrofluoric acid (HF) solution for 1 min to remove the native oxide layer. The cleaned wafer was then dried under N_2 gas and immediately loaded into the ALD chamber. Before the ALD process, the wafer was heated for 30 min to stabilize its temperature. The cocktail precursor was provided by ADEKA (ORCERA FER-1). The cocktail precursor was added to a stainless steel canister and heated at 150 ° C. The precursor supply method was vapor drawing using Ar carrier gas at 50 sccm. The chamber pressure was maintained at ~0.20 Torr by control of the Ar process gas. The ALD cycles were performed in the following sequence: O_3 ALD: FER-1 (supply time: 5–30 s)/Ar purge (15 s)/O_3 (10 s)/Ar purge (15 s). Several deposited HZO films were annealed in vacuum at 600 °C under Ar flow for 1 min using an infrared-lamp heating system (ADVANCE RIKO, RTP-6).

Characterization of deposited HZO films

The extent of Hf and Zr deposition was measured by X-ray fluorescence (XRF; Rigaku ZSX Primus IVi). The stoichiometry and elemental bonding states in the films were studied by X-ray photoelectron spectroscopy (XPS; Thermo Fisher Scientific K-Alpha). The film morphology and thickness were evaluated by field-emission scanning electron microscopy (FE-SEM; Hitachi High-Tech S-4800) and atomic force microscopy (AFM; Bruker Multimode 8), respectively. The crystallinity was characterized by X-ray diffraction (XRD; Rigaku Ultima IV).

Electric characterization of HZO films

The electric properties of the HZO films were evaluated using metal–insulator–semiconductor (MIS) structures of Pt/HZO/*p*-Si. The thicknesses of the Pt electrode and *p*-Si substrate were 100 nm and 0.5 mm, respectively. Capacitance–voltage (*C–V*) curves for the MIS structure were recorded using a precision LCR meter (Agilent, 4980A). The current–voltage (*I–V*) curves were also recorded (Keithley, Sourcemeter 2450).

The ferroelectric properties of the HZO films were evaluated using MIM structures of TiN/HZO/TiN/*p*-Si. The thicknesses of the TiN top and bottom electrode and the *p*-Si substrate were 100 nm, 50 nm, and 0.5 mm, respectively. The ferroelectric properties were measured using a ferroelectric tester (Radiant, Multiferroic II).

RESULTS AND DISCUSSION

Volatility and thermal stability of the cocktail precursor

Figure 1(a) shows the variation of the vapor pressure of the $Hf(damp)_4$ and $Zr(dmap)_4$ precursors with temperature. The vapor pressure of the $Hf(dmap)_4$ reached 1.0 Torr at 153 °C, and that of the $Zr(dmap)_4$ reached 1.0 Torr at 154 °C. This indicates that both precursors have the same vapor pressure because both vapor pressure curves overlapped at around 153–154 °C. When $Hf(damp)_4$ and $Zr(dmap)_4$ are mixed, they can be volatized simultaneously because their vapor pressures are similar. Figure 1(b) shows the TGA curves of $Hf(dmap)_4$, $Zr(dmap)_4$, and the cocktail precursor. The TGA curves are clean, with a single step without decomposition or residue formation at 760 Torr. These results indicate that no side reaction occurs as a result of mixing and heating the $Hf(dmap)_4$ and $Zr(dmap)_4$ precursors. The 50% volatile temperature ($TG_{1/2}$) was 249 °C at 760 Torr.

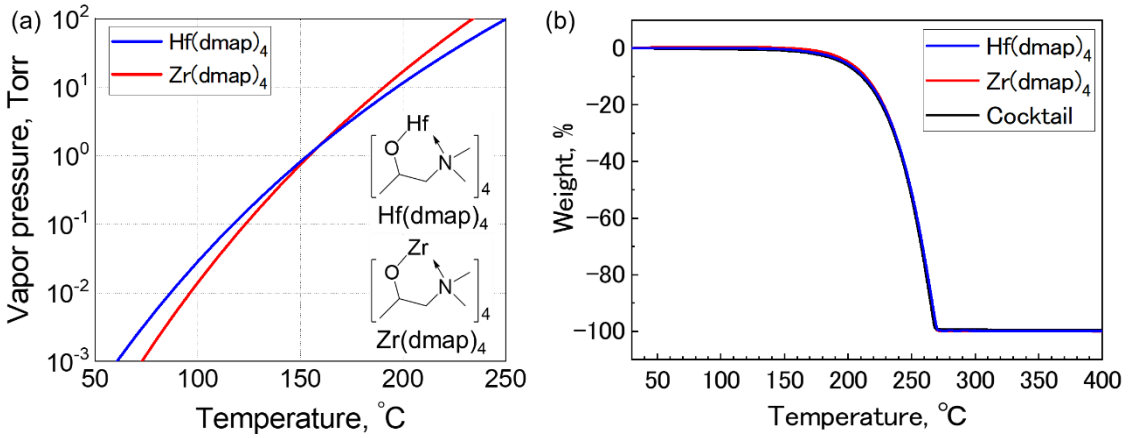

Fig. 1 (a) Variation of the vapor pressure of $Hf(dmap)_4$ and $Zr(dmap)_4$ as a function of temperature. (b) TGA curve of $Hf(damp)_4$, $Zr(dmap)_4$, and the cocktail precursor at 760 Torr.

Long-term thermal stability of the cocktail precursor

An ALD precursor is heated to a high temperature during the ALD process. Long-term thermal stability at the vaporization temperature for more than a few months is critical for ALDs used industrially, where long-life precursors enable films to be continuously produced without stopping the production line. The TGA results indicate that $Hf(dmap)_4$, $Zr(dmap)_4$, and the cocktail precursor exhibit high thermal stability and high volatility. We therefore evaluated the long-term thermal stability of the cocktail precursor as a novel compound. The cocktail precursor was placed in a stainless steel canister and heated at the vaporization temperature (150 °C), which is the temperature at which it vaporizes at 1 Torr, and then periodically characterized by TGA and ^{1}H-NMR. Figure 1(a) shows the change in the TG residue of the cocktail precursor recorded during the long-term thermal stability test. The TG residue was less than 1.0% until 8 weeks. At 12 weeks, the TG residue reached 1.4%, indicating that thermal decomposition had started during the 12-week stability test at 150 °C. Figure 2(b) shows ^{1}H-NMR spectra acquired during the long-term thermal stability test. The spectrum of the cocktail precursor did not change before or after it was heated at 150 °C for 12 weeks. The extent of thermal decomposition detected by TGA is very small; thus, the ^{1}H-NMR spectra did not change because of the detection limit of the NMR spectrometer. Therefore, the cocktail precursor was confirmed to exhibit excellent long-term thermal stability for at least 12 weeks.

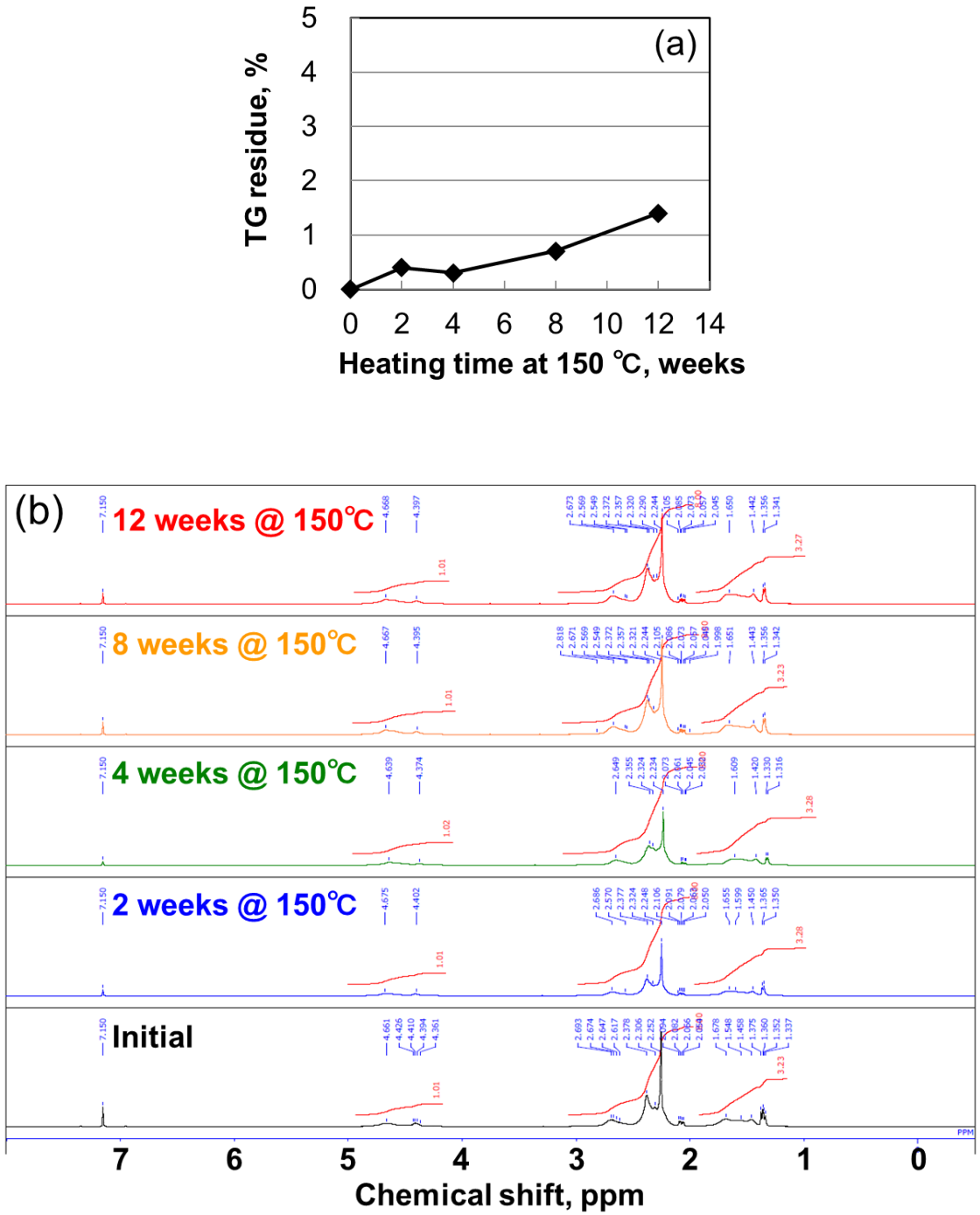

Fig. 2 (a) TG residue change recorded during a long-term thermal stability test of the cocktail precursor at 150 °C for 12 weeks. (b) ^{1}H-NMR spectra of the cocktail precursor acquired during the long-term thermal stability test at 150 °C for 12 weeks.

ALD testing of the cocktail precursor

An evaluation of the optimal dosing time was carried out to study its effect on the growth

rate using the cocktail precursor with O_3 as a co-reactant. The cocktail precursor dosing time was varied at 360 °C. Figure 3(a) shows the thickness per cycle and the film density as functions of the cocktail precursor dose. The film growth rate increased as the cocktail precursor dosing time was increased from 5 to 10 s. The film density then decreased as the cocktail precursor dosing time was increased from 5 to 10 s. The cocktail precursor growth rate and film density saturated when the Hf precursor dosing time was longer than 10 s. The Hf precursor half-reaction reached a self-limited state. The saturated growth rate and film density were 0.46 Å/cycle and 7.45 g/cm^3, respectively, at 360 °C. The film densities of HfO_2 and ZrO_2 are 9.68 g/cm^3 and 5.68 g/cm^3, respectively. The density of the HZO film was intermediate between those of the HfO_2 and ZrO_2 films, indicating that the HZO film had similar concentrations of Hf and Zr.

The O_3 dosing time was also optimized. Figure 3(b) shows the O_3 dosing time dependence of the film growth rate and the film density at 360 °C. A constant growth rate was observed when the dosing time was 300 ms or longer. Small variations in the growth rate were confirmed at shorter dosing times because of incomplete oxidation of the metal precursor. Because carbon contamination originating from the ligand was a concern in this range of short dosing times, a dosing time of at least 300 ms was considered necessary.

Figure 3(c) shows the temperature dependence of the growth rate in the cocktail precursor + O_3 ALD test process. The film growth rate increased slightly as the deposition temperature was increased from 300 to 360 °C. When the deposition temperature was increased to 400 °C, the film growth rate increased because thermal decomposition began. However, the film density was almost constant with increasing deposition temperature.

Figure 3(d) shows the film thickness as a function of the number of ALD cycles. The film thickness, which was measured by X-ray reflectometry (XRR), increases linearly with increasing number of ALD cycles at 360 °C. This result indicates that the film grew with a constant growth rate; that is, the cocktail precursor exhibits excellent thickness-control characteristics. The linear dependence and saturation behavior were verified, and we therefore concluded that the cocktail precursor exhibited ALD-type growth behavior.

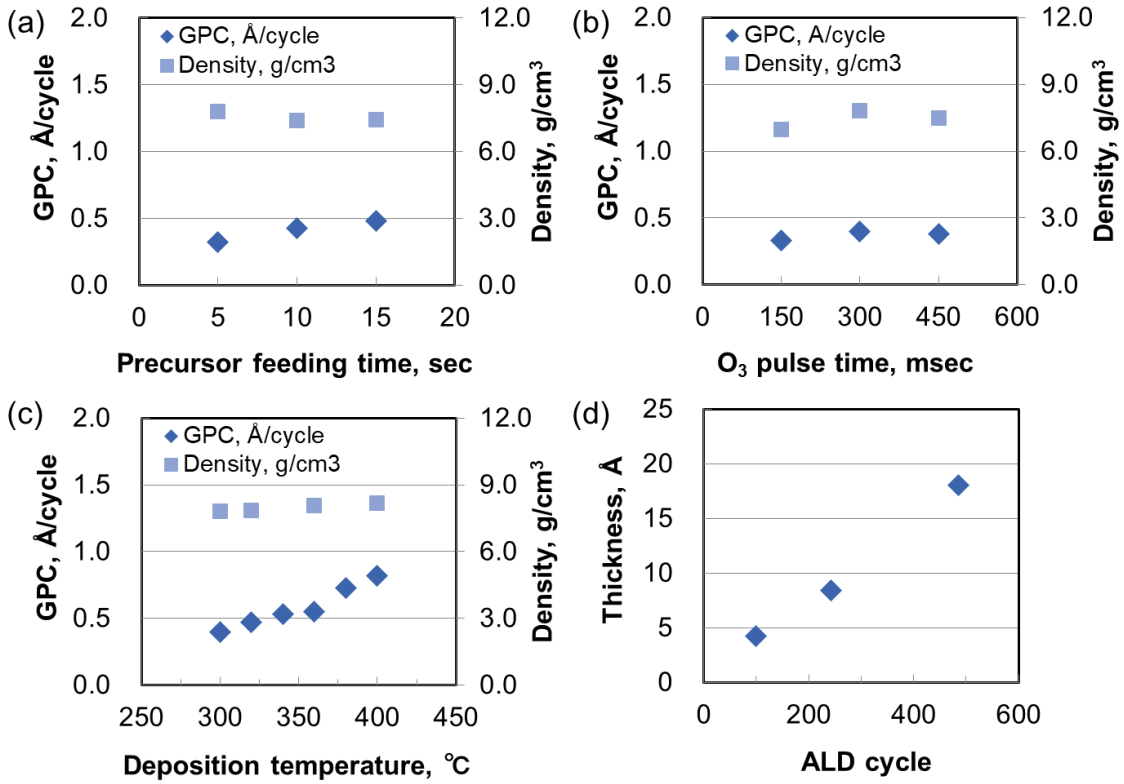

Fig. 3 ALD behavior of the cocktail precursor when O_3 is used as a co-reactant. (a) Growth rate and density as a function of the cocktail precursor supply time at a substrate temperature of 360 °C. (b) Growth rate and density as a function of the O_3 supply time at a substrate temperature of 360 °C. (c) Temperature dependence of the growth rate and density of the cocktail precursor. (d) Film thickness as a function of the number of ALD cycles at 360 °C.

Characterization of HZO films deposited by the cocktail precursor with O_3 as a co-reactant

The compositions of the films and the concentrations of impurities in the films were measured by XPS analysis. Table 2 shows the composition of the as-deposited HZO films obtained at each deposition temperature (340, 360, and 380 °C) when O_3 was used as a co-reactant. The corresponded XPS depth profiles and high-resolution spectra are displayed in Figure 4. The film deposited at 340 °C using O_3 as a co-reactant contained 3.7 at% of carbide as an impurity. This carbide contamination was reduced with increasing deposition temperature. At 380 °C, carbide was detected at a concentration of 2.0 at% in the film. This situation can likely be improved by extending the O_3 dosing time or increasing the O_3 partial pressure in the chamber. The Hf/Zr ratio was 1.00–1.05, which is the same as the Hf/Zr ratio in the cocktail precursor. Thus, the Hf/Zr ratio in the film can be controlled by manipulating the precursor Hf/Zr concentration. The crystal phase of HZO varies depending on the Hf and Zr contents; the ferroelectric phase transition therefore depends on the Hf/Zr

ratio. [18] With the proposed cocktail precursor, a HZO film with a targeted composition can be stably and easily deposited.

Table 2 Composition of as-deposited HZO films grown on silicon at different temperatures, as characterized by XPS.

T_{growth}, °C	Hf, at%	Zr, at%	O, at%	C, at%	N, at%	Hf/Zr ratio
340	18.0	18.0	60.3	3.7	0.0	1.00
360	17.4	17.1	63.0	2.5	0.0	1.02
380	18.7	17.8	61.5	2.0	0.0	1.05

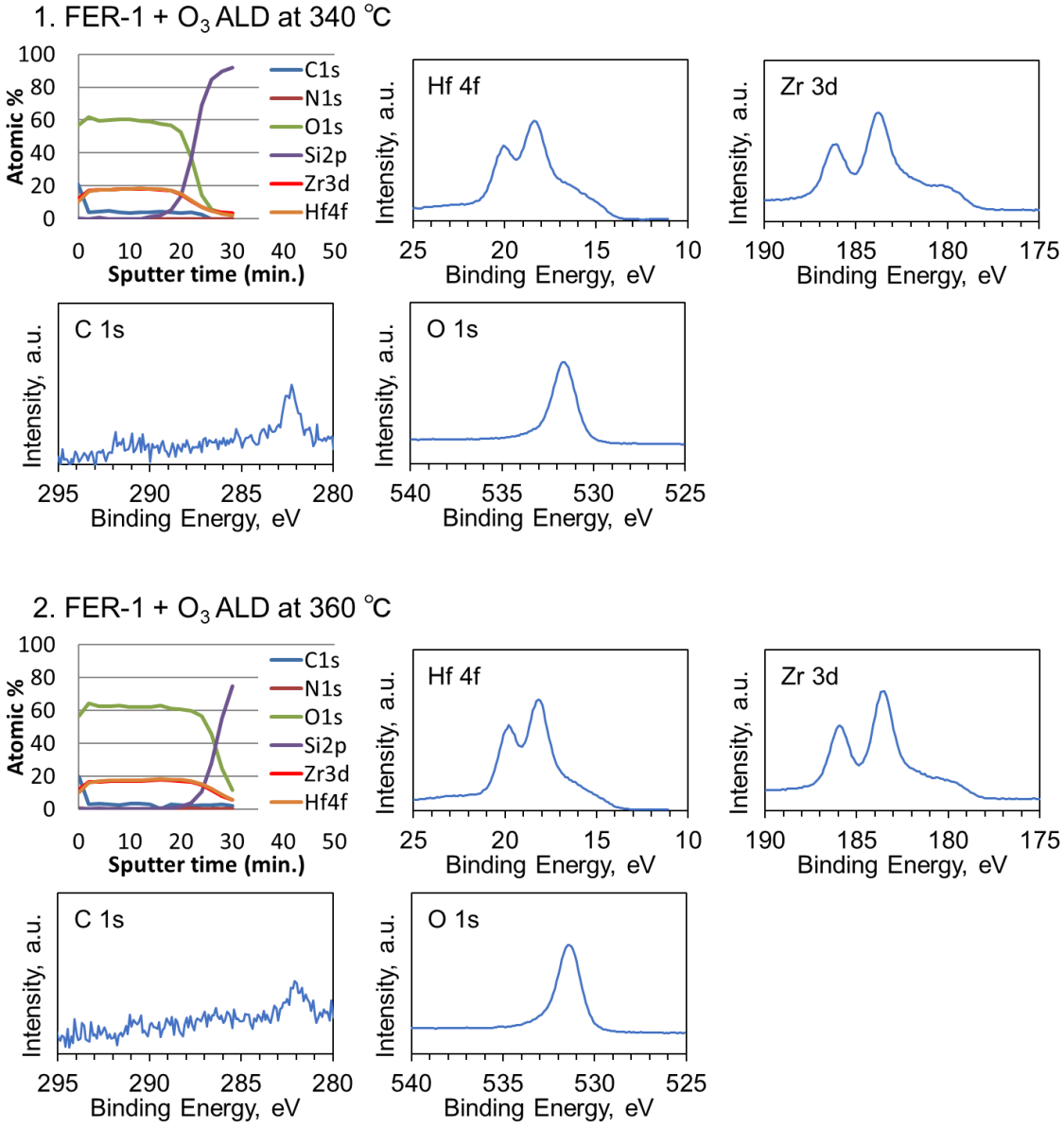

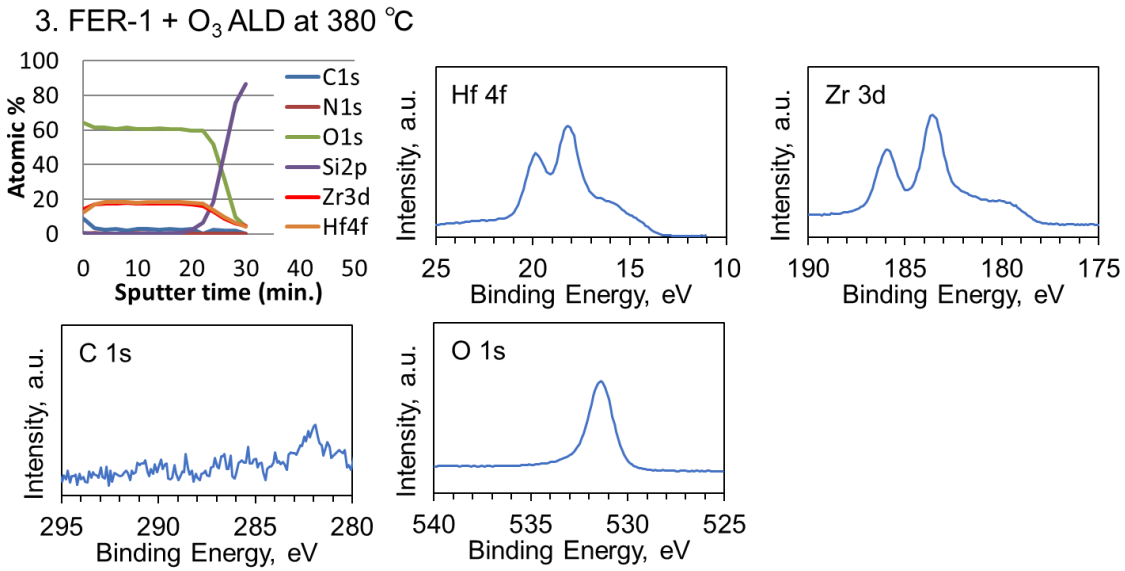

Fig. 4 XPS spectra of HZO films made by FER-1 + O_3 ALD corresponding to Table 2.

Figure 5 shows XRD patterns of HZO films with a thickness of 10 nm, deposited from the cocktail with O_3 as a co-reactant at temperatures ranging from 340 to 380 °C. Crystalline peaks are observed in the patterns of the films deposited in this temperature range, and the intensity of these reflections increased with increasing deposition temperature. The diffraction peaks at $2\theta \approx 30.5°$ match the orthorhombic phase (111 orientation) and tetragonal phase (111 orientation) of the HZO films. At deposition temperatures from 340 to 380 °C, crystalline HZO films can be deposited using the cocktail precursor and O_3 as a co-reactant, without post-annealing because of the high thermal stability of the cocktail precursor.

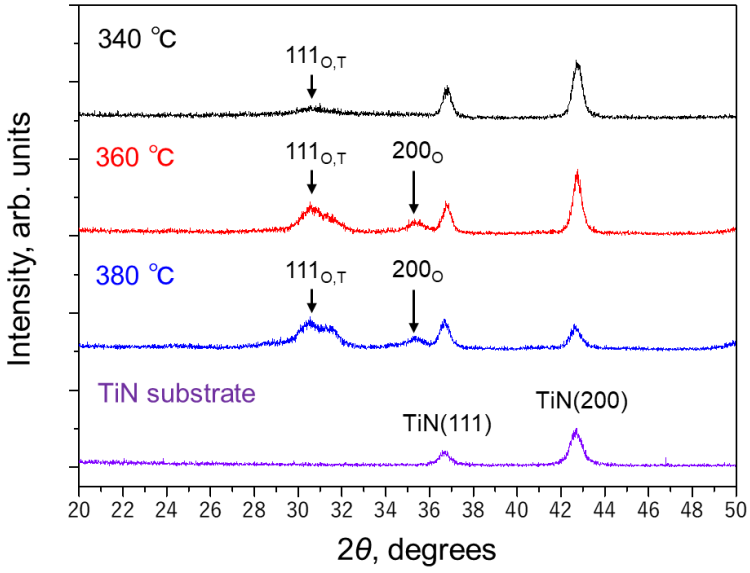

Fig. 5 XRD patterns of HZO films with thicknesses of 9.1 nm (340 °C), 10.6 nm (360 °C), and 10.0 nm (380 °C), deposited onto TiN using the cocktail precursor and O_3 as a co-reactant.

Table 3 shows the root mean square (rms) roughness values and HZO film thicknesses obtained from AFM measurements. The corresponded FE-SEM and AFM images are displayed in Figure 6 and 7. The films deposited at 340 °C exhibited low rms roughness values of 0.36 nm. At deposition temperatures greater than 360 °C, the rms values increased to 0.62 nm (360 °C) and 0.57 nm (380 °C) because of crystallization of the HZO films. These ~10 nm-thick films exhibited smooth surfaces.

Table 3 Rms roughness values and thicknesses of HZO films.

T_{growth}, °C	Thickness of HZO, nm	rms, nm
340	9.1	0.36
360	10.6	0.62
380	10.0	0.57

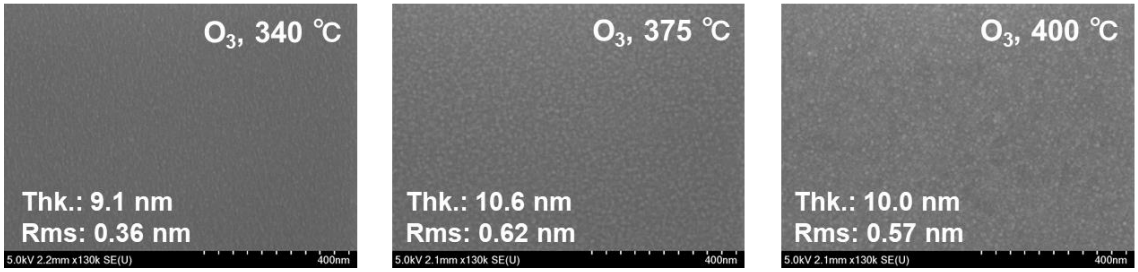

Fig. 6 FE-SEM images of HZO films made by FER-1 + O_3 ALD corresponding to Table 3.

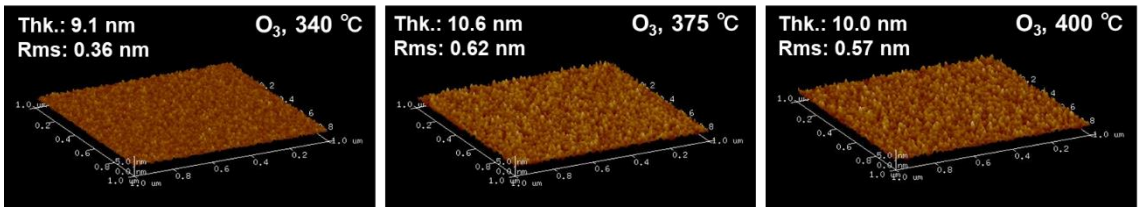

Fig. 7 AFM images of HZO films made by FER-1 + O_3 ALD corresponding to Table 3.

Electric characterization of HZO films deposited using the cocktail precursor with O_3

Figure 8(a) shows *C–V* curves for the Pt/HZO/*p*-Si MIS capacitors before and after the capacitors were annealed at 600 °C for 1 min. The area of the top Pt electrode was 0.0154 mm^2, and the thickness and deposition temperature for the HZO layer were 10.6 nm and 360 °C, respectively. When a negative bias was applied, the capacitance value of both of the MIS capacitors was 0.28 nF.

These results indicate that the dielectric constant of the HZO layers was ~20.8. However, when a positive bias was applied to the MIS capacitors, the capacitance values substantially decreased because of the formation of a depletion layer in the *p*-Si. A counterclockwise hysteresis was observed in the *C–V* curves, likely because holes were trapped at the interface between the HZO and the *p*-Si, resulting in a shift of the flatband voltage due to the screening of the electric field. The hysteresis of the MIS capacitor was narrowed when the device was annealed at 600 °C for 1 min. When a negative bias was applied, both of the MIS capacitors exhibited a capacitance value of 0.56 nF. The results show that the dielectric constant of the HZO layers was ~40.9. This increase in the dielectric constant indicates that the proportion of the tetragonal phase in the film increased as a result of thermal annealing.

Figure 8(b) shows the leakage current density versus electric field curves for the Pt/HZO/*p*-Si MIS capacitors. The leakage current density at 1 MV/cm and the breakdown electric field were approximately 3.6×10^{-7} A/cm^2 and −7.4 MV/cm, respectively. These values are better than those previously reported for MIS capacitors fabricated using a HZO layer prepared from amide ALD precursors (4.8×10^{-7} A/cm^2 and 6.4 MV/cm). [29] When the device was annealed at 600 °C for 1 min, the leakage current density at 1 MV/cm (7.0×10^{-5} A/cm^2) and breakdown electric field (−7.1 MV/cm) became slightly worse because of crystallization.

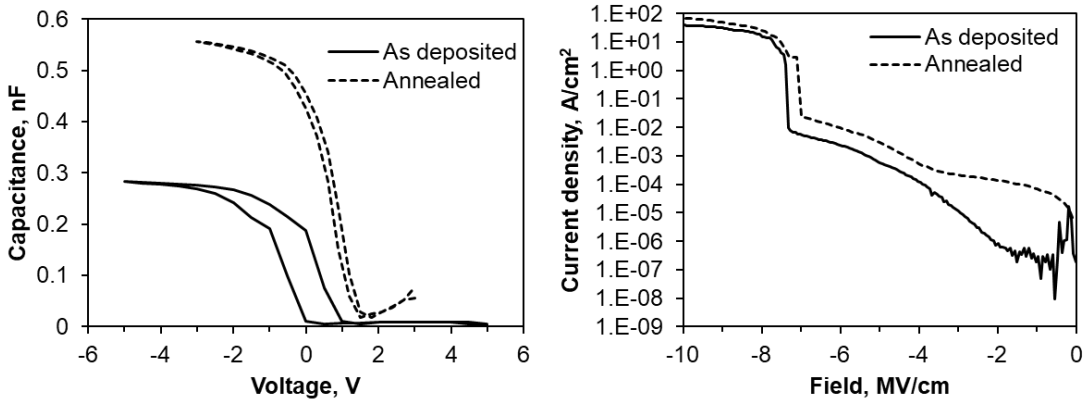

Fig. 8 Electric characterization of as-deposited (solid line) and annealed (dashed line) HZO films. (a) *C–V* curves of the Pt/HZO/*p*-Si MIS capacitor at a frequency of 100 kHz. The HZO film deposition temperature was 360 °C. The MIS structure was Pt/HZO (10.6 nm)/*p*-type Si/Pt. The post-annealing was conducted at 600 °C for 1 min. (b) *I–V* curves of the Pt/HZO/*p*-Si MIS capacitors before and after annealing at 600 °C for 1 min. The thickness and deposition temperature of the HZO layer were 10.6 nm and 360 °C, respectively.

Figure 9 shows *P–E* curves for the TiN/HZO/TiN/*p*-Si MIM capacitors after the capacitors were annealed at 600 °C for 1 min. The area of the top TiN electrode was 0.015 mm^2, and the thickness and deposition temperature for the HZO layer were 10.6 nm and 340 °C, respectively.

TiN/HfO_2/TiN/*p*-Si and TiN/ZrO_2/TiN/*p*-Si MIM capacitors were also fabricated for comparison using $Hf(dmap)_4$ and $Zr(dmap)_4$, respectively. A HZO film was deposited at 340 °C using $Hf(dmap)_4$ and $Zr(dmap)_4$ with O_3 as a co-reactant. The *P*–*E* curves of the HZO film exhibited typical ferroelectric hysteresis loops with symmetrical switching characteristics, and the film showed a large remanent polarization ($2P_r$) of 36.9 μC/cm^2. However, the HfO_2 film exhibited paraelectric behavior. Meanwhile, the ZrO_2 film exhibited double loops and showed a small $2P_r$ value of 6.0 μC/cm^2, indicating that the film exhibited an antiferroelectric nature. These results show that the ferroelectric HZO films can be easily fabricated using a simple cocktail precursor consisting of a mixture of $Hf(dmap)_4$ and $Zr(dmap)_4$. In addition, the ferroelectric properties can be tuned by varying the $Hf(dmap)_4$-to-$Zr(dmap)_4$ ratio in the cocktail precursor, which is highly advantageous for manufacturing processes.

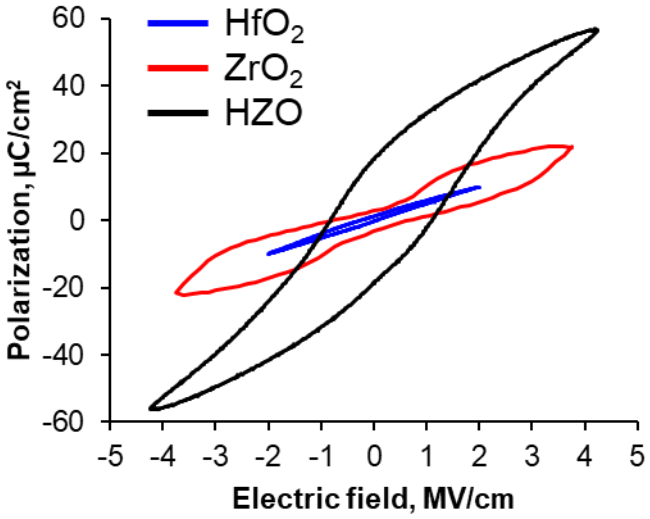

Fig. 9 Polarization versus electric field (*P*–*E*) curves for the HfO_2, ZrO_2, and HZO films.

SUMMARY AND CONCLUSIONS

We evaluated a newly developed $Hf(dmap)_4$ and $Zr(dmap)_4$ cocktail precursor that is a liquid at room temperature and exhibits excellent thermal stability. This cocktail precursor also exhibits excellent mixture stability, with a vaporization temperature of 150 °C. Thus, the binary ALD process can be used to make homogeneous HZO films. We demonstrated ALD of HZO films using O_3 as a co-reactant. The ALD window was estimated to range from 300 to 360 °C. The saturated growth rate and film density were 0.46 Å/cycle and 7.45 g/cm^3, respectively, at 360 °C. XPS analysis showed that a HZO film was deposited and that the Hf/Zr ratio was 1.00–1.05. This ratio is the same as the Hf/Zr concentration ratio in the cocktail precursor, indicating that the Hf/Zr ratio in the film can be controlled via the precursor Hf/Zr concentration ratio. Crystalline peaks were observed in the XRD patterns of the deposited HZO films and matched the orthorhombic phase (111 orientation) and tetragonal phase (111 orientation). MIM TiN–HZO–TiN devices were fabricated to evaluate the ferroelectric properties

of the HZO films. The remanent polarization $2P_r$ reached 36.9 μC/cm^2. Therefore, we conclude that the proposed Hf(dmap)$_4$ and Zr(dmap)$_4$ cocktail precursor is an excellent candidate as a HZO ALD precursor for use at temperatures greater than 300 °C.

ACKNOWLEDGMENTS

We are grateful to ADEKA CORPORATION for providing the FER-1 precursor and its vapor pressure, TGA, and ^{1}H-NMR data. This work was partly supported by "Crossover Alliance to Create the Future with People, Intelligence and Materials" and Advanced Research Infrastructure for Materials and Nanotechnology (ARIM) Japan from the Ministry of Education, Culture, Sports, Science and Technology (MEXT).

REFERENCES

(1) Robertson, J. High dielectric constant gate oxides for metal oxide Si transistors. *Reports on Progress in Physics* **2006**, *69* (2), 327-396. DOI: 10.1088/0034-4885/69/2/r02.

(2) Wong, H.; Iwai, H. On the scaling issues and high- κ replacement of ultrathin gate dielectrics for nanoscale MOS transistors. *Microelectronic Engineering* **2006**, *83* (10), 1867-1904. DOI: 10.1016/j.mee.2006.01.271.

(3) Choi, J. H.; Mao, Y.; Chang, J. P. Development of hafnium based high-k materials—A review. *Materials Science and Engineering: R: Reports* **2011**, *72* (6), 97-136. DOI: 10.1016/j.mser.2010.12.001.

(4) Robertson, J.; Wallace, R. M. High-K materials and metal gates for CMOS applications. *Materials Science and Engineering: R: Reports* **2015**, *88*, 1-41. DOI: 10.1016/j.mser.2014.11.001.

(5) Boescke, T. S.; Muller, J.; Brauhaus, D.; Schroder, U.; Bottger, U. Ferroelectricity in hafnium oxide thin films. *Applied Physics Letters* **2011**, *99* (10). DOI: 10.1063/1.3634052.

(6) Fan, Z.; Chen, J. S.; Wang, J. Ferroelectric HfO2-based materials for next-generation ferroelectric memories. *Journal of Advanced Dielectrics* **2016**, *6* (2). DOI: 10.1142/s2010135x16300036.

(7) Kim, K. D.; Lee, Y. H.; Gwon, T.; Kim, Y. J.; Kim, H. J.; Moon, T.; Hyun, S. D.; Park, H. W.; Park, M. H.; Hwang, C. S. Scale-up and optimization of HfO2-ZrO2 solid solution thin films for the electrostatic supercapacitors. *Nano Energy* **2017**, *39*, 390-399. DOI: 10.1016/j.nanoen.2017.07.017.

(8) Zhang, X.; Chen, L.; Sun, Q. Q.; Wang, L. H.; Zhou, P.; Lu, H. L.; Wang, P. F.; Ding, S. J.; Zhang, D. W. Inductive crystallization effect of atomic-layer-deposited Hf0.5Zr0.5O2 films for ferroelectric application. *Nanoscale Research Letters* **2015**, *10*, 1-5. DOI: 10.1186/s11671-014-0711-4.

(9) Shekhawat, A.; Hsain, H. A.; Lee, Y.; Jones, J. L.; Moghaddam, S. Effect of ferroelectric and

interface films on the tunneling electroresistance of the Al(2)O(3)/Hf(0.5)Zr(0.5)O(2)based ferroelectric tunnel junctions. *Nanotechnology* **2021**, *32* (48). DOI: 10.1088/1361-6528/ac1ebe From NLM PubMed-not-MEDLINE.

(10) He, G.; Liu, M.; Zhu, L. Q.; Chang, M.; Fang, Q.; Zhang, L. D. Effect of postdeposition annealing on the thermal stability and structural characteristics of sputtered HfO2 films on Si (100). *Surface Science* **2005**, *576* (1-3), 67-75. DOI: 10.1016/j.susc.2004.11.042.

(11) Van Elshocht, S.; Baklanov, M.; Brijs, B.; Carter, R.; Caymax, M.; Carbonell, L.; Claes, M.; Conard, T.; Cosnier, V.; Daté, L.; et al. Bulk Properties of MOCVD-Deposited HfO2 Layers for High k Dielectric Applications. *Journal of The Electrochemical Society* **2004**, *151* (10). DOI: 10.1149/1.1784822.

(12) Ben Amor, S.; Rogier, B.; Baud, G.; Jacquet, M.; Nardin, M. Characterization of zirconia films deposited by rf magnetron sputtering. *Materials Science and Engineering B-Solid State Materials for Advanced Technology* **1998**, *57* (1), 28-39. DOI: 10.1016/s0921-5107(98)00205-0.

(13) Smith, R. C.; Ma, T. Z.; Hoilien, N.; Tsung, L. Y.; Bevan, M. J.; Colombo, L.; Roberts, J.; Campbell, S. A.; Gladfelter, W. L. Chemical vapour deposition of the oxides of titanium, zirconium and hafnium for use as high-k materials in microelectronic devices. A carbon-free precursor for the synthesis of hafnium dioxide. *Advanced Materials for Optics and Electronics* **2000**, *10* (3-5), 105-114. DOI: 10.1002/1099-0712(200005/10)10:3/5<105::aid-amo402>3.3.co;2-a.

(14) Crowell, J. E. Chemical methods of thin film deposition: Chemical vapor deposition, atomic layer deposition, and related technologies. *Journal of Vacuum Science & Technology A* **2003**, *21* (5), S88-S95. DOI: 10.1116/1.1600451.

(15) Hausmann, D. M.; Kim, E.; Becker, J.; Gordon, R. G. Atomic layer deposition of hafnium and zirconium oxides using metal amide precursors. *Chemistry of Materials* **2002**, *14* (10), 4350-4358. DOI: 10.1021/cm020357x.

(16) Hausmann, D. M.; Gordon, R. G. Surface morphology and crystallinity control in the atomic layer deposition (ALD) of hafnium and zirconium oxide thin films. *Journal of Crystal Growth* **2003**, *249* (1-2), 251-261. DOI: 10.1016/s0022-0248(02)02133-4.

(17) Kim, B. S.; Hyun, S. D.; Moon, T.; Do Kim, K.; Lee, Y. H.; Park, H. W.; Lee, Y. B.; Roh, J.; Kim, B. Y.; Kim, H. H.; et al. A Comparative Study on the Ferroelectric Performances in Atomic Layer Deposited Hf(0.5)Zr(0.5)O(2) Thin Films Using Tetrakis(ethylmethylamino) and Tetrakis(dimethylamino) Precursors. *Nanoscale Res Lett* **2020**, *15* (1), 72. DOI: 10.1186/s11671-020-03301-4 From NLM PubMed-not-MEDLINE.

(18) Muller, J.; Boscke, T. S.; Schroder, U.; Mueller, S.; Brauhaus, D.; Bottger, U.; Frey, L.; Mikolajick, T. Ferroelectricity in Simple Binary ZrO2 and HfO2. *Nano Lett* **2012**, *12* (8), 4318-4323. DOI: 10.1021/nl302049k From NLM PubMed-not-MEDLINE.

(19) Materano, M.; Mittmann, T.; Lomenzo, P. D.; Zhou, C.; Jones, J. L.; Falkowski, M.; Kersch,

A.; Mikolajick, T.; Schroeder, U. Influence of Oxygen Content on the Structure and Reliability of Ferroelectric HfxZr1−xO2 Layers. *ACS Applied Electronic Materials* **2020**, *2* (11), 3618-3626. DOI: 10.1021/acsaelm.0c00680.

(20) Shekhawat, A.; Walters, G.; Yang, N.; Guo, J.; Nishida, T.; Moghaddam, S. Data retention and low voltage operation of Al(2)O(3)/Hf(0.5)Zr(0.5)O(2) based ferroelectric tunnel junctions. *Nanotechnology* **2020**, *31* (39), 39LT01. DOI: 10.1088/1361-6528/ab9cf7 From NLM PubMed-not-MEDLINE.

(21) Kim, H. B.; Jung, M.; Oh, Y.; Lee, S. W.; Suh, D.; Ahn, J. H. Superior and stable ferroelectric properties of hafnium-zirconium-oxide thin films deposited via atomic layer deposition using cyclopentadienyl-based precursors without annealing. *Nanoscale* **2021**, *13* (18), 8524-8530. DOI: 10.1039/d1nr01535d From NLM PubMed-not-MEDLINE.

(22) Oh, Y.; Kim, H.-B.; Lee, S. W.; Jeong, M. J.; Park, T. J.; Ahn, J.-H. Effects of Zr content and annealing on ferroelectricity of as-grown crystalline Hf1-xZrxO2 thin films using Hf[Cp(NMe2)3] and Zr[Cp(NMe2)3] precursors via atomic layer deposition. *Ceramics International* **2022**, *48* (17), 25661-25665. DOI: 10.1016/j.ceramint.2022.05.397.

(23) Kukli, K.; Pilvi, T.; Ritala, M.; Sajavaara, T.; Lu, J.; Leskelä, M. Atomic layer deposition of hafnium dioxide thin films from hafnium tetrakis(dimethylamide) and water. *Thin Solid Films* **2005**, *491* (1-2), 328-338. DOI: 10.1016/j.tsf.2005.05.050.

(24) Niinisto, J.; Kukli, K.; Kariniemi, M.; Ritala, M.; Leskela, M.; Blasco, N.; Pinchart, A.; Lachaud, C.; Laaroussi, N.; Wang, Z. Y.; et al. Novel mixed alkylamido-cyclopentadienyl precursors for ALD of ZrO2 thin films. *Journal of Materials Chemistry* **2008**, *18* (43), 5243-5247. DOI: 10.1039/b810922b.

(25) Nishida, A.; Hatase, M.; Yoshino, T.; Ooe, Y.; Mitsui, C. METHOD FOR MANUFACTURING THIN FILM. Japan WO/2022/107769, PCT/JP2021/042094, 2022.

(26) Nishida, A.; Hatase, M.; Yoshino, T.; Ooe, Y.; Mitsui, C. METHOD FOR MANUFACTURING THIN FILM. Japan WO/2022/107769, PCT/JP2021/042094, 2022.

(27) Nishida, A.; Katayama, T.; Matsuo, Y. Atomic Layer Deposition of HfO2 Films Using Tetrakis(1-(N,N-dimethylamino)-2-propoxy)hafnium [Hf(dmap)4] for Advanced Gate Dielectrics Applications. *ACS Applied Nano Materials* **2023**, *6* (19), 18029-18035. DOI: 10.1021/acsanm.3c03319.

(28) Dickson, R. S.; Dobney, B. J.; Eastwood, F. W. PREPARATION OF CYCLOPENTADIENE FROM ITS DIMER. *Journal of Chemical Education* **1987**, *64* (10), 898-898. DOI: 10.1021/ed064p898.

(29) Choi, P.; Baek, D.; Heo, S.; Choi, B. Atomic layer-deposited (HfZrO4)1−x(SiO2)x thin films for gate stack applications. *Thin Solid Films* **2018**, *652*, 2-9. DOI: 10.1016/j.tsf.2017.12.020.

Chapter 6

SUMMARY AND FUTURE WORKS

The purpose of this study is to evaluate the ALD processes, film characteristics, and electric properties of films prepared via novel liquid ALD precursors for industrial use. We have investigated and demonstrated $Y(sBuCp)_3$, $Hf(dmap)_4$, $Zr(dmap)_4$, and FER-1 precursors. The use of a novel precursor having industrially preferred properties can improve ALD processes compared with conventional precursor processes. In particular, this paper dealt with novel liquid ALD precursors that have a homoleptic structure for the ALD of high-K films such as Y_2O_3, HfO_2, ZrO_2, and $Hf_xZr_{1-x}O_2$ (HZO). We expect that the challenges of process optimization and expression of preferred film characteristics based on improving the properties of an ALD precursor through chemical modification are also applicable for other films. In particular, aminoalkoxide-type ALD precursors exhibited excellent ALD behavior. The ALD precursor market is expected to grow substantially, heightening the need for higher-performance ALD precursors for device fabrication. We will continue to work to develop novel ALD precursors with industrially preferred properties.

ACKNOWLEDGMENTS

The author thanks ADEKA CORPORATION for providing the ALD precursors [$Y(sBuCp)_3$, $Hf(dmap)_4$, $Zr(dmap)_4$, and FER-1] and the staff members of the Semiconductor Materials Department, Electronic Materials Development Laboratory, ADEKA CORPORATION for their support in acquiring the ^{1}H-NMR, TGA, and DSC data. The author also thanks Associate Professor Tsukasa Katayama of the Research Institute for Electronic Science (RIES) for support in fabricating the MIS and MIM capacitors and characterizing their electrical properties. I am grateful to Professor Kei Murakoshi, Professor Kosei Ueno, and Professor Toshihiro Shimada of Hokkaido University for their useful comments. Finally, I am grateful to Professor Yasutaka Matsuo of RIES, Hokkaido University for guidance and encouragement. This work was partly supported by the "Crossover Alliance to Create the Future with People, Intelligence and Materials" and Advanced Research Infrastructure for Materials and Nanotechnology (ARIM) Japan from the Ministry of Education, Culture, Sports, Science and Technology (MEXT).

List of publications

Journal publications related to this work.

1. Atomic Layer Deposition of Y_2O_3 Films Using Liquid Yttrium Precursor Tris(sec-butylcyclopentadienyl)yttrium and Water, *RSC Advances*, **13**, 39, 27255-27261, 2023, DOI: 10.1039/d3ra05217f (Chapter 2)
2. Atomic Layer Deposition of HfO_2 Films Using Tetrakis(1-(N,N-dimethylamino)-2-propoxy)hafnium [$Hf(dmap)_4$] for Advanced Gate Dielectrics Applications, *ACS Applied Nano Materials*, **6**, 19, 18029-18035, 2023, DOI: 10.1021/acsanm.3c03319 (Chapter 3)

Conference presentations

1. Higher Temperature ALD for HfO_2 Film using Hafnium Aminoalkoxide Precursors, 21st International Conference on Atomic Layer Deposition (ALD2021), June 27-30, 2021, Virtual meeting, Poster presentation. (Chapter 3)
2. High Temperature Atomic Layer Deposition of Hafnium Oxide using Homoleptic Hafnium Aminoalkoxide Precursor, 34th International Microprocesses and Nanotechnology Conference (MNC2021), October 26-29, 2021, On-line and on-demand conference, Oral presentation. (Chapter 3)
3. High Temperature Atomic Layer Deposition of Hafnium Oxide using Homoleptic Zirconium Aminoalkoxide Precursor, 35th International Microprocesses and Nanotechnology Conference (MNC2022), November 8-11, 2022, Tokushima, Japan, Poster presentation. (Chapter 4)